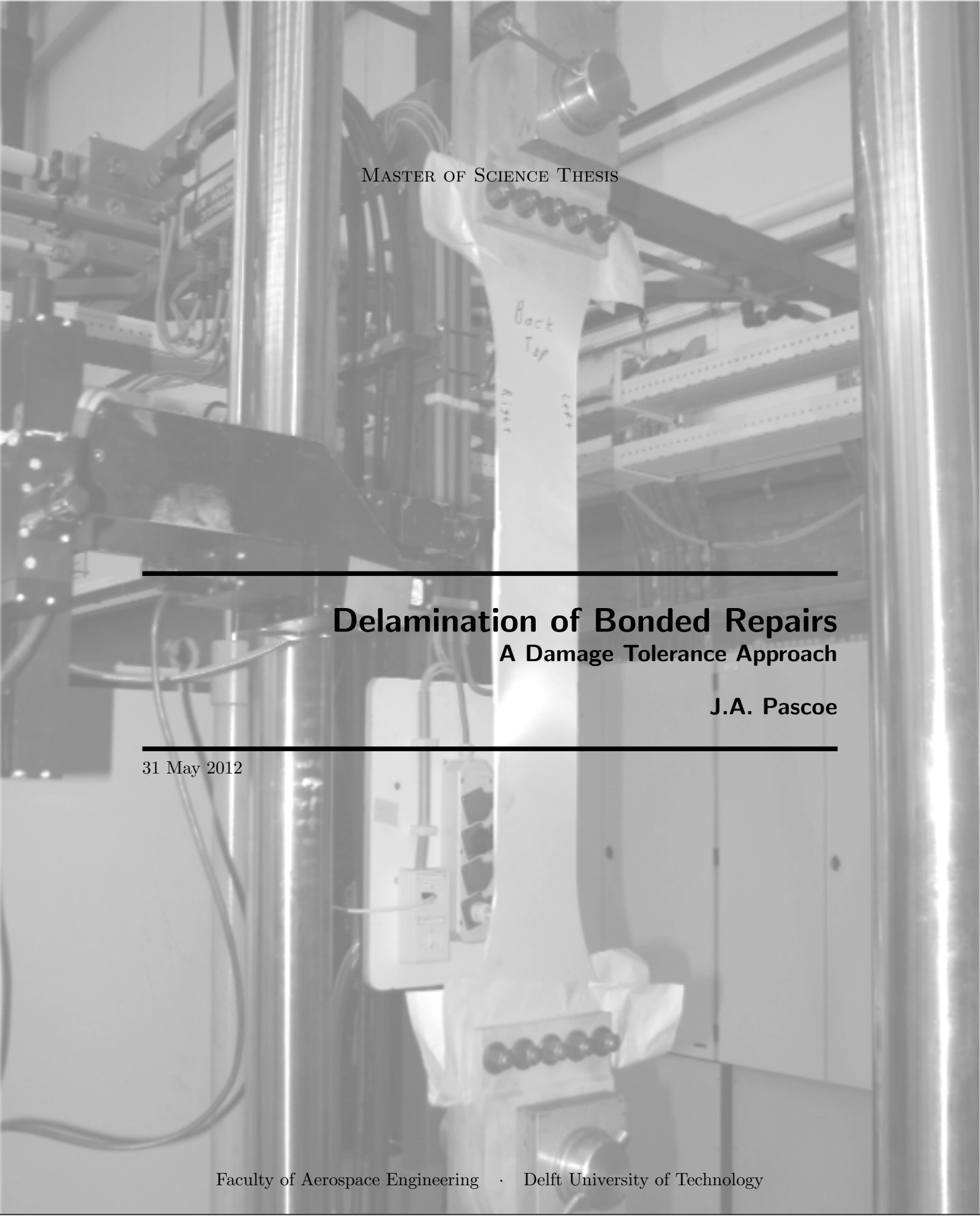

Master of Science Thesis

Delamination of Bonded Repairs

A Damage Tolerance Approach

J.A. Pascoe

31 May 2012

Faculty of Aerospace Engineering · Delft University of Technology

TU Delft

Delamination of Bonded Repairs
A Damage Tolerance Approach

Master of Science Thesis

For obtaining the degree of Master of Science in Aerospace Engineering at Delft University of Technology

J.A. Pascoe

31 May 2012

Faculty of Aerospace Engineering · Delft University of Technology

Delft University of Technology

Delft University Of Technology
Department Of
Structural Integrity

The undersigned hereby certify that they have read and recommend to the Faculty of Aerospace Engineering for acceptance a thesis entitled **"Delamination of Bonded Repairs"** by **J.A. Pascoe** in partial fulfillment of the requirements for the degree of **Master of Science**.

Dated: 31 May 2012

Head of department: _____
Prof.dr.ir. R. Benedictus

Supervisor: _____
Dr.ir. R.C. Alderliesten

Reader: _____
Dr. C.D. Rans

Reader: _____
Dipl.-Ing. R. Fischer

Abstract

Adhesive bonding of repair patches is a technology that offers many advantages over the traditional joining method of riveting. Unlike a riveted repair, a bonded repair does not require the drilling of holes in either the patch or the structure to be repaired and offers a smooth load transfer. In this way adhesive bonding overcomes a short-coming of riveted repairs: the introduction of new stress concentrations into the structure. Despite the advantages of adhesive bonding of repairs, their wide-scale application has been hindered by a lack of understanding of their damage tolerance behaviour.

The goal of this research was to improve the understanding of damage tolerance in bonded repairs by investigating the most important damage mechanism: delamination. Specifically, the goal was to develop a model that would allow the prediction of delamination growth as a result of fatigue loading.

In the developed model the delamination growth rate $\frac{db}{dN}$ is described as a power law function of the strain energy release rate (SERR) of the form:

$$\frac{db}{dN} = CG^m \tag{1}$$

Where G is the SERR and C and m are parameters that depend on the material as well as environmental influences such as temperature.

The SERR is found by a finite element (FE) analysis employing the virtual crack closure technique (VCCT). By pre-defining a number of delaminations of increasing length in the FE model, SERR can be expressed as a function of delamination length. Together with the relation between SERR and delamination growth rate this can be numerically integrated to predict the delamination length after a given number of fatigue cycles.

Development of the model was supported by two phases of testing. In the first phase material coupons were tested in order to find the parameters C and m. As a side-goal the influence of reduced temperature on delamination growth rate was also investigated, by conducting a number of tests at -30 ℃. In the second phase, more representative patch repair specimens were tested in order to validate the model.

Testing during the first phase was successful and confirmed that G is a configuration independent similarity parameter which can be used to predict delamination growth. Delamination growth was found to correlate most strongly with the mode II SERR component.

Lower temperature was found to significantly retard delamination growth. Finally, as had been indicated by the numerical analysis, interaction effects between delaminations of unequal lengths were found to be significant, especially in symmetric patch configurations.

Testing during the second phase was less successful. Two out of the four specimens tested did not exhibit any delamination. For the other two patches the scatter in the delamination length measurements was too high to allow a good validation of the model.

As a result of the research it was concluded that the mode II SERR can be used to predict delamination growth in simple coupons for uni-axial, constant amplitude, fatigue loading with a fixed R-ratio. Further research is required to confirm this also applies to more realistic load cases and structural configurations.

Executive Summary

Patch repairs of aircraft structures are traditionally fastened to their substrate by means of riveting. This requires the drilling of holes in the patch and substrate and means the load will be transferred in the form of point loads. Both these facts imply the introduction of stress concentrations into the structure, possibly acting as initiation sites for new fatigue damage. Adhesively bonded repairs largely overcome these problems by offering a uniform load transfer, without the need for extra holes in the structure.

Despite the advantages of bonded repairs, their application is hindered by the lack of knowledge of the damage tolerance behaviour. This requires bonded repairs to be certified under the 'no growth' or 'large damage carrying capacity' concepts. This results in heavier repairs and limits the possible application in highly stressed structures. Thus the objective of this research was to investigate the most important damage mode, delamination of the repair, with the objective of developing a delamination growth prediction model.

The research found it is possible to express the delamination growth rate in an adhesive interface as a power-law function of the mode II component of the strain energy release rate (SERR). The SERR for a given repair configuration can readily be determined by means of a finite element model employing the virtual crack closure technique(VCCT). The VCCT can be used to calculate the SERR as a function of delamination size and shape. This can be combined with the relation between delamination growth rate and SERR and numerically integrated to produce a delamination growth prediction.

The research was supported by two phases of experimental testing. In the first phase material coupons were tested in order to generate the required material data input for the delamination growth model. As several coupon configurations were tested, these experiments also confirmed that the SERR is a similarity parameter that can be related to the delamination growth rate. The coupon tests were also used to investigate the effect of temperature. It was found that delamination growth was retarded at low temperature (-30 ℃).

In the second phase of testing more representative patch repair specimens were tested in order to validate the model. Unfortunately the large amount of scatter in the delamination length measurements did not allow any firm conclusions to be drawn from the validation.

In conclusion the model developed was found to perform well for the fatigue loading and structural configurations tested, but needs to be extended and validated for more realistic load cases and structural configurations before it can be applied to real aircraft structures.

Acknowledgements

This Master's thesis could not have been completed without the valuable assistance I received from many quarters.

First of all I will thank my supervisors, Rinze Benedictus, René Alderliesten, Calvin Rans, and Riccardo Rodi, for all their advice and feedback on my work.

The experimental portion of this work would not have been possible without the help of the DASML lab staff, in particular: Berthil Grashof, Bob de Vogel, Johan Boender, Kees Paalvast, Frans Oostrum and Ed Roessen. My thanks goes to them for teaching me how to set up the fatigue machines and measuring equipment, assisting with the manufacturing of specimens and answering many small questions that came up during testing.

My contacts at Airbus, Richard Fischer and Roman Starikov, not only supplied me with the material coupon specimens, but were also always ready to provide advice for both experimental and theoretical problems, for which I am very grateful.

The administrative matters that came up during the thesis research, from having a place to work from in the first place, to arranging all the appropriate paperwork, often seemed to be resolved smoothly and as if by magic. In reality however this was down to the hard work of the department secretary: Gemma van der Windt. Thanks Gemma!

I am most grateful to Airbus for providing me with the material coupon specimens to use in my experiments.

Manufacturing of the patch repair specimens was sponsored by the Netherlands Organization for Scientific Research (NWO) and Technical Science Foundation (STW) under the Innovational Research Incentives Scheme Veni grant.

The lay-out of this thesis report was created using the LaTeXtemplate made available on www.aerostudents.com. The template is maintained by W.R.M. Van Hoydonck, to whom I extend my gratitude.

Finally I must thank all my colleagues: the interns, master's and PhD students, and staff, of the Structural Integrity and Composites department; those who are still here, as well as those who have left for other pastures, for providing me with such a enjoyable and stimulating working environment for the time it took me to conduct this research.

Contents

Abstract v

Executive Summary vii

Acknowledgements ix

1 Introduction 1

2 Literature Review and Chosen Approach 5

2.1 Failure Types and Interaction 5

2.2 Adherent Failure 6

2.3 Bond Line Failure 8

2.3.1 Analytical Approaches 8

2.3.2 Numerical Approaches 10

2.4 Conclusions 16

2.5 Chosen Approach 17

3 Specimens and Test Set-Up 19

3.1 Material Coupons 19

3.1.1 Series A 20

3.1.2 Series B 21

3.2 Patch Repair Specimens 23

3.2.1 Series C 23

4 Calculation of the Strain Energy Release Rate **27**

4.1 Analytical Methods . . . 27

4.2 Numerical Methods . . . 28

4.2.1 ΔU method . . . 29

4.2.2 VCCT . . . 29

4.3 Numerical Models . . . 30

4.3.1 Material Coupons . . . 31

4.3.2 Patch Repair Specimens . . . 31

5 Results of the Numerical Calculation of the Strain Energy Release Rate **33**

5.1 Comparison of Analytical and Numerical Methods for Calculating the SERR 33

5.2 SERR as a Function of Delamination Length . . . 35

5.3 Modal Distribution of the SERR . . . 36

5.4 Effect of Asymmetric Crack Growth . . . 40

5.5 Effect of Different Delamination Shapes . . . 42

5.6 SERR in the Patch Repair Configuration . . . 44

6 Test Results **49**

6.1 Series A . . . 49

6.2 Series B . . . 52

6.3 Relation Between Delamination Growth and SERR for series A and B . . 55

6.4 Series C . . . 59

6.4.1 Specimen C1 . . . 60

6.4.2 Specimen C2 . . . 62

6.4.3 Specimen C3 . . . 63

6.4.4 Specimen C4 . . . 64

6.5 Relation Between Delamination Growth and SERR for Series C . . . 65

7 Prediction of the Delamination Growth **69**

7.1 Description of the Model Used . . . 69

7.2 Comparison Between Predictions and Material Coupon Results . . . 70

7.3 Comparison Between Predictions and Patch Repair Results . . . 72

8 Conclusions and Recommendations **75**

8.1 Conclusions 75

8.2 Recommendations 77

8.2.1 Recommendations for Design Practice 77

8.2.2 Recommendations for Further Research 78

A Complete Test Results **85**

A.1 Series A 85

A.2 Series B 87

B Matlab Code **91**

Symbols

a	Crack length	mm
j	Number of cracked layers	$-$
m	Material constant in the Paris equation	$-$
n	Number of layers	$-$
t	Thickness	mm
u	Nodal displacement	mm
v	(Nodal) displacement	mm
w	Nodal displacement	mm
A	Area	m^2
C	Material constant in the Paris equation	unit is a function of m
C	Compliance	$-$
E	Young's Modulus	MPa
F	Force	N
G	Strain energy release rate	N/mm
G	Shear Modulus	MPa
K	(Spring) Stiffness	N/mm
K	Stress intensity factor	$MPa\sqrt{m}$
N	Number of cycles	$-$
P	Force	N
R	Stress ratio	$-$
S	Stress	MPa
T	Temperature	K,℃
U	Strain Energy	J
α	Coefficient of thermal expansion	$-$
β	Geometry factor	$-$
δ	Deformation	mm
ϵ	Strain	$-$
σ	Stress	MPa
ϕ	Rotation	rad
ψ	Mode-mix angle	$^\circ$

Subscripts

a	Adhesive
c	Critical
cl	Closure
cr	Crack
eff	Effective
f	Fibre
I	Mode I
II	Mode II
III	Mode III
lam	Laminate
max	Maximum
min	Minimum
p	Patch
s	Substrate
tot	Total
0	In 0°direction
90	In 90°direction
∞	Far field

Abbreviations

AC	Air-Conditioning
BFRP	Boron Fibre Reinforced Polymer
CFRP	Carbon Fibre Reinforced Polymer
CCD	Charge Coupled Device
COD	Crack Opening Displacement
CTE	Coefficient of Thermal Expansion
CZM	Cohesive Zone Model
DSTO	Defence Science and Technology Organisation
DUT	Delft University of Technology
FCG	Fatigue Crack Growth
FE	Finite Element
FEA	Finite Element Analysis
FEM	Finite Element Method
FML	Fibre Metal Laminate
FOD	Foreign Object Damage
FRP	Fibre Reinforced Polymer
HSS	High Static Strength
LDCC	Large Damage Carrying Capacity
LEFM	Linear Elastic Fracture Mechanics
M(T)	Middle crack Tension
MPC	Multi Point Constraint
MVF	Metal Volume Fraction
RAAF	Royal Australian Air Force
SENT	Single Edge Notch Tension
SERR	Strain Energy Release Rate
SIF	Stress Intensity Factor
TRS	Thermal Residual Stress
VCCT	Virtual Crack Closure Technique

Chapter 1

Introduction

Like any structure used in service, aircraft structures accumulate damage during their operational usage. This damage can be caused by a variety of sources such as fatigue, corrosion, bird strike, foreign object damage (FOD) and many others. In most cases this damage will necessitate some form of repair in order to ensure that the structure remains capable of bearing the required loads. A common form of repair for small structural damage is patching; an extra layer of material is added to the structure in order to bridge and/or reinforce a damaged area[1]. To be able to perform this function the patch must somehow be attached to the structure that is to be repaired, which shall be referred to as the substrate. The traditional method of attaching the patch to the substrate is by riveting. The major disadvantages of this method are that it requires rivet holes and it creates discrete load transfer points. Both of these act as stress raisers, increasing the fatigue sensitivity of the structure. In addition riveting may not be suitable for materials with a low allowable bearing stress, such as most fibre-reinforced polymer (FRP) composites currently used in aerospace. The use of an adhesive to bond the patch to the substrate offers a possible solution. The adhesive provides a continuous and smooth load transfer and avoids the need to load either the substrate or the patch in bearing.

The application of bonded patch technology in aerospace was pioneered by (a precursor of) Australia's Defence Science and Technology Organisation (DSTO) in the nineteen seventies. It was first applied to the Royal Australian Air Force's (RAAF) Hercules aircraft in 1975 [1]. DSTO developed a number of successful repairs for various aircraft in the RAAF fleet using bonded boron fibre reinforced polymer (BFRP) patches. Since these first efforts, a variety of patch and bonding technologies have been investigated, including aluminium patches and patches made from fibre metal laminates (FMLs) such as Glare [2], generally with promising results. Regardless of the specific technology used, an obstacle for the application of any form of bonded repair in aviation is its certification, especially the demonstration of damage tolerance. Currently three approaches have been identified to satisfy the damage tolerance requirements:

[1] A patch may also be applied as a preventative measure, in order to reinforce a certain area.

1. **No-growth** In a no-growth approach the structure is designed such that any damage that may be present will not grow under the conditions experienced in service. This approach may not be possible in heavily loaded structures and typically leads to over designed (i.e. heavy) structures. This approach is analogous to the safe-life philosophy used in metallic structure in that the structure is shown to not experience any damage growth during a set period.

2. **Large damage carrying capacity** In the large damage carrying capacity (LDCC) approach the structure must be shown to be capable of carrying limit loads with obvious and excessive damage (e.g. >80% disbond). Like the no-growth approach, the LDCC approach may also lead to over-designed structures. In addition the result of the LDCC approach may be that no credit is given for the presence of a patch, i.e. the repair is assumed to be completely ineffective for the purposes of determining inspection intervals. This is indeed the case for a number of repairs currently in use in the RAAF [3]. The LDCC approach is analogous to the fail-safe philosophy used in metallic structure. This can be seen by considering the adhesive layer of a bonded patch as the combination of multiple load carrying areas, i.e. multiple load paths. Thus, as with a metallic fail-safe design, when adopting the LDCC approach care should be taken to investigate the effects (both immediate and longer term) of the stress redistribution that will occur after a load path failure.

3. **Safety by inspection** In this approach the structure is regularly inspected so that any damage that occurs may be detected and repaired before it reduces the residual strength of the structure to an unacceptable level. The inspection interval is determined based on an understanding of damage evolution and the time required for the damage to grow from a detectable size to a critical size. This approach is analogous to the damage tolerance approach used in conventional metallic structure design.

From the above it is clear that the safety by inspection approach is the most desirable method of certification, as it leads to the lightest structure. Unfortunately the understanding of damage growth, especially the growth of delaminations in the adhesive layer between substrate and patch, is not yet advanced enough to allow sufficiently accurate predictions of damage growth. Without these predictions it is impossible to set an inspection period and thereby ensure damage tolerance. This thesis aims to further the understanding of delamination growth and provide a method to predict it. The research concerns mainly metal-metal and metal-FML bonds, based on the available specimens and the interest from industry. However many of the main conclusions are expected to be applicable to other material combinations as well.

The research for this thesis was conducted in two phases, which both involved experimental research and finite element modelling. In the first phase coupons were tested in order to gain an understanding of the material behaviour of the materials under investigation and develop a prediction model. In the second phase tests were carried out on a representative structure in order to validate the prediction model.

Chapter 2 of this report contains a literature review, giving an overview of the prior knowledge on delamination of bonded repairs available in the literature. On the basis of the conclusions of the literature review a prediction approach was chosen for this thesis.

The outline of this approach is discusses at the end of Chapter 2. Chapter 3 discusses the specimens used and the experimental set-up. In chapter 4 the methods used to determine the strain energy release rate, which is used in the growth prediction model, are presented. The results of these calculations are discussed in chapter 5. Chapter 6 presents the test results. The goal of this research was to create a model capable of predicting delamination growth. The results of the developed model are discussed in 7. Chapter 8 presents the conclusions of the research, as well as recommendations for further research and how the developed model can be used.

Chapter 2

Literature Review and Chosen Approach

Before starting on the research for this thesis, a literature review was conducted in order to determine the current knowledge on the topic of the damage tolerance of bonded repairs. The results of that literature review are presented in this chapter. The various failure types that can occur within a bonded repair, as well as the interactions between them will be discussed. Various models for describing and predicting failure and damage growth will be presented, followed by the conclusions that can be drawn from the current literature. Although this thesis deals with the delamination of bonded repairs the literature review also examined more general aspects of damage tolerance of such repairs.

As a final introductory remark to this literature review it should be stated that when consulting the literature on delamination growth care should be taken to determine whether the results presented are applicable to dynamic delamination growth (i.e. under cyclic loading). Many papers deal only with static delamination growth, without explicitly stating this.

2.1 Failure Types and Interaction

When analysing the damage tolerance of a bonded repair, there are two failure types that should be considered: bond line failure (delamination) and adherent failure.

For dynamic loading and especially in the case of patches applied over a crack in the substrate, there will be interaction between these failure modes. For example Guo and Wu [4] have shown that the crack bridging stress[1] in an FML is a function of the shape of the delamination at the interface between the cracked metal layer and the fibre layer(s). The same may be expected to hold true for a bonded patch. Similarly Aggelopoulos et al. investigated delaminations growing at the crack mouth for patches bonded over a crack

[1] Which affects the driving force for crack growth in an FML

growing in depth direction in thick plates [5]. They found that the growth of the delamination effects the stress state at the crack tip. Conversely it is known that the presence of a crack in a metal layer of an FML influences delamination growth, as explained e.g. by Alderliesten [6]. However before these interaction effects can be modelled, a better understanding of the mechanisms of delamination growth itself is required. Hence the current work will focus on loading cases such that there is no fatigue crack growth (FCG) in the adherents and thus no need of accounting for interaction effects. In light of this statement it is good to note that even if cracking does take place in the adherents, interaction effects are negligible if the delamination is sufficiently far from the crack mouth [5].

As mentioned above this work will focus on failure of the adhesive layer resulting in delamination of the adherents. For this case Alderliesten identifies two main classes of failure prediction methods in the literature [7]:

- Stress / Strain methods; using peak shear and peel stresses to determine bond line failure and peak tensile and compressive stress for adherent failure
- Fracture mechanics based methods; using energy balance methods for bond line damage growth and stress intensity factors for adherent damage growth.

Alderliesten states that the stress/strain methods are more suited for static failure and damage initiation predictions, whereas the fracture mechanics based methods are more suitable for predicting damage growth. Stress/strain methods may be used to find critical values that allow prediction of final failure, though these are commonly determined experimentally. Since this research is concerned with fatigue damage, it is mainly the fracture mechanics based methods that will be considered.

2.2 Adherent Failure

The mechanisms involved in adherent failure depend on the adherent material. In metals the main failure mechanism is FCG. The main failure mechanism for FMLs is also FCG, which occurs in the metal layers, however crack bridging by the fibre layers reduces the rate of the crack growth. For monolithic metals the mechanisms involved have been extensively studied over the past decades. The rate of crack growth is determined by the stress intensity factor (SIF), K, which is given by [8]:

$$K = \beta S \sqrt{\pi a} \tag{2.1}$$

Where S is the applied (far-field) stress, a is the crack length and β is a dimensionless geometry factor.

K can be related to the crack growth rate by means of the Paris relation:

$$\frac{da}{dN} = C\Delta K^m \tag{2.2}$$

Where C and m are material constants, and ΔK is defined as:

$$\Delta K = K_{max} - K_{min} \tag{2.3}$$

With K_{max} and K_{min} being the values of K for S_{max} and S_{min} respectively.

One of the shortcomings of the Paris law is that it doesn't account for the effect of the R-ratio:

$$R = \frac{S_{min}}{S_{max}} \tag{2.4}$$

Different values of R give different Paris curves. Another shortcoming is the Paris law's failure to describe the asymptotic behaviour of crack growth at low and high values of ΔK. It can also be difficult to apply the Paris law in the case of variable amplitude loading. In many cases however, especially for constant amplitude fatigue, the Paris relation gives a good prediction of crack growth for most of the (post-initiation) fatigue life of a structure.

FMLs, having only been developed relatively recently, have not been as extensively studied. However validated models are available that allow for prediction of FCG in the metal layers [6, 9, 10]. The main problems in developing these models were correctly accounting for the effect of fibre bridging over the crack, and correctly modelling the interaction between crack growth in the metal layers and growth of delaminations between the fibre and the metal layers.

At first glance a promising approach to modelling failure in adhesive bonds would seem to be to treat a bonded repair as a 'special FML'. Just as in an FML the fibre layer bridges the crack in the metal layer, so the patch may be expected to bridge the crack in the substrate in the case of a repair. Unfortunately there are problems with this approach. For example, using the data of Jones et al. [11], Jones [12] claims that for short to medium length cracks (defined as crack lengths from about 0.1 to 20 mm [12] or cracks with ΔK close to the threshold value [11]) repaired with a composite patch, the effect of fibre bridging is negligible. Instead for short cracks the effect of the patch should be wholly attributed to the reduction of net section stress caused by the increase of the cross-sectional area. It is important to note that, as emphasised in [11], this conclusion only applies to short cracks. For long cracks ($a > 40$ mm) the SIF remains constant as the crack grows, suggesting crack bridging does play an important role in those cases[2]. Furthermore Jones notes that the contribution of fibre bridging increases with the interlaminar shear modulus of the patch [12]. Hence for a metal or Glare patch the contribution of crack bridging will be larger than for a composite patch.

Another important point raised by Jones [12] is that the stress state in the patch is not constant through the thickness, i.e. a 3D-model is needed to accurately predict the stress state. Furthermore the peak surface strain did not occur over the crack (which was located at the centre line of the patch). Although most of Jones' paper [12] deals with composite patches, these conclusions were based partially on experiments done on Glare patches [13]. Whether this finding also holds true for monolithic aluminium patches is unclear, but there is no obvious reason why it should not.

A further complication when trying to apply the methods discussed above to FCG for a bonded repair is that patch repairs to aircraft are usually applied asymmetrically, that is to say a patch is only applied to one side of the cracked structure, rather than to both

[2]Since the SIF is a function of crack length, if the SIF remains constant for an increasing crack length there must be some mechanism to counteract the increase in SIF that would otherwise be expected. Crack bridging is thought to be this mechanism.

sides. This is done either because one side of the structure is hard to reach or in order to preserve the aerodynamic shape of the outer surface. This asymmetry results in secondary bending in both the patch and the substrate. Boscolo et al. [14] have shown that in this case a geometrically non-linear analysis is required to find an effective SIF in order to properly predict FCG. The same mechanism results in the requirement to use an effective R-ratio when calculating the crack growth rate in this case. This effective R-ratio is a function of crack length, and not equal to the ratio of minimum and maximum applied far field stress.

2.3 Bond Line Failure

Bond line failure is generally referred to as delamination in the literature, although in most cases there is no investigation if the failure is indeed caused by delamination at the adherent-adhesive interface or if there is cracking (cohesive failure) in the adhesive. Both analytical and numerical approaches for the prediction of delamination growth are available in the literature. It is interesting to note that none of the prediction methods available in the literature so far consider the effect of temperature. However recent results [15] indicate that, at least for FMLs, the delamination growth rate increases both at elevated temperature and at temperatures below room temperature.

Most delamination studies in literature deal with delamination in FMLs or other fibre-reinforced composite materials. However as long as they do not rely on the actual details of the delamination mechanism they can easily be adapted to the case of a bonded repair.

2.3.1 Analytical Approaches

Alderliesten et al. [16] have shown that delamination growth, at least in Glare, can be modelled using the strain energy release rate (SERR), G. The delamination growth is then given by:

$$\frac{db}{dN} = C_d \left(\sqrt{G_{d,max}} - \sqrt{G_{d,min}} \right)^{m_d} \tag{2.5}$$

where b is the delamination length and C_d and m_d are material constants.

It is readily seen that this equation is a restatement of the Paris relation (equation 2.2) using ΔG rather than ΔK as the basis of similitude. As recently emphasised by Rans et al. [17], to apply the similarity principle the correct expression for ΔG is not $G_{max} - G_{min}$, but rather

$$\Delta G = \left[\sqrt{G_{max}} - \sqrt{G_{min}} \right]^2 = \frac{1}{2W} \frac{dC}{da} (\Delta P)^2 \tag{2.6}$$

where C is the compliance.

Using this fact to re-analyse several cases where delamination growth had been reported as a function of $G_{max} - G_{min}$, Rans et al. showed that for mode II loading changing the R-ratio has little or no effect. In addition they showed that residual stresses have no effect on the delamination growth and that mixed mode growth can be predicted by superposition of mode I and mode II contributions to growth.

Allegri et al. [18] have proposed an alternative delamination growth law, given by

$$\frac{db}{dN} = C\left(\frac{G_{IImax}}{G_{IIc}}\right)^{\frac{m}{(1-R)^2}} \tag{2.7}$$

Notable features are that this function depends on G_{IImax} rather than on ΔG, and the inclusion of a stress ratio dependency. Allegri et al. only claim validity for 'intermediate toughness fibre reinforced epoxies', defined as those with a critical mode II SERR between 0.8 kJ/m^2 and 1.2 kJ/m^2. However basis, physical or otherwise, for this limitation is not mentioned. Although the proposed equation showed good agreement with experimental data, in light of the results of Rans et al. [17] it is questionable whether the inclusion of a dependency on R is worthwhile in the case of mode II behaviour.

To apply equation 2.5 or 2.7 to predict delamination growth it is necessary to find an expression for G. Following [10] and [19], Alderliesten et al. [16] showed that for a Glare laminate G is given by

$$\begin{aligned} G_d = &\frac{\sigma_{lam}^2}{2jE_{al}}\left[\gamma^2(n_{al}-n_{cr})t_{al} - \lambda^2 n_{al}t_{al}\right. \\ &\left. + \frac{E_f,0}{E_a l}n_{f,0}t_{f,0}(\gamma^2-\lambda^2) + \frac{E_{f,90}}{E_{al}}n_{f,90}t_{f,90}(\gamma^2-\lambda^2)\right] \end{aligned} \tag{2.8}$$

with

$$\gamma = \frac{t_{lam}}{(n_{al}-n_{cr})t_{al} + \frac{E_{f,0}}{E_{al}}n_{f,0}t_{f,0} + \frac{E_{f,90}}{E_{al}}n_{f,90}t_{f,90}} \tag{2.9}$$

$$\lambda = \frac{t_{lam}}{n_{al}t_{al} + \frac{E_{f,0}}{E_{al}}n_{f,0}t_{f,0} + \frac{E_{f,90}}{E_{al}}n_{f,90}t_{f,90}} \tag{2.10}$$

Where n_{cr} is the number of cracked layers, j is the number of interfaces to the cracked layers, the $f,0$ subscript refers to the fibre layers in the 0 direction and the $f,90$ subscript refers to the fibre layers in the 90 direction.

Using this approach delamination growth has been predicted for a variety of test specimens showing fair to good agreement with the measurements [7, 16]. In the cases where agreement is less good, Alderliesten [7] attributes this to the effect of the delamination initiation and initial growth. Equation 2.8 describes G for mode II opening. Alderliesten has shown experimentally that delamination growth is mainly determined by the mode II loading and that the effect of mode I loading on growth may be neglected [20]. Delamination initiation however is governed by mode I peel stresses, and during the initial growth (up to about 1 mm) the delamination experiences mixed mode loading. This causes an error in the predictions. Alderliesten identifies two possible approaches to improve the predictions [7]:

- Predict delamination initiation based on the mode I peel stresses, and then predict delamination growth based on a damage growth equation such as 2.5 or 2.7.
- Assume an initial manufacturing flaw and then predict the delamination growth based on a damage growth equation.

These approaches can be characterised as a scientific approach (the first approach), which aims to increase understanding of the material behaviour involved, and an engineering approach, which uses a simpler model and accepts less scientific insight in return. Given the current state-of-the-art, the engineering approach, as Alderliesten notes, would seem to be the more appropriate for evaluating the damage tolerance of bonded repairs. This is especially true if one considers that a damage tolerance analysis usually requires the assumption of an initial flaw anyway, rather than the assumption of an initially undamaged structure from which natural initiation will occur.

The greatest challenge when using the approach described above to analyse bonded repairs will be correctly describing G. Equation 2.8 was derived following Marissen [10] and Suiker and Fleck [19] and applies to an FML. In principle the same method can be used to describe G for any type of laminate. Since a bonded repair is essentially a type of laminate, at first glance it would seem that a suitable modification of equation 2.8 considering the thickness and stiffness of the adhesive, patch and substrate could give a good description of the SERR. However in both [10] and [19] it is implicitly assumed during the derivation that the stress in each layer is constant through the thickness. Since Jones [12] has shown that this is not the case for an adhesively bonded patch, it is uncertain whether equation 2.8 gives a good description of the SERR for a bonded repair. Furthermore in the case of an FML, or indeed nearly any composite panel studied to date, the length and width of all layers is the same, unlike in the case of a patch repair. Another important difference is that the thickness of the 'adhesive layer' is different. In an FML or composite, the closest analogy to an adhesive layer is the resin rich zone between the fibres in one layer and the fibres or metal in the next layer. The thickness of the resin rich zone depends on the material, but in all cases is at most a small fraction of the thickness of one laminate layer. In the case of adhesive bonding however the the adhesive layer is much thicker, which may also be expected to influence the validity of models developed for FMLs when applied to a bonded repair. For example Ji et al. [21] recently showed that adhesive thickness effects mode II fracture toughness and shear strength. Finally the derivations presented in [10] and [19] assume a symmetic structure and thus must be modified to include secondary bending effects before they can be used in the analysis of a bonded repair.

2.3.2 Numerical Approaches

Several numerical models are available in the literature that model delamination growth by use of finite element (FE) analyses. A common feature of many of these models is that they make use of the virtual crack closure technique (VCCT) to determine the SERR.

The VCCT was first proposed by Rybicki and Kanninen [22] and an overview of its development and applications may be found in [23]. The basics of the VCCT are illustrated in figure 2.1. The strain energy release when increasing the length of a crack (or delamination) over an increment Δa is assumed to be equal to the energy required to close the crack by the same amount. This energy is found by considering the work done by the forces at the crack tip node when displaced over a distance equal to the displacement of the nodes directly behind the crack tip. The exact equations depend on the type of elements used in the FE model; a summary for several common element types can be found in [23]. In the case of the 2D model shown in figure 2.1 the mode I SERR is given

by:

$$G_I = -\frac{1}{2\Delta a} F 2w \tag{2.11}$$

assuming the model has a unit width. The mode II SERR is found by considering the corresponding load and displacements (i.e. in horizontal direction), which are not shown in figure 2.1. It is important to note that when using the VCCT a 3D-model is required to correctly model a non-straight delamination front, although the adherents themselves may be modelled by computationally more efficient 2D plate or shell elements, rather than by 3D solid elements [23].

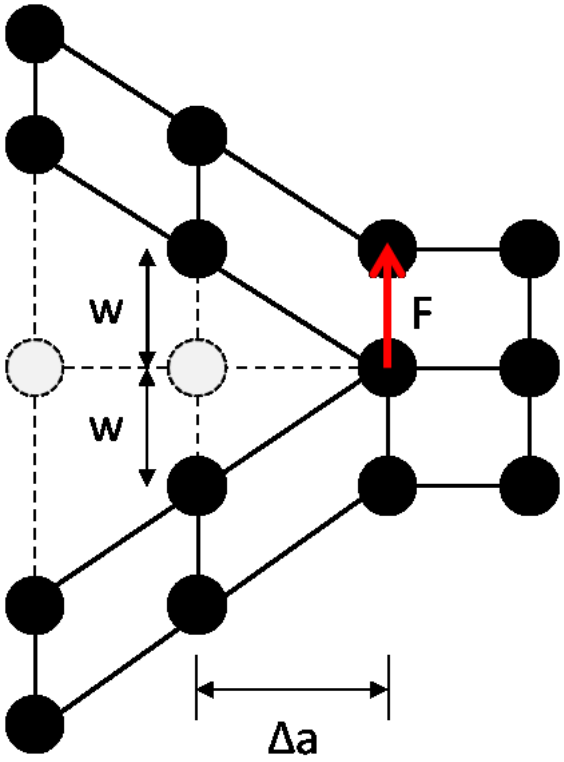

Figure 2.1: The virtual crack closure technique; only the nodes in the vicinity of the crack tip are shown. The SERR is found by considering the work done by force F, when closing the crack over the distance Δa, by displacement of the nodes behind the crack tip over the distance w. Note that the nodal displacements here are shown as being equal, but this is not necessary.

Xie and Biggers make use of the VCCT in combination with special interface elements to determine delamination growth [24, 25]. The interface elements consist of two sets of nine nodes (representing the interfaces at the top and bottom of the adhesive layer) connected at the central node by three springs, which represent the adhesive layer itself. The use of three springs allows separate determination of the three modal components of the SERR: G_I, G_{II} and G_{III}. Once the fracture criterion given by equation 2.12 is exceeded at a node the spring stiffnesses are set to zero, resulting in delamination growth.

$$\left(\frac{G_I}{G_{Ic}}\right)^{\alpha} + \left(\frac{G_{II}}{G_{IIc}}\right)^{\beta} + \left(\frac{G_{III}}{G_{IIIc}}\right)^{\gamma} \geq 1 \tag{2.12}$$

Usually the delamination front is required to be orthogonal to the mesh used to ensure a proper analysis. This means remeshing is necessary after every delamination growth increment. Xie and Biggers however developed an algorithm to determine the delamination front orientation, avoiding the need for remeshing.

The Xie-Biggers model was validated by comparison with analytical solutions and 3D FE models and showed good agreement [24]. No comparisons between the Xie-Biggers model and experimental results could be found in the literature however. Furthermore, although Xie and Biggers do not state this explicitly it should be noted that the Xie-Biggers model only captures (quasi-)static delamination growth and thus cannot be used to predict fatigue growth without modification.

The most complete model available in the literature that deals with both crack growth and delamination in the case of a bonded structure is the FE model developed by Boscolo and Zhang [26, 27]. Though the model was primarily developed for the analysis of plates with a bonded strap reinforcement, it is also applicable to patched repair, as the mechanisms involved are the same [14]. The main difference is that in the structures studied by Boscolo and Zhang the crack started outside of the area covered by the 'patch', whereas in a patch repair the patch will be applied over the crack. Boscolo and Zhang identify four mechanisms that need to be accounted for in their model:

1. **Strap stiffening and bridging.** When the crack is still at a distance from the strap the presence of the strap will still (locally) increase the stiffness and hence alter the stress state. When the crack grows through the substrate under the strap, the strap will act to bridge the crack, reducing the crack opening displacement.

2. **Disbond failure.** Delamination of the strap and the substrate will reduce the effectiveness of the bridging effect.

3. **Secondary bending.** Due to the asymmetry of the configuration there will be secondary bending as a result of the external load. This will alter the stress state.

4. **Thermal residual stress (TRS).** The mismatch in thermal expansion coefficients (CTEs) of the two adherents (assuming they are not made of the same material) will result in stresses as both try to contract by a differing amount following cooling from the cure temperature[3]. Due to the asymmetry of the configuration these residual stresses will also produce secondary bending.

As the subject of the current work is delamination of the adhesive, only the disbond failure portion of the Boscolo-Zhang model will be treated here.

Like Xie and Biggers [24], Boscolo and Zhang [26] use an interface element to model the adhesive layer. In the Boscolo-Zhang model the adhesive is represented by two rigid elements connected by three coincident springs at each node. The use of three springs allows separate modelling of the inter laminar peeling (mode I) and the two shear modes (mode II and III). The stiffness of the springs is given by

$$K_{az} = \frac{A_a E_a}{t_a}, \quad K_{ax} = K_{ay} = \frac{A_a G_a}{t_a} \tag{2.13}$$

[3] Adhesive curing typically takes place at an elevated temperature, in the order of 80-120 ℃.

where A_a is the area of the adhesive element, E_a is the Young's modulus of the adhesive, G_a is the shear modulus of the adhesive and t_a is the thickness of the adhesive. Multi Point Constraint (MPC) equations are used to ensure displacement continuity: Let u, v, w represent the nodal displacements in respectively x, y, and z direction, let ϕ^x denote rotation about the x-axis and ϕ^y denote rotation about the y-axis. Let subscript s denote substrate, p denote patch, $a1$ the nodes on the bottom of the adhesive layer and $a2$ the nodes on top of the adhesive layer. The MPC equations then are:

$$\begin{aligned} u_{a1} &= u_s + \frac{t_s}{2}\phi_s^y, \quad v_{a1} = v_s - \frac{t_s}{2}\phi_s^x, \quad w_{a1} = w_s \\ u_{a2} &= u_r - \frac{t_s}{2}\phi_r^y, \quad v_{a2} = v_r + \frac{t_s}{2}\phi_r^x, \quad w_{a2} = w_r \end{aligned} \tag{2.14}$$

Boscolo and Zhang use the VCCT to compute the three components of the SERR as follows:

$$G_I = -\frac{F_{az}(w_{a2} - w_{a1})}{\Delta l b_a}, G_{II} = -\frac{F_{ay}(v_{a2} - v_{a1})}{\Delta l b_a}, G_{III} = -\frac{F_{ax}(u_{a2} - u_{a1})}{\Delta l b_a} \tag{2.15}$$

where $\Delta l b_a$ is the area of crack extension. Delamination growth is simulated by deleting elements from the analysis when the following failure criterion is exceeded:

$$\frac{G_I}{G_{Ic}} + \frac{G_{II}}{G_{IIc}} \geq 1 \tag{2.16}$$

If an adhesive element fails the delamination front is updated and another FE analysis is carried out. This process is repeated until no more elements fail, at which point the node at the substrate crack tip is released and the process starts again. As Boscolo and Zhang note this is a quasi-static analysis method, as it does not account for the effect of fatigue loads. Boscolo and Zhang justify this by claiming that delamination growth in patch repairs and bonded straps is mostly due to high local stresses caused by the stress-singularity effect at the substrate crack tip, and not due to the fatigue loads themselves, which is a rather questionable assumption, as will be discussed later. In addition it should be remarked that the G_{Ic} value used can not be the value for G_{Ic} that is found in a static delamination test, since if it were the delamination would by definition continue propagating until failure of the structure.

An important point not noted by Boscolo and Zhang is that their model, unlike that of Xie and Biggers [24], does not appear to utilise any kind of algorithim to find the delamination front orientation, nor is any re-meshing done. This means that the Boscolo-Zhang model implicitly assumes that the mesh is always orthogonal to the delamination front, which depending on the shape of the structure and the initial delamination (should it exist) is a questionable assumption.

Note furthermore that the presence of a (growing) fatigue crack is required to drive delamination growth and that in the absence of a fatigue crack the Boscolo-Zhang model is unable to predict fatigue induced delamination growth. This was also shown in the validation Boscolo and Zhang performed [27].

The validation was carried out in comparison to both experimental data and 3D FE analyses for two configurations, a middle tension (M(T)) configuration, and a single edge notch tension (SENT) configuration, as shown in figure 2.2. The substrate was made

from aluminium 7085-T7651. The straps were bonded using FM94 as the adhesive and a number of strap materials were tested: a carbon-fibre composite, a glass-fibre composite, Ti-6Al-4V and Glare I 3/2.

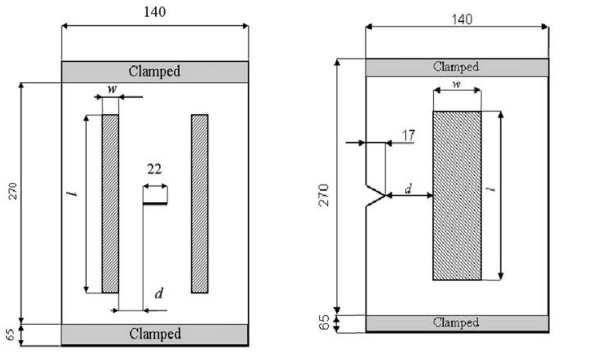

(a) Middle crack tension M(T) specimen with two straps

(b) Single edge notch tension (SENT) specimen with a strap

Figure 2.2: Configurations used for the validation of the Boscolo-Zhang model, figure from [27].

The results of the validation of the delamination component of the Boscolo-Zhang model are shown in figure 2.3. The delamination prediction was investigated for a SENT specimen with a Ti strap and the M(T) specimen with a glass-fibre composite strap.

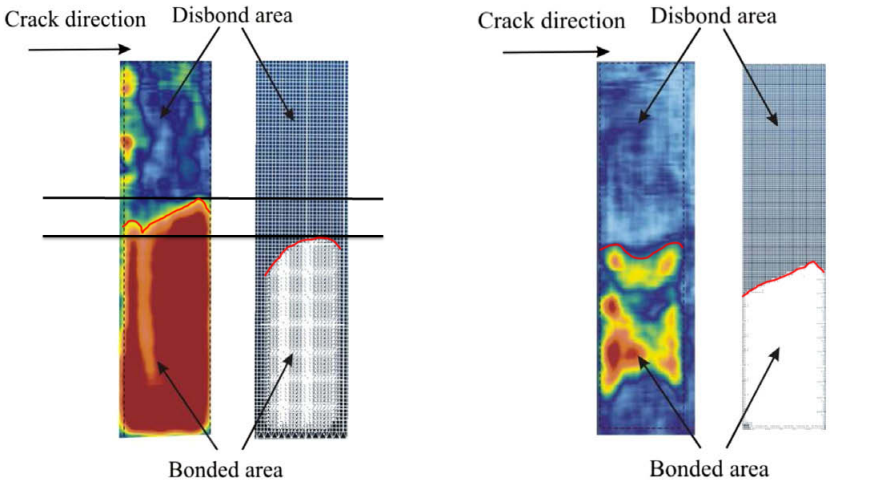

(a) SENT sample and Ti strap $w20d5t2l200$.

(b) M(T) sample with GFRP strap $w20d2.5t4.4l180$.

Figure 2.3: Delamination as predicted by the Boscolo-Zhang model compared with experimental results. Only half of the strap is shown, the top edge in the figure is the centre line of the strap. Figure from [27]. Horizontal lines showing extent of predicted and measured delamination as well as curves highlighting the delamination front added for emphasis.

For the SENT specimen the agreement between the model and experiment was relatively good, with the difference in predicted delamination length appearing to be about 5% of the strap length. For the M(T) specimen the agreement wasn't as good. Although the

size of the delamination that grew from the fatigue crack is relatively close to that predicted by the model, the model failed to predict a second delamination which grew from the bottom edge of the strap. This failure was caused by the model's the requirement for a fatigue crack to drive delamination. As a consequence the model is also incapable of predicting delamination initiation. Note that the presence of this delamination invalidates Boscolo and Zhang's claim that delamination growth is mainly caused by the high stresses at substrate crack-tip stress-singularity. A detail that Boscolo and Zhang do not remark on is that the bonded area of the strap seems to consist of two bonded regions separated by a delaminated zone, while the model predicts a single bonded zone. Furthermore, for both specimens the shape of the delamination front seen in the experimental results is quite different from the shape of the delamination front predicted by the model. Boscolo and Zhang do not comment on this, but a possible explanation is that Boscolo and Zhang do not ensure the mesh is orthogonal to the delamination front at all times nor do they have any way of compensating for this, such as for example the front tracing algorithm in the Xie-Biggers model [24].

Some current FE codes already contain modules to allow for automatic delamination propagation analyses. Krueger tested the applicability of these modules in the ABAQUS® code for delamination of CFRP composites [28, 29, 30], by comparing them with a manually created, code independent, benchmark. Krueger generally found good agreement between the benchmark and the automatic calculation provided inputs such as stabilisation factors and time increments were appropriately chosen, highlighting the importance of benchmarking in order to validate models created in this way.

Both the Xie-Biggers model and the (validation of) the Boscolo-Zhang model highlight the difficulty of incorporating delamination growth directly in the FE analyses. An alternative approach could be to create a map of the SERR as a function of delamination size and shape, using a series of pre-defined delamination geometries. This is the approach followed by Krueger in his benchmarking exercises [28, 29, 30]. Using an iterative interpolation in this map a first estimate of delamination growth can be produced. For a prescribed delamination the SERR can readily be found by means of the VCCT.

An alternative method for numerically predicting delamination growth is to make use of a cohesive zone model (CZM). The exact implementation varies (see [31, 32] for some examples) but in all cases the interface between adherent and adhesive is modelled with a cohesive zone element. The stiffness of this element is not constant. Instead a constitutive model is used to govern the relation between traction and displacement (or separation) in the cohesive element. A damage parameter, D, is introduced to represent the effect of fatigue damage accumulation, by degrading the stiffness of the cohesive element. An example of a multi-mode[4] bi-linear constitutive model, with use of a damage parameter to degrade the stiffness, is shown in figure 2.4.

An advantage of the CZM approach is that both initiation and propagation behaviour is captured, and that crack or delamination growth is integrated into the FE model. A disadvantage is that both an appropriate constitutive law and an appropriate damage parameter evolution need to be determined. Both require a number of parameters that must be experimentally determined and for which the physical basis is unclear.

[4] i.e. the traction depends on two deformation modes

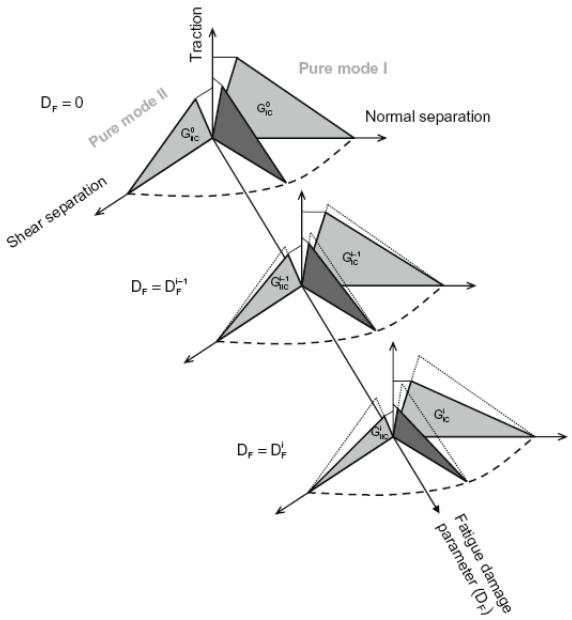

Figure 2.4: An example of a multi-mode bi-linear constitutive traction-displacement relation in a CZM. The traction depends on deformation in two directions (modes). The relation between traction and separation is described by two straight lines. The damage parameter D is used to reduce the stifness, and thus the traction for a given displacement. Image from [32].

2.4 Conclusions

There is currently no model available to evaluate the delamination growth behaviour of a bonded repair. The closest approximation is the numerical model developed by Boscolo and Zhang for plates reinforced with bonded straps [26], which is unable to model a delamination growing without an underlying substrate crack to produce the driving force. However the required features of a model, both for general damage tolerance and specifically for delamination growth of a bonded repair, as well as promising starting points, can be identified.

A damage tolerance model for a bonded repair will have to account for both failure of the adherent(s) and failure of the bond line, and for the interaction of these two modes. Adherent failure in the case of a monolithic metal adherent is caused by fatigue crack growth, which may be predicted using the well-known relationship to SIF range. The challenge for a bonded repair is correctly determining the SIF range in the adherents. In the case of an FML adherent, failure models are also available (e.g. that of Alderliesten [6]), and once again correctly determining the stress state in the adherent(s) is the challenge.

Delamination growth can be calculated analytically by means of a Paris type relation as a function of the SERR range [16] or of the maximum SERR [18]. Numerically quasi-static delamination growth can be found by modelling the adhesive by two-layer plus spring elements [26, 24] with the use of an appropriate failure criterion. Proper implementation of such a procedure in an FE analysis will require the use of delamination front tracing

algorithms such as that developed by Xie and Biggers [24] or other means of dealing with delamination growth that is not orthogonal to the mesh (e.g. remeshing). To predict fatigue delamination growth the two-layer plus springs approach will have to be modified, as it currently only models quasi-static growth. Rather than incorporating delamination growth directly in the FE model an alternative is to use the FE model to create a map of SERR as a function of delamination shape and size. Combining this map with an (analytical) delamination growth law then allows prediction of the delamination growth.

Another option is to make use of a CZM [31, 32], which requires the formulation of both a constitutive law for the cohesive elements and a damage parameter evolution law. Both require the experimental determination of a number of parameters in order to make the predicted behaviour match experiment. This makes the implementation significantly more complex than a SERR map plus delamination growth law method. In addition the physical basis of the required parameters is unclear.

For analytical models a correct expression for the SERR needs to be found, as the expressions currently available in the literature (e.g. [16, 19]) have been determined for FMLs, which have significantly different geometries. Furthermore the available models assume that the stress is constant through the thickness of a laminate layer, which is untrue in the case of a bonded patch [12] or in the case of secondary bending [26]. Secondary bending is completely ignored in current analytical models for the SERR, but is expected to be important for bonded repair, which generally contain asymmetric joints.

Numerically the SERR for a prescribed delamination can readily be found by means of the VCCT. This allows the creation of a SERR map as a function of delamination geometry. This can be used as an input for both analytical and numerical growth models. The accuracy of an integrated delamination growth model in an FE code, as well as the required 'tuning parameters' can be determined by manually creating a code-independent benchmark [28, 29, 30].

Current delamination models, both analytical and numerical, are not able to correctly predict initiation behaviour. Correct prediction of delamination initiation could greatly enhance the accuracy of life predictions. Alternatively an initial flaw can be assumed, as is generally required in any case for a damage tolerance analysis.

2.5 Chosen Approach

Based on the conclusions presented above it was decided to limit the scope of the research to delamination growth; the initiation phase was not considered. The approach selected to predict the delamination growth was the combination of a SERR map (i.e. a function or method capable of calculating the SERR for a given delamination size and shape) and a delamination growth law of the form:

$$\frac{db}{dN} = C\,(G)^m \tag{2.17}$$

The SERR map was created by means of finite element analysis (FEA) using the VCCT. This can be done for any arbitrary configuration; only the material properties are necessary as supporting data. However, to use equation 2.17 it is necessary to first determine

C and m. Based on experience with the Paris relation in metallic crack growth these are thought to be material parameters. Thus the research took place in two phases. In the first phase coupons were tested in order to determine C and m. At the request of Airbus, who supplied the coupons, a number of coupons were tested at -30°Cin order to study the effect of temperature on delamination growth. The first phase also allowed for a quick, though somewhat tautological, verification of the chosen approach. In the second phase a number of specimens were manufactured that were representative of a patch repair. These were then used to experimentally validate the delamination growth prediction model.

An open question at the start of the research was which representation of G to use in equation 2.17: whether to use G_{max} (the SERR with an applied stress of S_{max}) or ΔG and whether to use the total SERR or only one of the modal components. This too was investigated during the first phase of the research.

Chapter 3

Specimens and Test Set-Up

This chapter describes the experimental portion of the thesis work. Two classes of specimen were tested: material coupons and patch repair specimens. The material coupons were tested to gain data on the material response to fatigue loading. In particular the objective was to gather sufficient data on delamination growth to allow the determination of the parameters in a Paris-type (i.e. power-law) delamination growth relation.

The patch repair specimens were designed to be (more) representative of a patch repair applied to an aircraft skin section. The objective of these tests was to validate the delamination growth prediction model and to provide some guidelines on optimisation of the repair patch geometry.

3.1 Material Coupons

The material coupons were manufactured by Airbus. There were two types of specimen, with both a symmetric and an asymmetric variant per type. Type I specimens represented an aluminium patch bonded to Glare skin and Type II specimens represented a Glare patch bonded to aluminium skin. A 0.4 mm aluminium plate was bonded between the 'patch' and the 'skin'. This doubler was made of Al-7475 T761, while the alloy used for the skin (Type II specimen) or patch (Type I specimen) was Al-7175. The Glare grade used was high static strength (HSS) Glare-3 7/6 0.4-0.3-0.3-0.3-0.3-0.4-0.4. The relevant mechanical properties of these materials may be found in table 3.1. The properties of the aluminium alloys were taken from [33] and the Young's modulus of the Glare lay-up was calculated with the aid of the metal volume fraction (MVF) method [34]. The Poisson ratio of Glare was taken as 0.3. The adhesive used to bond Al-7175 to Al-7475 was FM73M.06 and the adhesive used to bond the Al-7475 and Glare parts was FM300K.05.

Two series of material coupons were tested during the course of this research, designated series A and series B. Some specimens manufactured in the same batch had previously been tested at Airbus and at Delft University of Technology (DUT). Test data was also available for these specimens. All specimens were manufactured by Airbus using a process also used in regular production.

	E [GPa]	Poisson Ratio [-]
Al-7175	72.0	0.33
Al-7475 T761	70.3	0.33
HSS-Glare-3 7/6	53.9	0.3

Table 3.1: Mechanical properties of the materials used in the test specimens. Note that for this Glare grade $E_x \approx E_y$. Al-alloy properties from [33], Glare properties calculated using the MVF method [34].

3.1.1 Series A

Series A specimens were of the Type I asymmetrical configuration. The specimens consisted of a tapered Al-7175 patch bonded to an HSS Glare plate. A 0.4 mm thick Al-7475 T761 plate was bonded between the Glare 'skin' and the Al-7175 'patch'. This plate extended beyond the edge of the patch. The specimen configuration is shown schematically in figure 3.1. The taper does not extend all the way to the patch end. Instead there is a short flat section at the edges of the patch, as shown in figure 3.2.

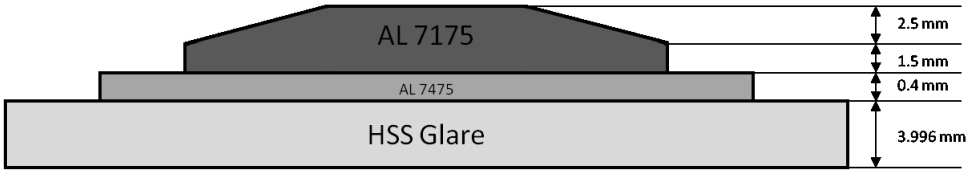

Figure 3.1: Schematic overview of the configuration of series A specimens. Figure is not to scale.

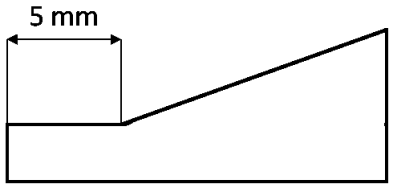

Figure 3.2: Detail of the tapering at the patch ends of series A specimens. Figure is not to scale.

The sides of the specimens were coated with white paint to facilitate measurement of the delamination growth[1]. The specimens were cycled with fatigue loading in an MTS-810 500 kN hydraulic fatigue testing machine under load control. Testing occurred at room temperature, with a frequency of 5 Hz and R=0.1. The maximum stress applied is shown in table 3.2. Delamination growth was measured using a travelling camera with high magnification. In order to measure the delamination size the test was paused at regular

[1] Although the paint is necessary to improve the visibility of the delamination, it does introduce the implicit assumption that the delamination will not grow under the paint layer without inducing cracking or at least visible deformation of the paint. Prior work at TU Delft (unpublished) where the direct visual method used in this work was compared with the use of Digital Image Correlation (DIC) gives confidence that this assumption is valid. DIC can be used to determine the delamination front by locating the accompanying strain gradient.

intervals. Maximum load was then applied in order to open the delamination, before measuring the delamination length using the camera. Figure 3.3 shows the test set-up and figure 3.4 shows schematically the orientation of the camera relative to the specimen.

Specimen	S_{max} [MPa]
A1	150
A2	170

Table 3.2: Test matrix for series A.

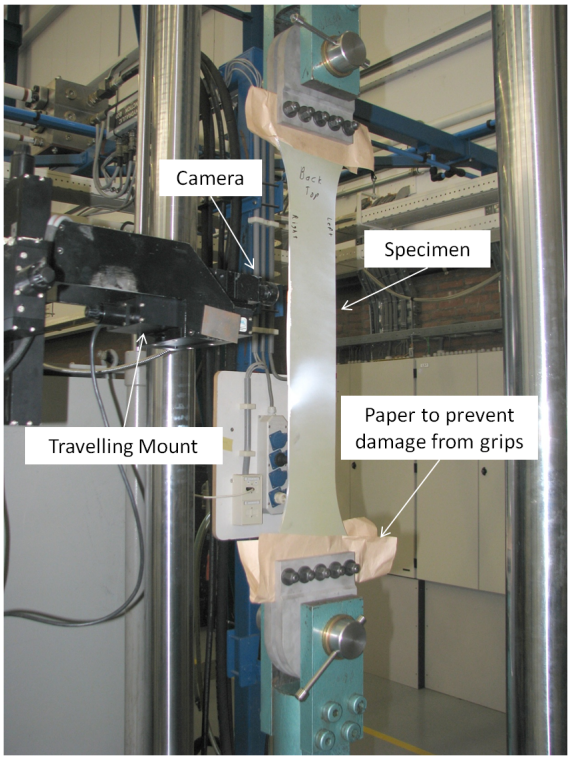

Figure 3.3: Test set-up, showing the specimen installed in the test machine and the travelling camera used for delamination length measurements.

3.1.2 Series B

Series B consisted of specimens with the Type II symmetrical configuration. Apart from switching the patch and skin materials the other notable difference between these specimens and those used for series A is the lack of taper. Figure 3.5 gives a schematic overview of the Type II symmetrical configuration.

At the request of Airbus the series B specimens were used to investigate the effect of low temperature on delamination growth. To this end testing occurred at a temperature of -30 ℃.

As with the series A specimens, the sides of the series B specimens were coated with white paint to enhance visibility of the delaminations. Testing was done on an MTS 250 kN

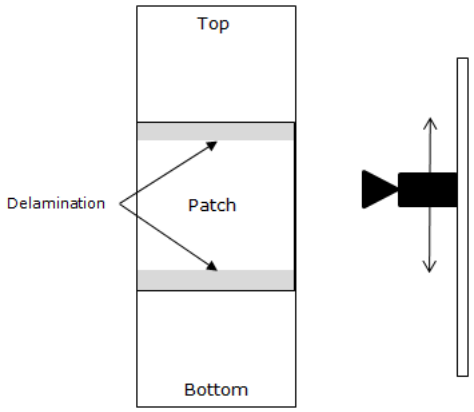

Figure 3.4: Schematic overview of the position of the camera used to monitor delamination growth.

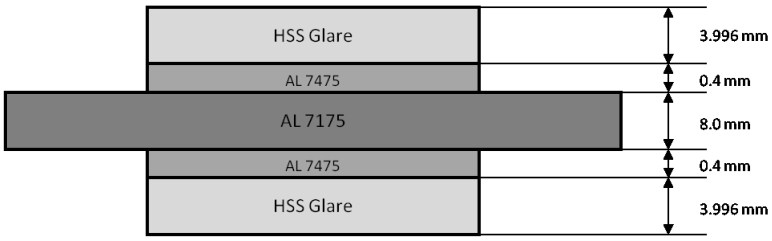

Figure 3.5: Schematic overview of the configuration of series B specimens. Figure is not to scale.

hydraulic fatigue testing machine under load control. The test frequency was 5 Hz and R=0.1. The maximum stress applied during the testing is shown in table 3.3. Temperature control was achieved by placing an insulated chamber around the specimen. The chamber was connected to an air-conditioning (AC) unit that supplied cooled air. A thermocouple exposed to the air within the AC unit provided temperature control. In addition an extra thermocouple was applied to the patch area of the specimen with adhesive tape. This allowed the specimen temperature to be monitored and the temperature control of the AC unit to be adjusted as necessary. In general the temperature control had to be set several degrees lower than the desired specimen temperature.

Again a camera was used to measure the delamination growth. However the use of the insulated box required use of a lens with a longer focal length. This lens had a lower magnification, resulting in reduced visibility of the delamination tip. This resulted in greater scatter in the delamination length measurements. Furthermore the view port of the insulated box reduced the field of view of the camera, so that only two delaminations could be viewed. Had the side of the box been completely transparent, four delaminations would have been visible, as can be seen in figure 3.6.

Specimen	S_{max} [MPa]	Remarks
B1	170	No valid measurements
B2	190	
B3	150	
B4	160	
B5	170	
B6	210	

Table 3.3: Test matrix for series B.

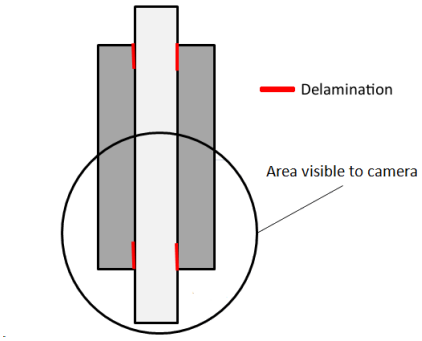

Figure 3.6: Estimate of the field of view of the camera during testing of series B.

3.2 Patch Repair Specimens

The patch repair specimens were intended to be more representative of an actual patch repair than the material coupons. The goal was to test whether the data gathered using the material coupons could be used to predict delamination growth for a substantially different configuration. In addition several design options for improving (i.e. reducing) delamination growth rate were tested.

3.2.1 Series C

The four patch repair specimens were designated series C. Each specimen in series C consisted of a base-plate with a patch bonded over a 30x30 mm square cut-out in the base-plate. The base-plate is shown in figure 3.7. A different patch shape was used for each specimen in order to test the effect of corner radius and patch shape on the delamination growth rate. Three of the four patches were 100x100 mm squares. One of these had sharp corners, one had corners rounded with a 10mm radius and one had corners rounded to a 20mm radius. The fourth patch was octagonal, with the dimensions shown in figure 3.8. Both the base-plates and the patches were cut and milled from a sheet of Al-7075 with a thickness of 1.6mm. A summary of the patch types used is given in table 3.4

The base-plates and patches underwent a pre-treatment consisting of chromic acid anodising, followed by priming with BR-127. The patches were bonded to the base-plates with FM94, which was cured in an autoclave at 120 ℃and six bar for one hour. The heating rate was 2 ℃/minute and the same rate was used to cool the specimen back to

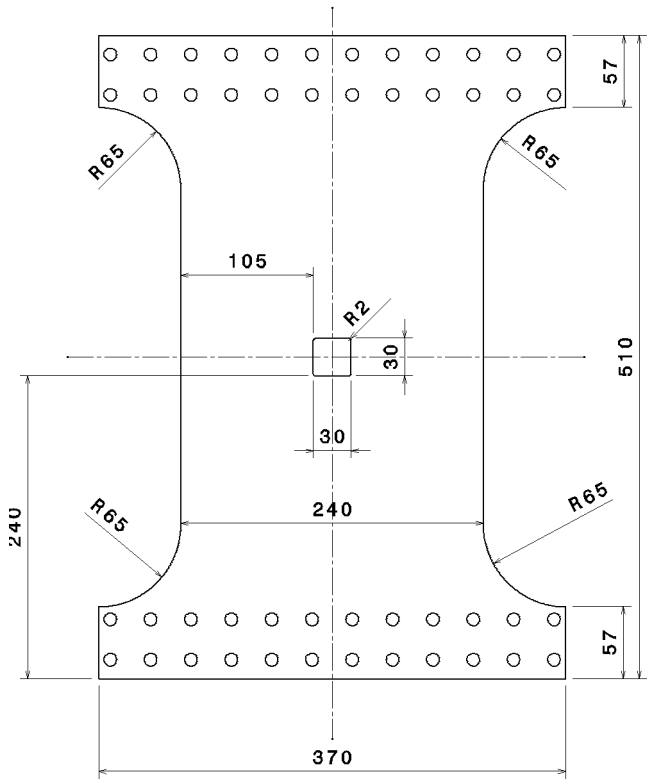

Figure 3.7: Base-plate used for the series C specimens. Top view, dimensions in mm.

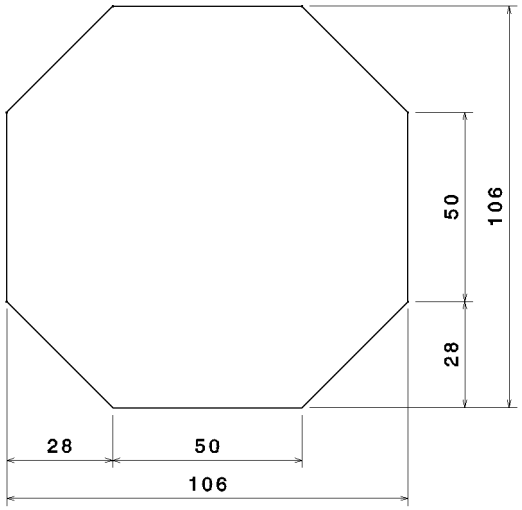

Figure 3.8: Dimensions (in mm) of the octagonal patch.

room temperature after the curing time had elapsed. On specimens C1, C2 and C4 a 5mm strip of adhesive tape was applied to the base plate under one of the patch edges to initiate a delamination. On specimen C3 the entire patch area was bonded in order to investigate the difference in delamination (initiation) behaviour.

Specimen	Patch Type
C1	Square, sharp corners
C2	Square, 10 mm corner radius
C3	Square, 20 mm corner radius
C4	Octagonal

Table 3.4: Overview of the patch types used for series C specimens

The series C specimens were tested at room temperature on an MTS 250 kN hydraulic fatigue testing machine under load control at 5 Hz. A constant amplitude fatigue load was applied such that the maximum gross section stress (so considering a width of 240 mm) S_{max} was equal to 170 MPa. The R-ratio was 0.1.

Due to the width of the base-plates measuring the delamination growth by direct visual measurements was not possible. Instead digital image correlation (DIC) was used to measure the strain field on surface of the patch. Since there will be a significant difference in the strain of the bonded and the disbonded portions of the patch, this method can be used to detect the location of the delamination front. The secondary bending of the specimens makes 3D DIC a necessity to obtain accurate numbers for the strain. However for the purposes of this experiment it was deemed sufficient to be able to measure the location of the strain gradient over the delamination front, rather then requiring the actual value of the strains. As the availability of the 3D DIC cameras was limited, 3D DIC was only used for specimen C1, while specimens C2, C3, and C4 were monitored using 2D DIC. The position of the camera(s)[2] with respect to the specimens is shown in figure 3.9.

Although it was stated at the start of this section that the patch repair specimens were intended to be more representative of an actual repair, there are some notable differences between the test specimens and actual patch repairs. First of all the test specimens consisted of a patch bonded to a flat plate, without any of the support structures (e.g. stiffeners, frames) present in an actual aircraft structure. Second, most panels used in aircraft structures, certainly in the primary structure, are singly or doubly curved, in contrast to the test specimens. Third the specimens were tested under constant amplitude uni-axial loading with constant R-ratio. In reality the load will most likely be bi-axial and have a variable amplitude and R-ratio. Still, the patch repair specimens are one step closer to actual aircraft structures than the material coupons tested in the first part of the research.

[2] 3D DIC requires the use of two cameras, 2D DIC only requires one.

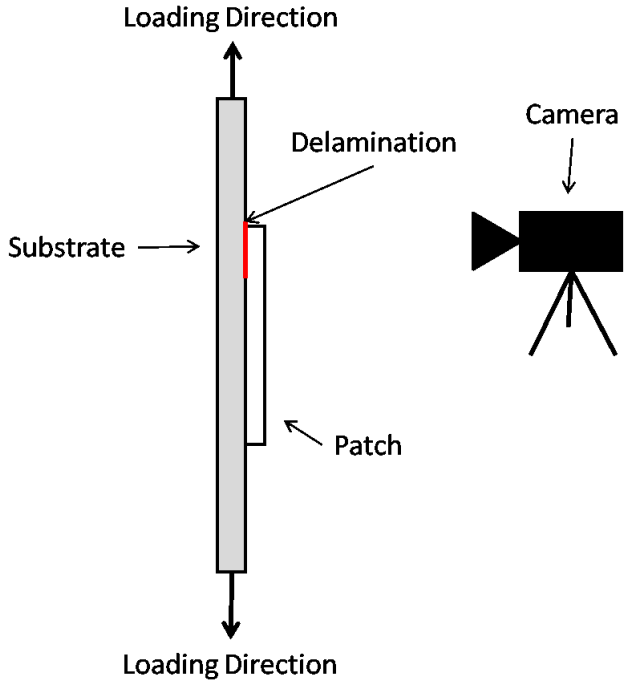

Figure 3.9: Schematic overview of the position of the DIC camera(s) used to monitor delamination growth for the patch repair specimens.

Chapter 4

Calculation of the Strain Energy Release Rate

In the literature review (Chapter 2) it was shown that delamination growth can be formulated as a function of the SERR. Using this function has been shown to be a promising approach to predicting delamination growth. To be able to do this one must of course first determine the SERR. This chapter will present and compare various methods for doing this. Both analytical and numerical methods will be discussed, followed by a description of the numerical models used.

4.1 Analytical Methods

Three analytical methods for determining G have been provided in [35]. One method was derived for the run-out of a bonded doubler, which is equivalent to the material coupons tested. The two other methods were developed for a patch bonded over a gap in the substrate. All three methods assume a constant stress distribution through the thickness of the adherents, and thus are strictly speaking only applicable to symmetrical configurations. They are presented here in order to allow a comparison with the numerical calculations.

Method A The first method presented in [35] is based on the equations derived in [16] for the SERR in Glare. For the bonded doubler run-out these can be reworked to give:

$$G_d = \frac{S_{base}^2 t_{base}}{2E_{base}} \cdot \frac{E_{doubler} t_{doubler}}{E_{doubler} t_{doubler} + E_{base} t_{base}} \tag{4.1}$$

Method B The second method is based on relating the SERR to the total strain energy contained in the base material. In principle it is a restatement of method I for the patch

repair configuration (i.e. with a doubler bonded over a gap in the substrate). G is given by:

$$G = \frac{S_{lam}^2 t_{lam}}{2E_{lam}} \tag{4.2}$$

where the subscript lam refers to the laminate made up of the substrate and patch.

Method C The third method is based on equilibrium between the elements of the two adherents and the adhesive. The derivation, as presented in [35] leads to

$$G_I = \frac{P^2 t_{sub}^2 t_{ad}}{2E_{ad}L^2}\left(\frac{\sin^2\left(\frac{cL}{2}\right)\sinh^2\left(\frac{cL}{2}\right)+\cos^2\left(\frac{cL}{2}\right)\cosh^2\left(\frac{cL}{2}\right)}{\cos\left(\frac{cL}{2}\right)\sin\left(\frac{cL}{2}\right)+\cosh\left(\frac{cL}{2}\right)\sinh\left(\frac{cL}{2}\right)}\right)^2 \tag{4.3}$$

$$G_{II} = \frac{t_{ad}}{2G_{ad}}\left(\frac{Pk\cosh\left(\frac{kL}{2}\right)}{2\sinh\left(\frac{kL}{2}\right)}\right)^2 \tag{4.4}$$

with P the load per unit width of the laminate and L half the bond length (the method treats a patch bonded over a cut-out as a single lap joint). The parameters k and c are given by the following equations:

$$k = \sqrt{\frac{8G_{ad}}{E_{sub}t_{sub}t_{ad}}} \tag{4.5}$$

$$c = \sqrt[4]{\frac{6}{E_{sub}t_{sub}^3 E_{ad}t_{ad}}} \tag{4.6}$$

In addition to the absence of secondary bending this method assumes that patch and substrate consist of the same material and have the same thickness. Neither of these assumptions hold in the case of a generalised patch repair, limiting the usefulness of this method. Further it should noted that this method assumes an interruption of the substrate layer (i.e. the patch is applied over a hole or crack), if there is no interruption the value of P used should be set to half of the real value. A final important point is that only method C contains a delamination length dependency (in the form of the bond length included in the equations). The other two methods assume G is not a function of b.

4.2 Numerical Methods

The current analytical methods are not sufficient to investigate more general patch repairs, especially if they are in an asymmetric configuration which will cause secondary bending. Hence numerical analyses using the finite element method (FEM) are required. There are several methods by which the SERR can be extracted from a FEA. In this work the ΔU method and VCCT were investigated. All analyses were carried out in Abaqus-6.10-1. A full description of the numerical models used will be given further in this chapter.

4.2.1 ΔU method

The SERR is given by [17]:

$$G = \frac{d}{db}(F - \Delta U) \tag{4.7}$$

where U is the strain energy, F the work applied to the system and b is the delamination length. In the analysis of the earlier test results that was available G had been calculated as:

$$G = \frac{d}{dA}\Delta U \approx \frac{\Delta U}{\Delta A} \tag{4.8}$$

where A is the crack area (b times specimen width for a straight delamination front). Using equation 4.8 the SERR can be easily found by calculating the total strain energy at two chosen delamination lengths. This method only provides the total SERR, and does not provide any information about the modal distribution.

Unfortunately the validity of equation 4.8 was found to be rather limited. For a 2D FEM model of a symmetric configuration use of 4.8 was found to give approximately the same results as the VCCT (discussed below). However for a 3D model of a symmetric configuration, or a 2D or 3D model of an asymmetric configuration, the two methods gave different results. This difference could be resolved by artificially constraining certain deformations (secondary bending for the asymmetric configuration, Poisson contraction for the 3D symmetric configuration). In this case both methods gave the same number for the SERR. This suggests that the problem is caused by the fact that equation 4.8 neglects the work term which should be present, as is shown by equation 4.7. It seems that secondary bending and Poisson contraction introduce non-negligible work terms, which need to be included for a proper calculation of the SERR. To avoid this complication it was decided to use the VCCT for all calculations of the SERR.

4.2.2 VCCT

The VCCT was described in section 2.3.2. To briefly recap here: the underlying principle is that the energy released when the crack grows by the length of one element (i.e. the SERR) is assumed to be equal to the energy required to close the crack by the same length. A useful feature of the VCCT is that is does not calculate the total SERR, but calculates each of the three components separately. VCCT capability is integrated into Abaqus, though only in a crack propagation module. This assumes crack propagation occurs when the following criterion is exceeded:

$$\left(\frac{G_I}{G_{Ic}}\right)^{\alpha} + \left(\frac{G_{II}}{G_{IIc}}\right)^{\beta} + \left(\frac{G_{III}}{G_{IIIc}}\right)^{\gamma} \geq 1 \tag{4.9}$$

As only the SERR was required, and not the crack propagation prediction, very high values were entered for the critical G components. This assured that the crack growth criterion would not be exceeded.

There are several reasons not to use the crack propagation capability of Abaqus directly, but to only use it to find the SERR. First of all the crack propagation prediction requires

that the crack path be pre-defined. This means it is poorly suited to predicting the direction a crack might take. Second, many iterations are required for the crack propagation calculations. This makes the analysis very computationally expensive. Third, the critical modal components of the SERR as well as the exponents in the crack growth criterion would have to be determined experimentally. Fourth and perhaps most important, this crack propagation model is ill-equipped to deal with delamination growth as a result of dynamic loading.

This last point deserves closer scrutiny, as it is an important point that often goes unacknowledged in the models presented in literature, despite being a short-coming of any critical SERR based propagation criterion. To understand why this is so, consider an FE model of a structure containing a delamination that is subject to fatigue loading. Maximum fatigue load is applied (quasi-statically) and the SERR at the nodes on the delamination front is computed. If the fracture criterion is exceeded at any node the delamination front is advanced and a new calculation is performed. This is repeated until an equilibrium is reached where the maximum fatigue load is applied to the structure, without the fracture criterion being exceeded at any node. At this point no further growth will occur. Simulating a new fatigue cycle will produce the same equilibrium when maximum load is reached, and so no new growth will occur. Therefore *absent an externally applied driving force in addition to the fatigue loading, a propagation model based on exceedance of a critical SERR criterion will predict that no delamination growth will occur, outside of an initial static growth spurt during the first fatigue cycle.* This is in blatant disagreement with the situation known to occur in reality, where fatigue loading will produce continuous delamination growth. All the above holds true not just for delamination growth, but for crack propagation in general.

The reason some models that are based on a critical SERR fracture criterion appear to correctly predict fatigue induced delamination growth is that they impose an extra driving force for delamination growth. An illustrative example is the model of Boscolo and Zhang [26]. In this model a crack in the substrate is included. It is the growth of this crack, and the resultant movement of the crack tip singularity, that provides the driving force for delamination growth. If the substrate crack is not allowed to grow, or is removed from the model completely, the model will predict static delamination growth during the first fatigue cycle and no further growth thereafter. However, as is shown by the experimental results of this thesis (discussed later) and the validation performed by Bosocolo and Zhang themselves [27] a fatigue load is in itself a sufficient driving force for delamination growth.

4.3 Numerical Models

Numerical models for the purposes of FEA were created in Abaqus for both the material coupons and the patch repair specimens. A short description of these models is given in this section.

4.3.1 Material Coupons

3D FEA was used to model the material coupons in order to be able to investigate different delamination front shapes. Apart from the Type I asymmetric (series A) and Type II symmetric (series B) specimens, a model was also made for the Type I symmetric specimens, as data from previous tests at DUT was available for that configuration as well.

The specimens were modelled as solids, using 8 node linear brick elements (Abaqus designation: C3D8). Quadratic brick elements are generally recommended [36], however in a 3D model the Abaqus integrated VCCT capability is only compatible with linear elements. Since large stress and strain gradients were expected near the delamination tips and the thickness steps full integration elements were used. Geometrically non-linear analysis was used since relatively large bending was expected to occur.

Since for the Glare grade used $E_x \approx E_y$ and the VCCT is an energy based method the Glare was modelled as an isotropic material. The adhesive layer itself was not included in the model as it is very thin and the stiffness of the adhesive is very low in comparison with the adherents. Thus the stress in the adhesive layer will be very small. The SERR is a concept derived from linear elastic fracture mechanics (LEFM), and thus all materials were modelled as linearly elastic.

Geometrically the FEA used a truncated model of the specimens, taking the end of the fillet radius as the cut-off. Figure 4.1 shows schematically the area used for the FEM and figure 4.2 shows an example of the model used for the Type II symmetric specimens. The ends of the model were constrained from displacement in the width and thickness directions and from all rotations. Displacement in the length direction was not constrained. The loading was applied as a pressure load on each of the two end surfaces, equal in magnitude to the fatigue stress being investigated.

Four elements were used in thickness direction in the substrate, two in the thin doubler and three in the patch in all three models. The element size in width direction remained constant, while the element size in length direction was reduced in the patched area and further reduced in the vicinity of the crack tip.

4.3.2 Patch Repair Specimens

The patch repair specimens were modelled in the same way as the material coupons. Again full-integration 8 node linear brick elements (C3D8) were used in a geometrically non-linear analysis. For the specimens with rounded patch corners, triangular wedge elements (C3D6) were used for the patch and the substrate area under the patch. Three elements were used in thickness direction in both the patch and the substrate. As both the patch and the base-plate were made out of Al-7075 the material was modelled as linear elastic and isotropic, with $E = 71.7$GPa and $\nu = 0.33$ (material properties from [33]). The end of the fillet radius was once again used as the cut-off of the model. Boundary conditions were applied at the top and bottom end. Deformation in width and thickness directions was constrained, while deformation in length direction (the same as the loading direction) was left unconstrained. All rotations were constrained. The loading was applied as a pressure load on the cross-section face.

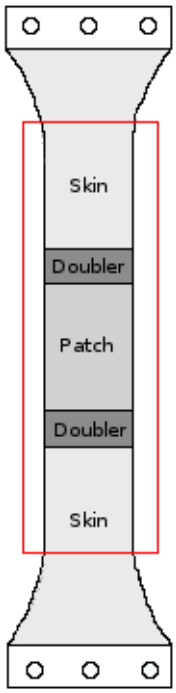

Figure 4.1: Schematic view of the Type I specimen. The red box indicates the area included in the FE model.

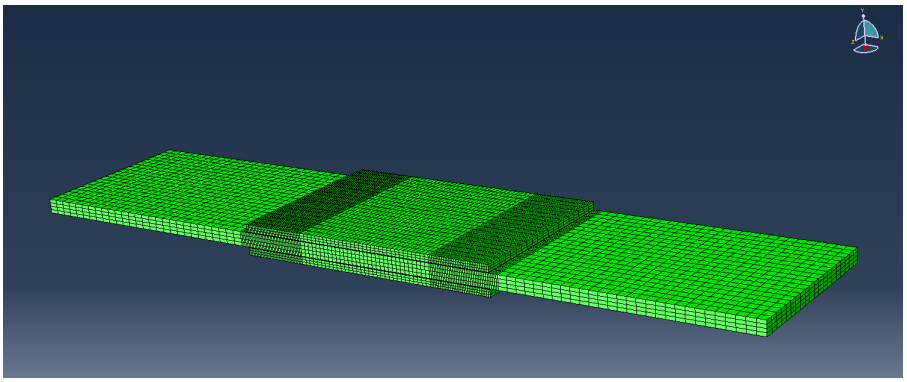

Figure 4.2: Mesh used for the FEA of the Type II symmetric specimens, with a delamination length of 30mm.

Chapter 5

Results of the Numerical Calculation of the Strain Energy Release Rate

This chapter discusses the results of the numerical calculations of the SERR. First the analytical and numerical methods for calculating G will be compared, then the variation of G as a function of various delamination shapes and sizes will be discussed. The chapter will mainly focus on the material coupons as they were more deeply studied while trying to gain an understanding of the behaviour of the SERR as a function of delamination size and shape. At the end of the chapter there will be a short discussion on the behaviour of the SERR in the patch repair configuration and the effect of different patch shapes. Unless specified otherwise all SERR values were found via the VCCT.

5.1 Comparison of Analytical and Numerical Methods for Calculating the SERR

As was mentioned in section 4.1 the analytical methods are only applicable to symmetric configurations with adherents with constant thickness, i.e. the Type II symmetrical specimens. Thus comparison between the analytical and numerical methods could only be done for that configuration. Analytical method C assumes that the patch and the substrate have the same Young's modulus and thickness. In this case the Young's modulus and thickness of the aluminium substrate were used. For the adhesive E =2160 MPa and G =842 MPa. Note that here G represents the shear modulus. The adhesive properties were taken from [37] and [38].

Table 5.1 shows a comparison of the SERR calculated using the different methods for a Type II specimen with a delamination length $b = 10$ mm and a stress level of 150 MPa. A 10 mm delamination means that there is a 10 mm long delamination from each of the four patch edges (two for the top patch and two for the bottom patch), see also figure 5.1. The VCCT value given is the average taken over the width of the specimen. Method A gives a difference in total SERR of about 7%, method B gives a difference of 26% and

method C gives a difference of 18%. This is to be expected as method A was developed for a configuration that matches that of the Type II symmetrical specimens, unlike methods B and C which consider a patch bridging a gap in the substrate (in effect, a single lap joint).

It should be noted that methods A and B predict that the SERR will be constant for any delamination length, whereas the numerical results predict that the SERR will vary as a function of delamination length. Another observation is that the difference in the modal distribution calculated by method C, compared to that calculated by the VCCT, is much larger than the error in the total SERR. A possible explanation is that the numerical calculations predict that the debonded section of the patch will bend away from the substrate, which was indeed observed during the experiments. This will obviously increase the peel (i.e. mode I) component. Analytical method C does not account for this bending effect. Although this method still allows a somewhat correct determination of how much energy is released by the delamination growth, it would seem that the information on *how* this energy is released is lost.

In summary, method A agrees reasonably well with the VCCT, whereas method B and C do not. This is not so surprising if one considers that method A was developed for a configuration that closely matches that of the type II specimen, whereas method B and C where developed for a different configuration. Since the analytical methods all assume a symmetrical structure it was decided to use the SERR values calculated via the VCCT for the remainder of the thesis.

	Method A	**Method B**	**Method C**	**VCCT**
G_{tot} [N/mm]	0.286	0.337	0.317	0.268
G_I [N/mm]	-	-	0.0047	0.074
G_{II} [N/mm]	-	-	0.313	0.179
Difference	6.72%	25.75%	18.28%	0.00%

Table 5.1: Values of the SERR calculated using various methods for a Type II symmetric specimen with b=10mm and S=150 MPa. The difference is the relative difference with respect to the value calculated using the VCCT method.

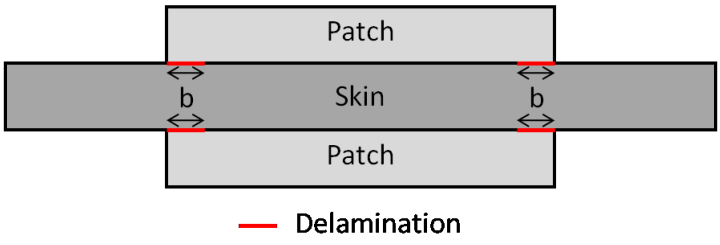

Figure 5.1: Definition of delamination length b.

5.2 SERR as a Function of Delamination Length

Figure 5.2 shows the SERR calculated for a number of prescribed delamination lengths for each of the three material coupon specimen configurations for which test data was available. The delamination front was defined as straight across the specimen width and normal to the specimen sides.

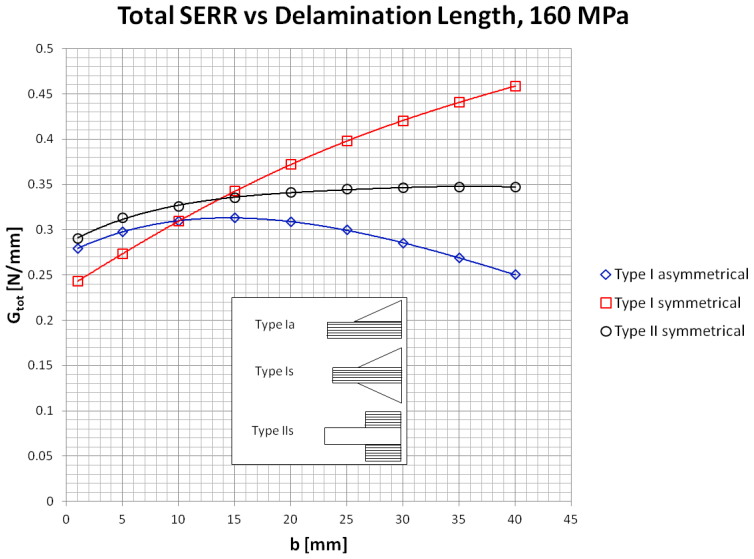

Figure 5.2: Total strain energy release rate as a function of delamination length for the three configurations tested, at an applied stress of 160 MPa. The lines are 4th order polynomial trendlines through the calculated points.

All three specimens start with G increasing with increasing delamination length. However the continued behaviour is quite different. In the case of the Type II symmetric specimen the increase of G slows, with the SERR becoming almost constant for a delamination length of 20 mm and greater. For the type I symmetric specimen the increase of G is continuous over the entire range of delamination lengths considered. The likely explanation for this is that as the delamination length increases the cross-sectional area at the delamination front increases (as a result of the patch taper). Thus a greater volume is available for storage of strain energy and the amount of strain energy released by further delamination growth is greater. For the Type I asymmetric specimen G decreases as the delamination length increases past 15 mm. The most likely reason for this is that unloading of the patch as the delamination grows is much greater in the asymmetric case than in the symmetric case as a result of the secondary bending and the progressive shift of the neutral axis due to the taper.

The benefit of applying taper in this case is masked by the configuration differences between Type I and Type II specimens, specifically by the materials used. For the Type I specimens the patch has a higher modulus of elasticity, since Al-7175 is stiffer than the Glare grade used. This means that the patch will attract more load (given the same thickness) and thus the SERR will be greater. That taper does in fact provide a benefit can be seen in figure 5.3. To produce this figure the FEA was re-run on a Type II symmetric

configuration but with aluminium used as the material for the patch and Glare used as skin material (so switched with respect to the actual configuration). The benefit of taper can now be clearly seen, as G for the Type I (tapered) specimen is initially only half of G for the Type II (untapered) specimen and remains significantly lower for all delamination lengths.

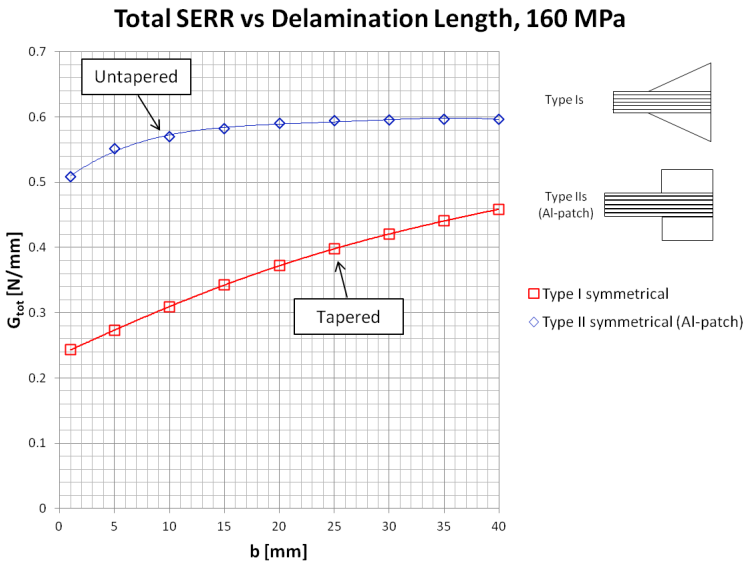

Figure 5.3: Comparison between G vs b behaviour for a Type I (tapered) symmetrical configuration and a Type II (untapered) symmetrical configuration if both used the same materials for the patch and the skin. This figure shows clearly the benefit of applying taper; a benefit that was hidden by the change in materials in the actual specimens.

It also appears that secondary bending is *beneficial* in the case of delamination, as it reduces the SERR, especially for longer delamination lengths. This is not unexpected, as the specimen will bend towards the patch (i.e. the patch is on the inside of the bending radius). However it is in contrast to traditional fatigue problems in metals, where the bending will tend to further open the crack.

5.3 Modal Distribution of the SERR

Use of the VCCT allows separate calculation of the three modal components of the SERR. The modal distribution as a function of b shown in figure 5.4 through figure 5.6. Also shown is the mode-mix angle, defined as:

$$\psi = \arctan\left(\frac{G_{II}}{G_I}\right) \tag{5.1}$$

For all three configurations the largest component of the SERR is mode II, and the smallest is mode III. The mode mix angle remains roughly constant with delamination length for the Type II and Type I symmetric specimens. The Type I asymmetric specimen

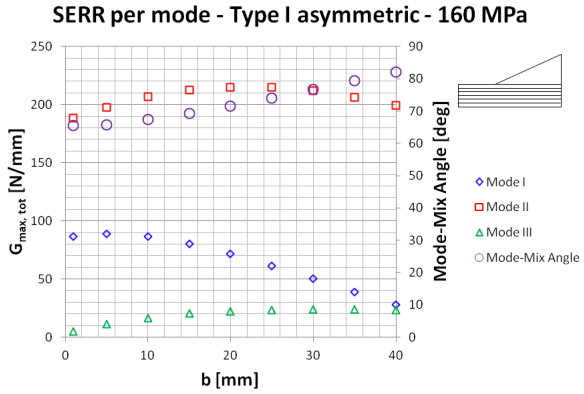

Figure 5.4: Distribution of the modal components of the SERR as a function of delamination length for a Type I asymmetric specimen.

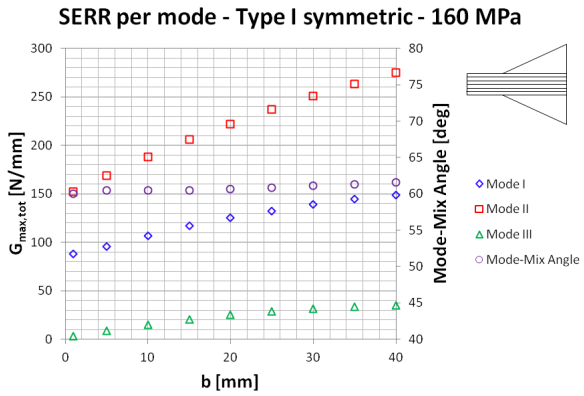

Figure 5.5: Distribution of the modal components of the SERR as a function of delamination length for a Type I symmetric specimen.

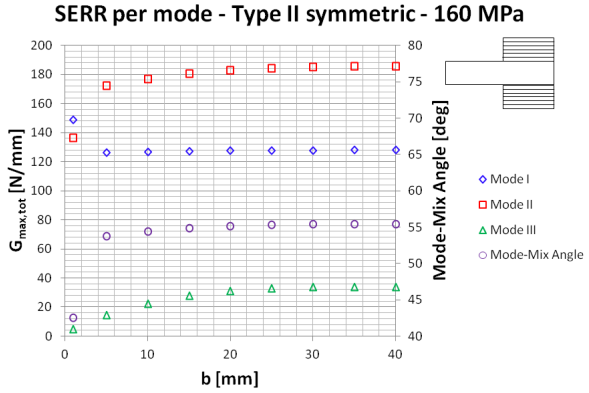

Figure 5.6: Distribution of the modal components of the SERR as a function of delamination length for a Type II symmetric specimen.

rapidly approaches pure mode II as the delamination grows, but the two symmetric configurations clearly experience mixed-mode loading. Figure 5.4 shows that the increase of the mode-mix angle for the Type I asymmetric specimen is driven by the drop in mode I loading being larger than the drop in mode II loading as the delamination grows.

A number of mechanisms will effect the mode mix. The mode I component will be influenced by the known peel stress distribution for a laminate where the laminae have differing lateral stress [39], as shown in figure 5.7. This will cause a small rise in the mode I component near to the edges of the specimen and a drop in mode I at the edge itself.

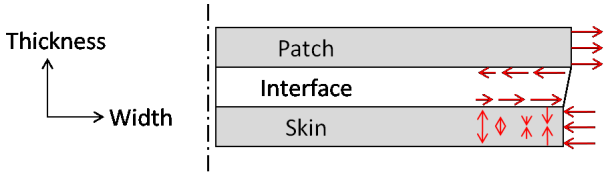

Figure 5.7: Stress distribution in the specimen cross-section, with the cut made at the delamination tip. The difference in Poisson ratio, combined with spring-back of the disbonded portion of the patch, result in a difference in the stress in width direction. This causes bending of the patch and skin and a non-constant peel stress distribution.

The mode III distribution is determined by two factors. One is the difference in Poisson ratio between the patch and the skin, resulting in a different contraction in width direction. In the asymmetric configuration this effect is magnified by the secondary bending, which causes a non-uniform distribution of strain in length direction. As a result the Poisson contraction is also non-uniformly distributed through the thickness. The other factor determining the mode III distribution is the elastic spring-back in width direction of the disbonded portion of the patch, which will cause a stress in width direction away from the centre line of the specimen in the bonded portion of the patch, but not in the substrate.

The free edge is expected to cause a peak in the mode III and mode II distributions. This may be seen to some extent in the results of Boscolo and Zhang [27] shown in figure 2.3. The delamination length is somewhat greater at the edges of the specimen. This is what would be expected if the SERR was locally higher there.

The modal distribution of the SERR over the width of the specimen is shown in figure 5.8 through figure 5.10.

For all specimens both the mode II and mode III components show a steep rise towards the specimen edges as expected due to the free edge. Further numerical analysis was conducted to investigate this behaviour. A 2 mm wide strip at the edge of the delamination front was advanced by a short distance. This caused the stress concentration that is normally present at the edge of the specimen to move inward. This is illustrated in figure 5.11. This behaviour suggests that although the delamination may grow faster at the edges, the difference in growth rate is checked by redistribution of stress if the edges advance too far with respect to the remainder of the delamination front. Thus in reality it is likely there a balance in the mechanism which will result in a slightly curved delamination front, minimising the SERR. This shape can be see in the experimental results of Boscolo and Zhang [27] shown in figure 2.3.

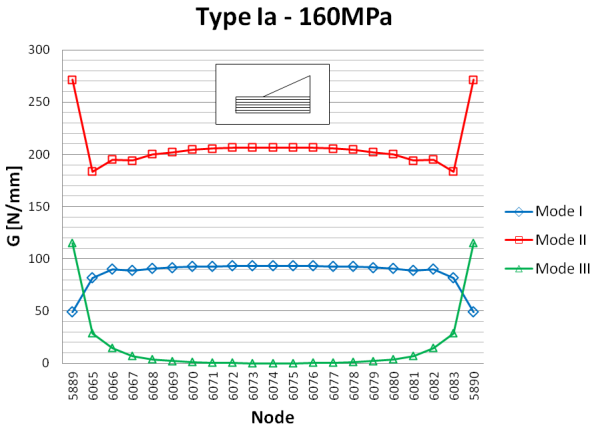

Figure 5.8: Distribution of the SERR components over the specimen width for a Type I asymmetric configuration with a 10 mm delamination.

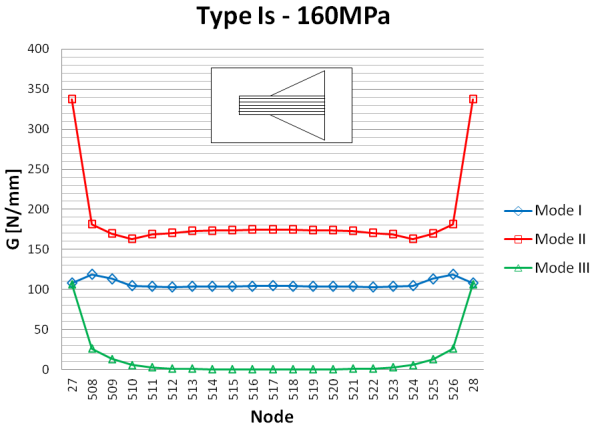

Figure 5.9: Distribution of the SERR components over the specimen width for a Type I symmetric configuration with a 10 mm delamination.

The effect of the peel stress distribution across the width can also been seen to some extent in figure 5.8 through 5.10. For the asymmetric configuration the expected rise in the mode I component is not present and the drop is far more pronounced. This is likely due to the fact that the bending about the length-axis reduces the peel stresses. This bending is a result of the bending about the width axis of the specimen. As a result of the bending about the width axis the strain in length direction is not constant through the cross-section of the specimen. Thus the contraction in width direction of the patch and substrate will also be non-uniform through the thickness. This effect is enhanced by the difference in Poisson ratios between the skin and the patch.

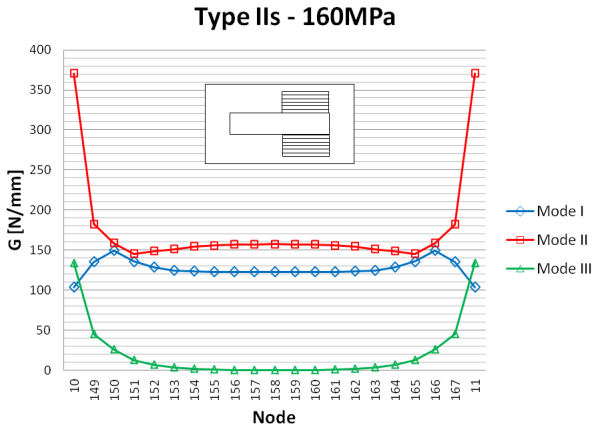

Figure 5.10: Distribution of the SERR components over the specimen width for a Type II symmetric configuration with a 10 mm delamination.

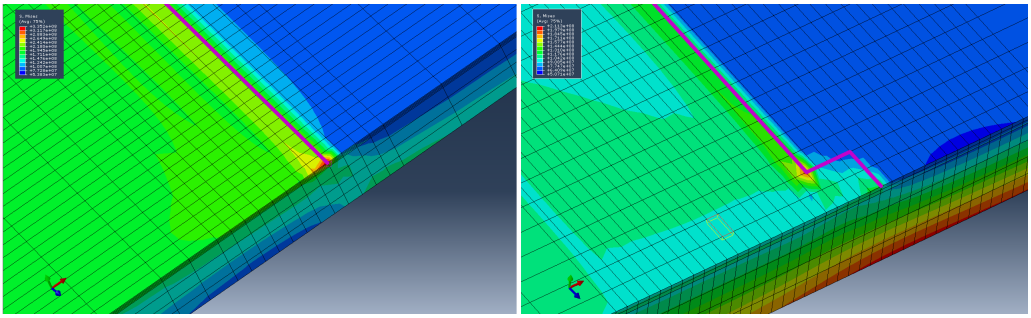

Figure 5.11: Stress distribution in the substrate around the delamination front as determined by FEA. The delamination front is drawn in purple. The image on the left shows a straight delamination front, the image on the right shows the situation where a 2 mm strip at the edge has advanced ahead of the main front. This causes the stress concentration to move inward, suggesting the delamination front will straighten if the edges advance too far ahead of the main front. The visibility of the patch has been suppressed in these images.

5.4 Effect of Asymmetric Crack Growth

Due to various effects (e.g. material inhomogeneity, imperfect manufacturing, etc) it is expected that delamination growth rate in practice will not be equal for all the delaminations that are present. Thus the effect of having delaminations of different lengths in a specimen was investigated numerically.

For the type I asymmetric configuration the length of one delamination was fixed. The length of the second delamination was varied from 10 to 40 mm in steps of 5 mm. The VCCT was then used to calculate the SERR for each delamination increment. Figure 5.12 shows schematically one of the delamination configurations used. The results are shown in figure 5.13.

The mode II, mode III and total SERR are lower for the shorter delamination for all delamination lengths. The difference increases as the delamination length difference in-

Figure 5.12: Example of a delamination configuration used in the investigation of asymmetric delamination growth in a type I asymmetric specimen.

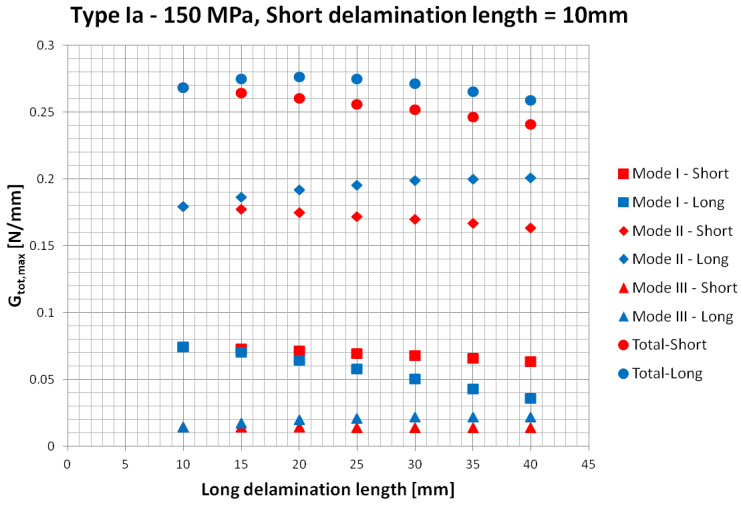

Figure 5.13: SERR for differential delamination growth in a Type I asymmetric specimen. The delamination nomenclature is illustrated by figure 5.12.

creases. This indicates that any difference in the length of the two delaminations will be magnified as the delaminations grow. The largest difference in the total SERR occurs for a long delamination length of 40 mm, at which point the difference in total SERR is approximately 11% with respect to the lower value. For the mode I component it is the shorter delamination that has the largest value. This allows the following prediction: If the mode I component provides the driving force for delamination, in the case of asymmetric delamination growth the shorter delamination should grow faster than the longer delamination, reducing the length difference. If on the other hand the driving force is provided by mode II, mode III, or the total SERR the longer delamination will grow faster, increasing the length difference. Another important observation from figure 5.13 is that which delamination has the highest SERR does not change with respect to delamination length. This was assumed to also hold true for the symmetric configurations when investigating their asymmetric growth behaviour.

Following the numbering in figure 5.14 the cases listed in table 5.2 were considered for the symmetrical configuration. Due to symmetry these cover all the possible configurations. The results are shown in table 5.3 As with the asymmetric configuration the longer delaminations always had a higher SERR. However if a long and a short delamination were on opposite sides of the thickness of the skin (Cases 1, 3 and 4) the difference in SERR was found to be far more pronounced than if a long and a short delamination were on the same side of the skin (Case 2). For example for $b_1 = b_2 = 10$mm and $b_3 = b_4 = 25$mm the difference in total SERR was already 57% with respect to the higher value. This is because if the delaminations on opposite sides of the skin thickness have different lengths

the configuration will become asymmetric. Thus there will be secondary bending, which will act to close the short delamination. This bending is shown in figure 5.15.

Figure 5.14: Delamination numbering definition.

Delamination	Case 0	Case 1	Case 2	Case 3	Case 4
b_1 [mm]	10	10	10	10	10
b_2 [mm]	10	10	10	15	10
b_3 [mm]	10	15	25	10	10
b_4 [mm]	10	15	25	15	15

Table 5.2: Cases investigated for asymmetric delamination growth on a symmetric specimen. Numbering of the delaminations is in accordance with the definition shown in figure 5.14.

Case	Case 0	Case 1	Case 2	Case 3	Case 4
Location 1	0.286	0.179	0.175	0.286	0.290
Location 2	0.286	0.179	0.175	0.295	0.176
Location 3	0.286	0.400	0.406	0.288	0.283
Location 4	0.286	0.400	0.406	0.293	0.404

Table 5.3: SERR in N/mm at each of the four delamination locations, for each of the asymmetric growth cases investigated. Numbering of the locations is in accordance with the definition shown in figure 5.14.

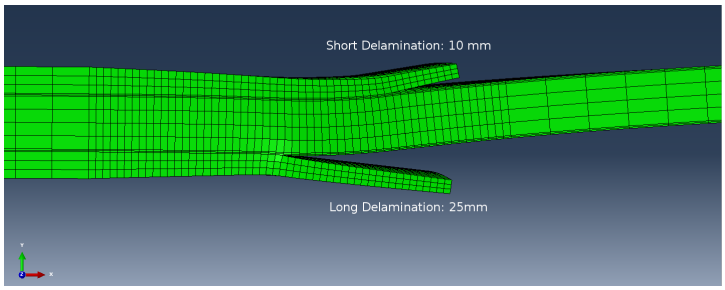

Figure 5.15: Secondary bending caused by asymmetric delamination growth. The bending causes closure of the shorter delamination. A scale factor of 50 has been applied to the magnitude of the deformations to enhance visibility.

5.5 Effect of Different Delamination Shapes

All the analyses described so far have assumed a straight delamination front running across the entire width of the specimen. However it may be expected that delaminations

in service are not necessarily straight. Therefore a number of delamination shapes were investigated, as shown in figure 5.16. The computed stress distributions are presented in figure 5.17. As the shear stresses play an important role, figure 5.17 shows the von Mises stress, to inlcude these stresses. As a comparison figure 5.18 shows only the normal stress in loading direction. For all the shapes there is a stress concentration at or near the edge of the patch. The stress concentrations are located on the sides of the delamination, rather than ahead of it. This suggests that the delamination front will tend to 'straighten-out' as the delamination grows. Thus no matter the starting shape of the delamination it will eventually develop a straight delamination front across the width of the specimen. This lends support to the validity of determining the delamination length by measuring the length at the side of the patch.

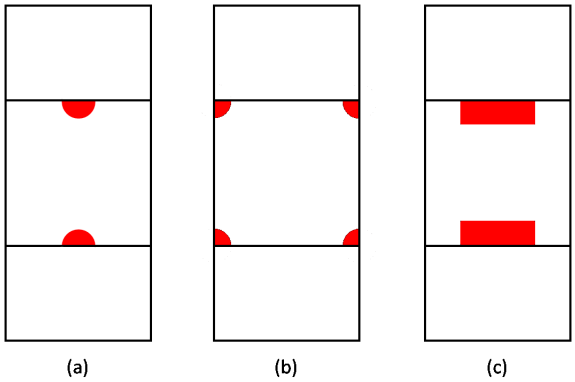

Figure 5.16: Delamination shapes analysed: (a) half penny-shaped delamination in the centre of the patch edge; (b) Quarter-circular delaminations from the patch corners and (c) rectangular crack in the centre of the width.

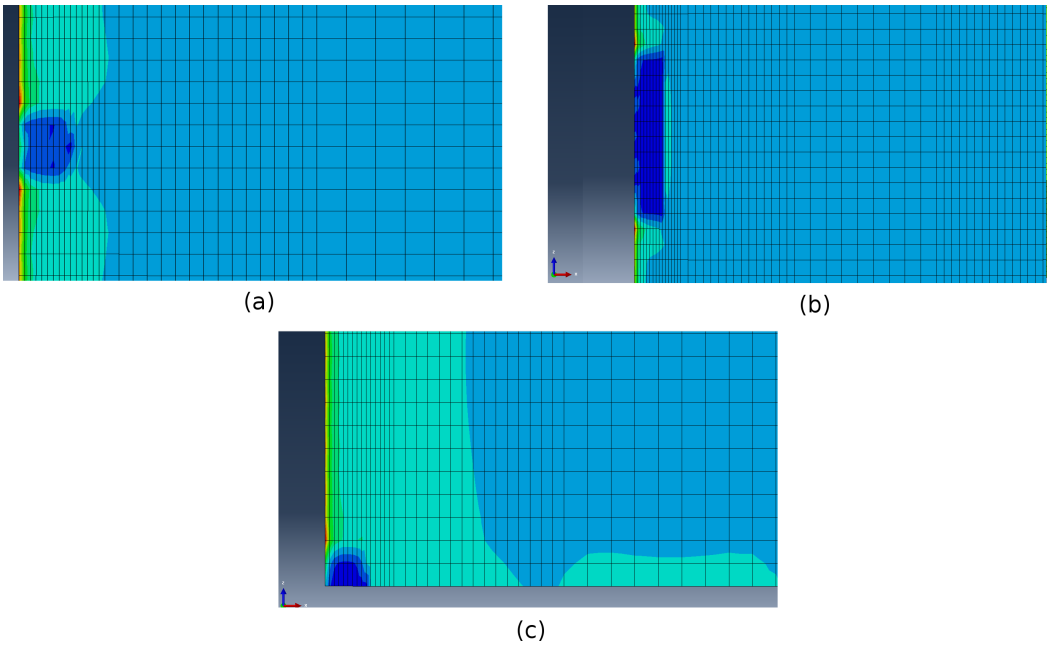

Figure 5.17: Results of FEA showing the von Mises stress distribution on the underside of the patch for various delamination shapes: (a) a half-penny shaped delamination in the centre of the patch width; (b) quarter-circular delaminations from the patch corners and (c) rectangular crack in the centre of the width. Areas of highest stress are in red, areas of lowest stress are coloured blue.

5.6 SERR in the Patch Repair Configuration

The SERR as a function of delamination length was also calculated for the patch repair specimens. The delaminations were defined as a strip over the full width of the patch, with the delamination front normal to the loading direction. This definition is shown in figure 5.19.

An anomalous behaviour was noticed in the numerical models for the patch repair specimens, the cause of which is not known. The behaviour concerns the two nodes on the substrate surface at the edge of the patch on the delamination front. These locations of these nodes, labeled A and B, are shown in figure 5.20. Although the figure shows the square cornered patch (specimen C1) the same behaviour was observed for all other specimens as well, with the nodes exhibiting the anomalous behaviour advancing with the delamination front.

The anomalous behaviour was the following: One would expect the mode II SERR at these nodes to be higher than the mode III SERR. For node A that was indeed the case. However for node B the values for mode II and mode III SERR were switched with respect to node A, which does not agree with the expected behaviour based on the physics of the problem. Thus it is thought that this is purely a numerical artifact, though the exact cause remains unknown.

Three methods of dealing with the anomalous behaviour were investigated: Accepting the numbers as calculated; switching the mode II and mode III values at node B (matching

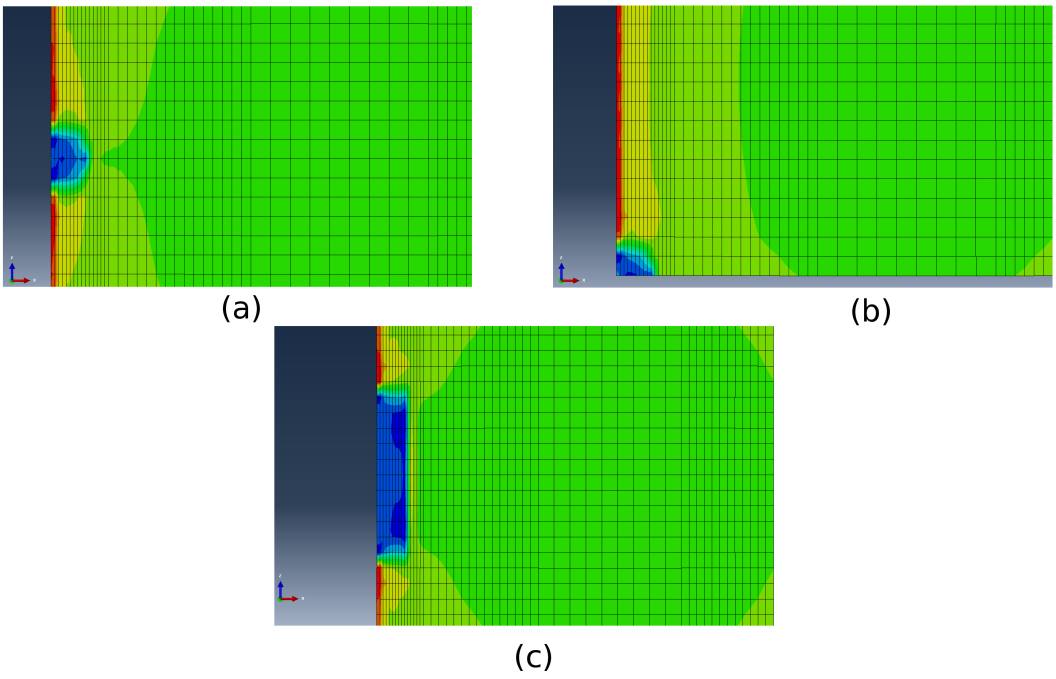

Figure 5.18: Results of FEA showing the distribution of normal stress in loading direction on the underside of the patch for various delamination shapes, as identified in figures 5.16 and 5.17. Areas of highest stress are in red, areas of lowest stress are coloured blue.

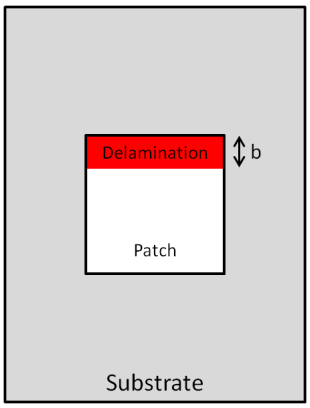

Figure 5.19: Delamination length definition used for the numerical analysis of the patch repair specimens.

the values at node A and what would be expected based on the physics) and completely discarding the SERR values for both nodes A and B. The results of these strategies for the 10 mm corner radius patch (specimen C2) are shown in figure 5.21, which shows the total SERR, and figure 5.22, which shows the mode II SERR. The SERR values shown are the average over all nodes in width direction.

The blue diamonds show the SERR values if all nodes are considered. The red squares show the SERR if the mode II and mode III values at node B are switched. It can be seen that in both these cases there is a sudden jump in the SERR values for a delamination

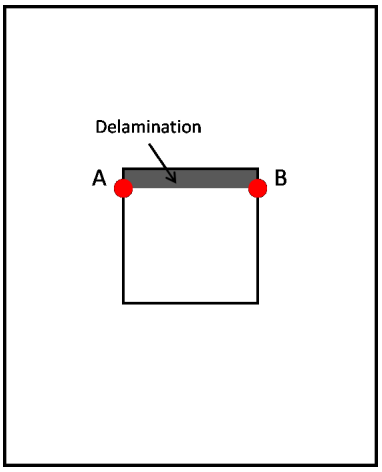

Figure 5.20: Location of the nodes on the delamination front at the patch edge

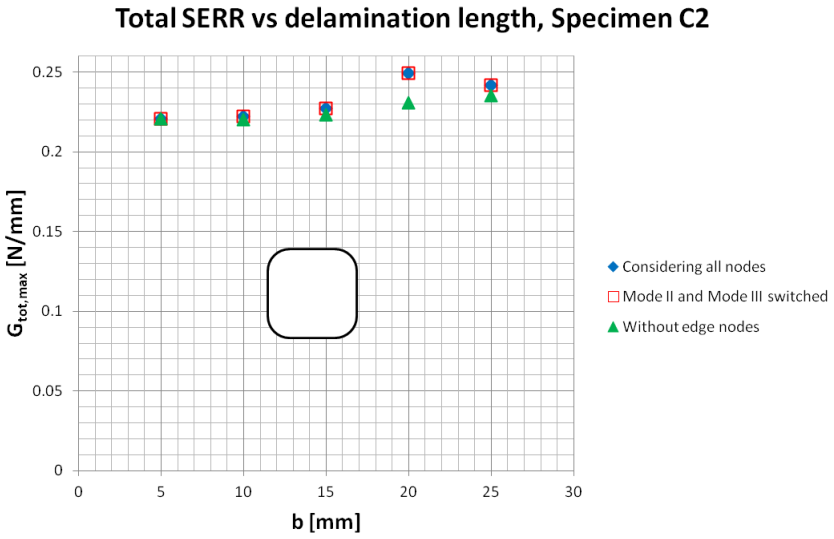

Figure 5.21: Total SERR vs delamination length for the 10 mm corner radius patch, comparing the three methods for dealing with the anomalous behaviour at the patch edge nodes.

length of 20 mm. There is no obvious physical reason for this jump. The green triangles show the SERR values if values for the nodes at the patch edges (so both A and B) are discarded. In this case the G vs b curve is much smoother, which is closer to what is expected to happen in reality. Thus it was thought that discarding the SERR values for the nodes at the patch edge produces the answer that is closest to the actual behaviour of the specimen. Consequently this method was applied for the numerical analysis of all patch repair specimens.

For the specimen investigated the difference in calculated SERR if the values at these nodes are discarded, compared with if they are not, is greatest for a delamination length of 20 mm. The difference is approximately 8% in mode I, 3% in mode II and 8% in total SERR. The difference in mode III is 75%, however in absolute terms the difference is of

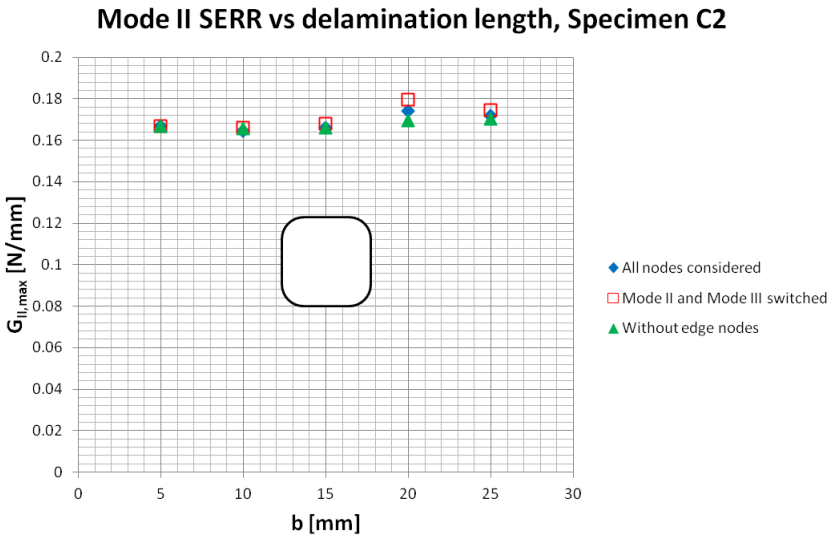

Figure 5.22: Mode II SERR vs delamination length for the 10 mm corner radius patch, comparing the three methods for dealing with the anomalous behaviour at the patch edge nodes.

the same size as the difference in mode I and mode II.

Discarding the SERR values at nodes A and B and averaging the values at the other nodes gives the G vs b behaviour as shown in figure 5.23 for the total SERR, in figure 5.24 for the mode I SERR, and in figure 5.25 for the mode II SERR.

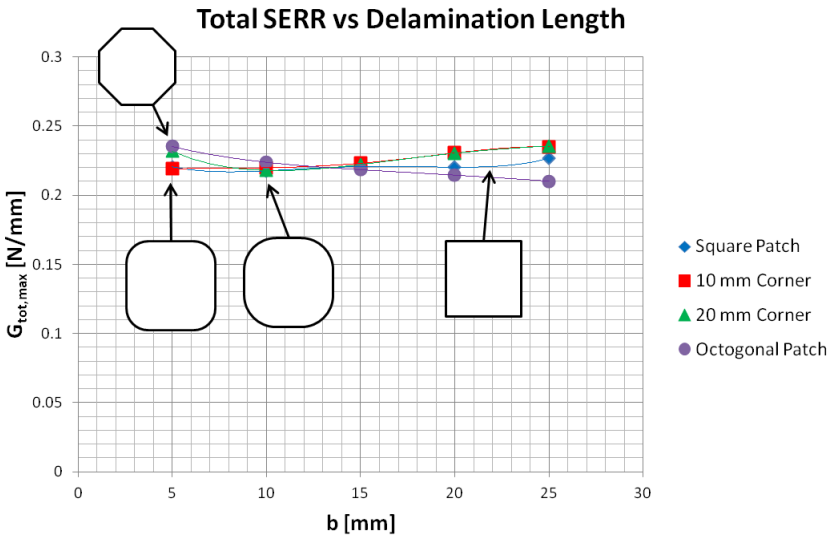

Figure 5.23: Total SERR vs delamination length for the patch repair specimens, including 4th order polynominal trendlines.

The SERR remains roughly constant over the entire range of delamination lengths studied, though there is a downward trend visible for the octagonal patch, possibly correlated to

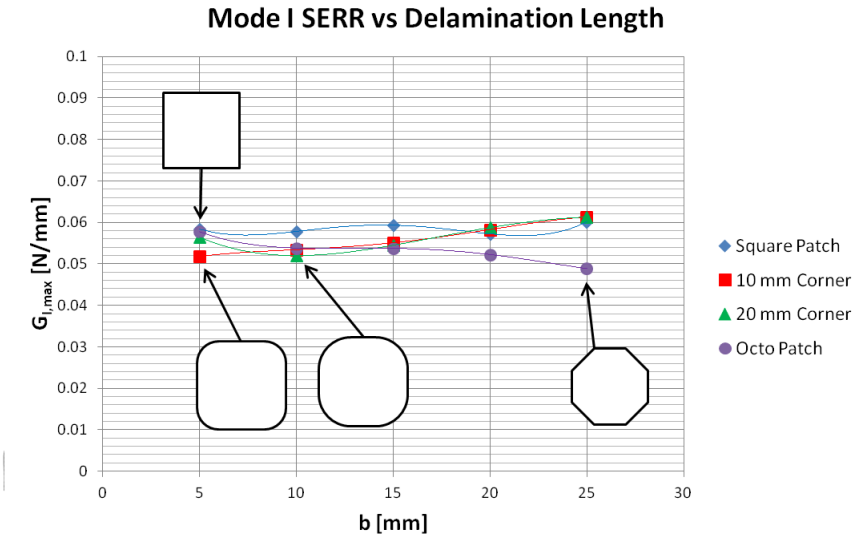

Figure 5.24: Mode I SERR vs delamination length for the patch repair specimens, including 4th order polynominal trendlines.

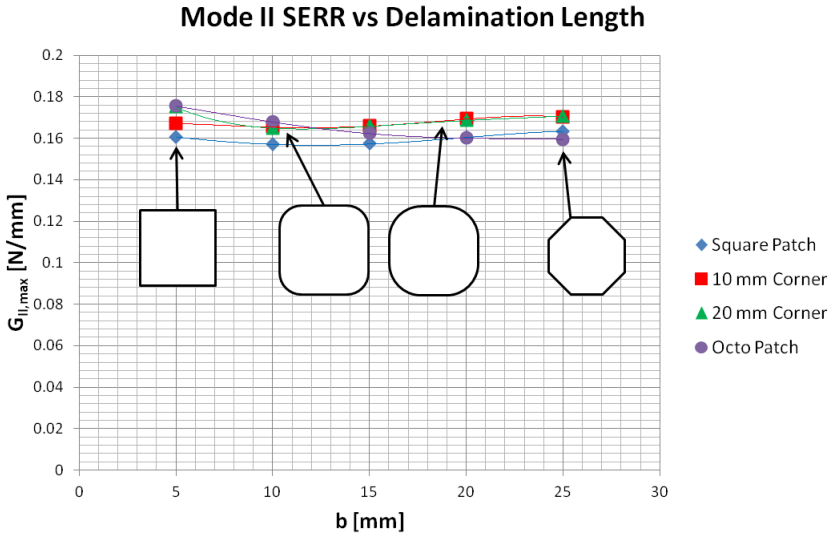

Figure 5.25: Mode II SERR vs delamination length for the patch repair specimens, including 4th order polynominal trendline.

the increasing width of the patch at the delamination front as the delamination grows. There is little difference in the SERR for the different patch shapes, suggesting that the influence of the patch shape on delamination growth will be minimal, at least for the shapes investigated.

Chapter 6

Test Results

This chapter discusses the experimental results. As in previous chapters, the first part will deal with the material coupons, the second with the patch repair specimens. The experimental observations and measurements will be presented and compared with the results from the numerical analyses discussed in chapter 5. Unless otherwise specified all SERR values were obtained by numerical analysis using the VCCT.

6.1 Series A

The series A specimens were of type I asymmetric configuration, so with a Glare skin and an aluminium patch. Both specimens were loaded as described in chapter 3. Delaminations started at the edges of the patch and grew as the test progressed. At a later stage of the test one or more cracks appeared in the metal layer of the Glare skin. In the case of specimen A1 a crack developed at the run-out of the fillet radius (far from the patch), and testing was stopped when the crack grew beyond half the width of the specimen. For specimen A2 multiple cracks developed in the vicinity of the patch edge and at the edge of the thin doubler. These cracks also caused delamination within the Glare skin itself, with in one case the delamination overtaking the delamination between patch and substrate. At this point testing was stopped. Using the designations as defined in figure 6.1, the results of the delamination length measurements have been plotted in figure 6.2. As moving the camera was not practical delamination length measurements were only performed for locations 3 and 4. Delamination length was defined as the distance in specimen length direction (which is the same as the direction of loading) from the mouth of the delamination to the tip, as shown in figure 6.3. A separate graph for each specimen has been included in Appendix A.

In the graph two phases can be identified. First there is a phase of almost no growth (lasting from 50 to 100 kcycles for specimen A1 and for the first 25 kcycles for specimen A2). Then there is a phase where the delamination length curve is approximately linear for a relatively long period and then slowly drops off. For specimen A2 the drop-off is

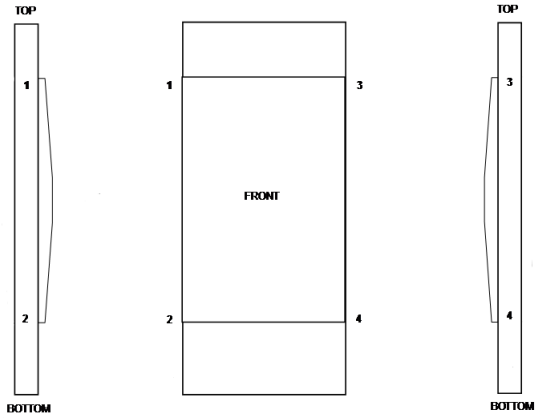

Figure 6.1: Nomenclature used for series A specimens. Adapted from a figure by C. Rans (unpublished).

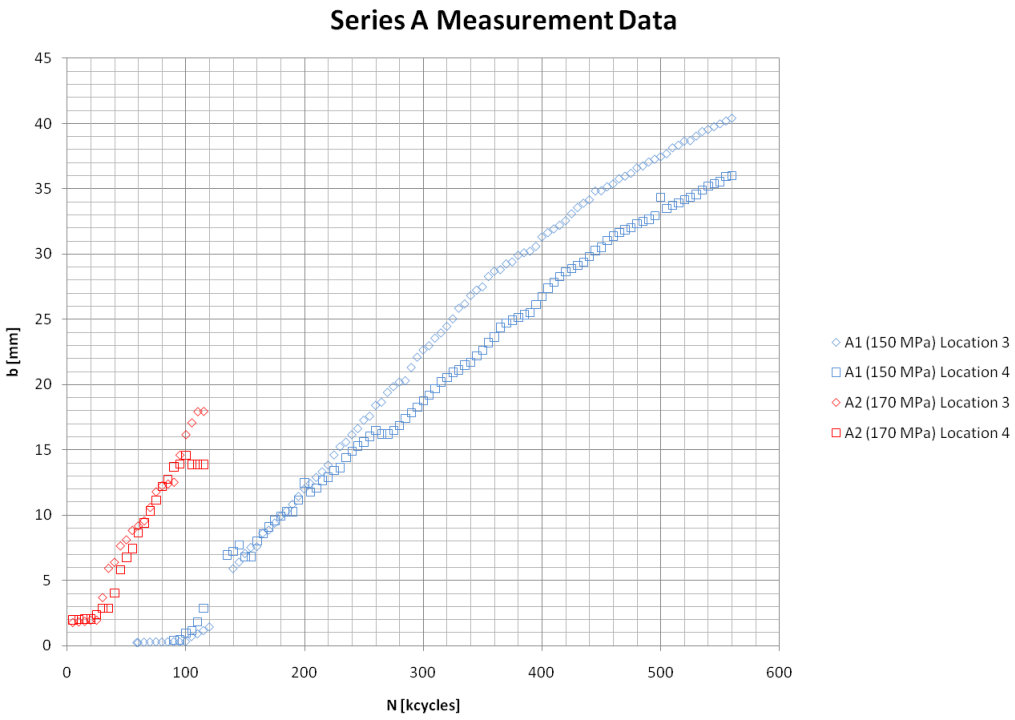

Figure 6.2: Measurement data for the Series A specimens.

rather sudden. This is thought to be caused by cracking and delamination of the Glare skin causing unloading of the patch.

The first phase seems to correspond with an initiation phase of delamination growth. The locations of the stress concentration as predicted by the numerical analysis discussed in section 5.5 suggest that the apparent lack of delamination growth could be caused by an initial delamination first growing in width direction, with growth in length direction only occurring after the delamination has become uniform over the width of the specimen. The numerical analysis predicts that for a delamination that is not uniform across the

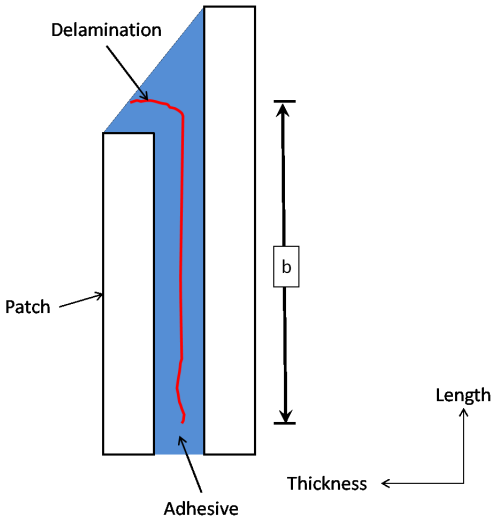

Figure 6.3: Definition of delamination length b. Delamination length was defined from the mouth of the delamination to the tip of the delamination. As the objective of the test was to measure delamination growth rate a fixed length offset will not affect the results of the test.

width the stress concentrations, and the locations of highest SERR, won't be ahead of the delamination front, but rather to the sides. This suggests that the delamination front will straighten out across the specimen width before growing in loading direction.

The second phase corresponds with the predicted behaviour of the SERR as a function of b, as discussed in section 5.2 and shown in figure 5.2. There is almost constant growth for delamination lengths between 5 and 30 mm, with a drop off in delamination growth rate past 30 mm. This matches the behaviour of G for a Type I asymmetric specimen predicted by the numerical model and shown in figure 5.4.

In the curves for location 4 on both specimens A1 and A2 a similar 'plateau' is visible in the delamination length. For specimen A2 this occurs around 100 kcycles, just before the end of the test. For specimen A1 this occurs around 260 kcycles. Although the behaviour appears to be similar the cause is thought to be different. For specimen A2 multiple fatigue cracks had already formed in the substrate at this point in the test. This cracking caused delamination within the Glare substrate itself, with one delamination overtaking the delamination in the patch-doubler interface. This is thought to have shielded the delamination in the patch-doubler interface, halting delamination growth there. For specimen A1 the plateau is thought to have been caused by an inadvertent shift of the datum point used during the delamination length measurements (i.e. measurement error). This is supported by the slope of the delamination length curve being equal on both sides of the plateau and the absence of any fatigue cracking at that point in the test.

Especially for specimen A1, it can be seen that the delamination length curves diverge. That is to say, the difference in delamination lengths between the two delaminations measured becomes greater as the number of cycles increases. As was demonstrated in section 5.4, this means that in the delamination growth phase the mode I component is not the dominant influence. This is in accordance with what has been reported in literature [7, 40].

6.2 Series B

Series B consisted of type II symmetric specimens, so with an aluminium skin and Glare patches. Six specimens were tested. However as mentioned in chapter 3 the use of the climate chamber required the use of a lens with a smaller magnification on the camera used to measure the delamination length. This made it harder to identify the delamination tip and as a result there were no valid measurements for the first specimen (B1). The measurements for the other five specimens are shown in figure 6.4, with the nomenclature as defined by figure 6.5. For all the specimens there is a 'fast' and a 'slow' delamination. Thus in order to improve legibility of the graph figure 6.4 was split into figure 6.6, showing only the fast delaminations, and figure 6.7, showing only the slow delaminations. Graphs for each specimen separately can be found in Appendix A.

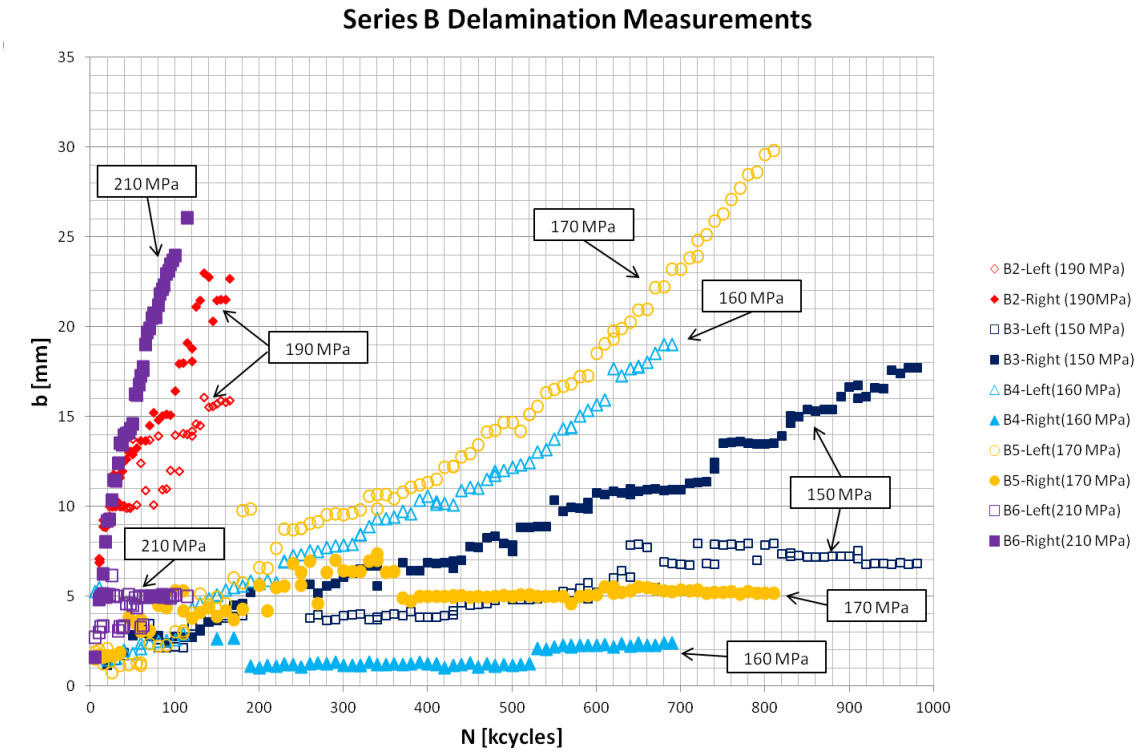

Figure 6.4: Measurement data for the series B specimens.

Specimens B1, B3, B4 and B6 failed due to fatigue cracking in the aluminium skin. For specimen B6 the fatigue crack was located a bit below the fillet radius. For the other specimens cracking occurred in the area under the patch, just beyond the patch edge. Due to time constraints specimens B2 and B5 were removed from the test machine while still intact after sufficient delamination measurements had been performed. The presence of adhesive residue on both the skin and the patch surface indicates delamination occurred due to cohesive failure of the adhesive.

Unlike for the series A specimens the delamination length curve remains roughly linear for series B, with no drop-off at longer lengths. This confirms the numerical analysis, which

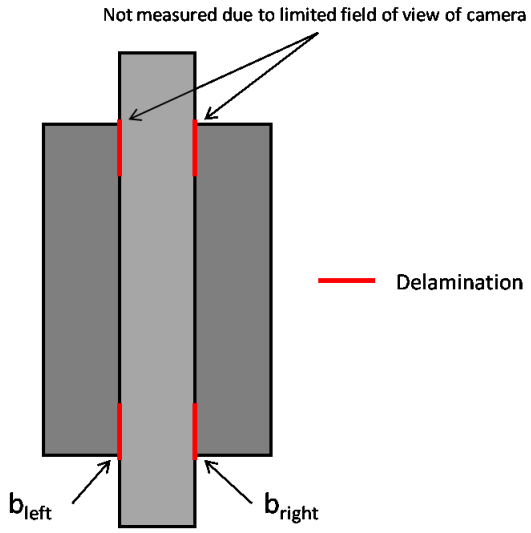

Figure 6.5: Nomenclature used for series B specimens.

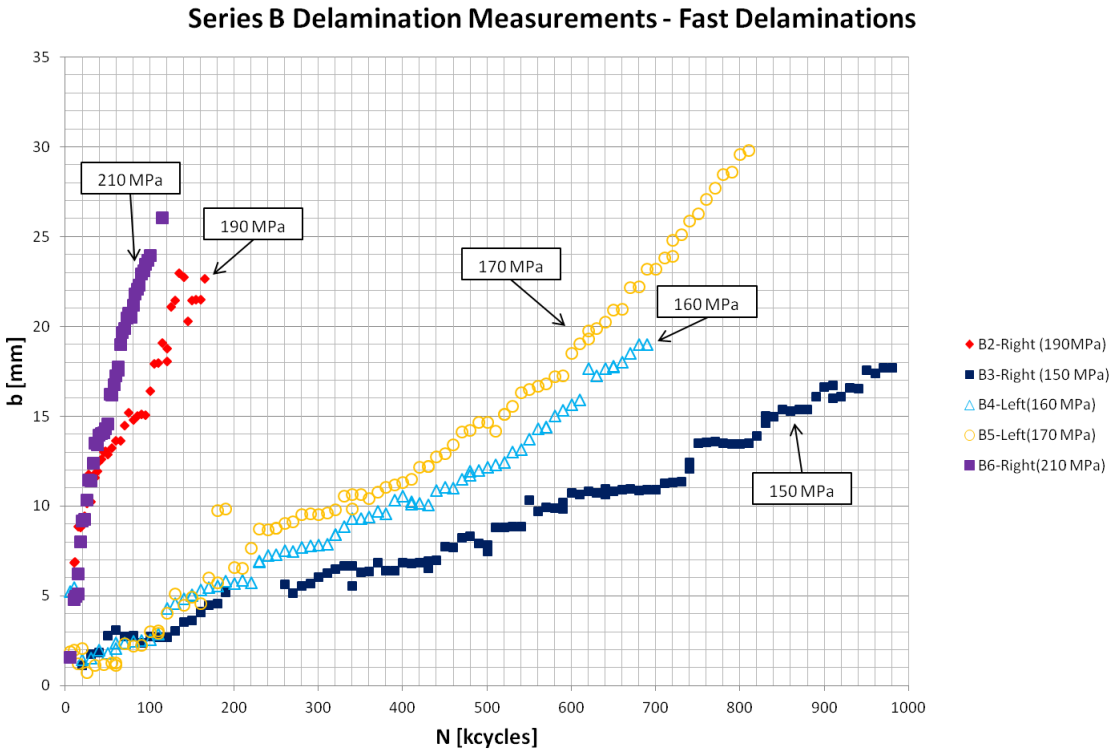

Figure 6.6: Measurement data for the fast delaminations of the series B specimens.

shows that for the type II symmetric configuration G remains more or less constant, even at longer delamination lengths.

Extending a linear trendline through the measurement points it will intersect the b-axis above the origin. This indicates that either there was an initial flaw present in the bond

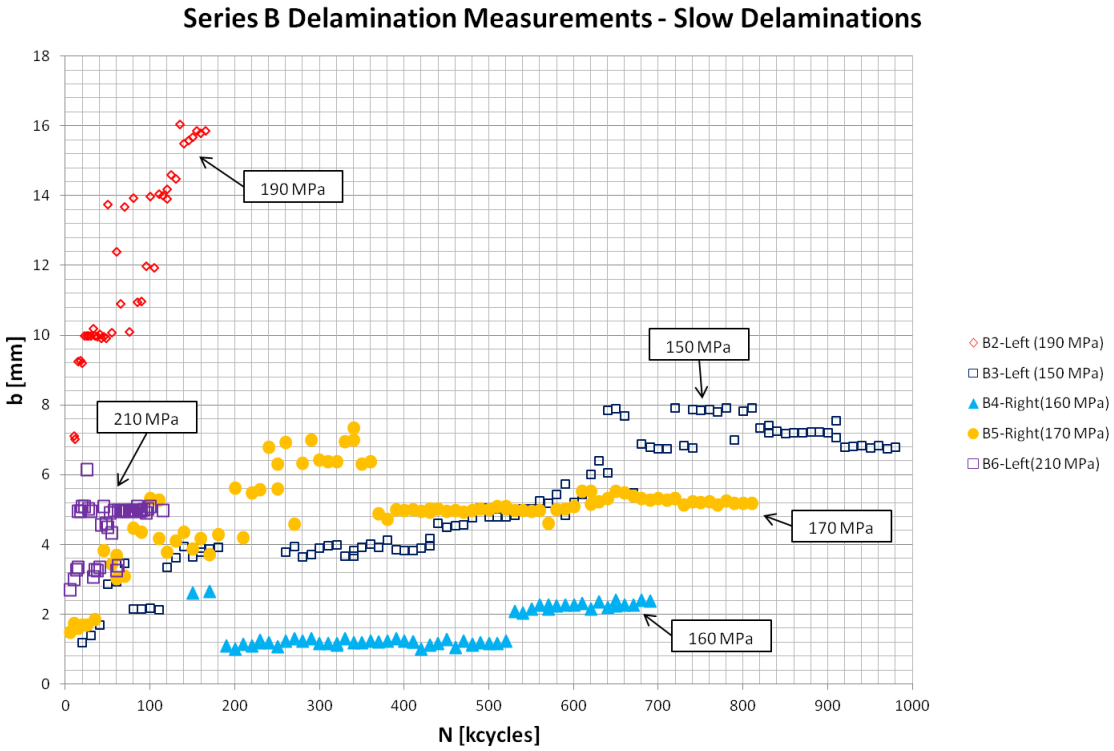

Figure 6.7: Measurement data for the slow delaminations of the series B specimens.

line or that there was an initial period of fast growth (before the first measurement point). The second has been reported for delamination in FMLs [7].

The fast and slow delaminations for each specimen diverged, confirming the numerical analysis discussed in section 5.4. On the basis of that analysis the large difference in growth rate was expected. However the analysis does not explain why the growth rate difference was much larger for specimens B4, B5 and B6 than for specimens B2 and B3. One possible explanation would be the presence of an initial flaw (or a larger initial flaw) on one side of the specimen in specimens B4-B6. This would cause secondary bending towards the pristine side of the specimen, causing a large reduction in the local mode I component of the SERR[1]. This would impede initiation and initial growth, which is thought to be mode I dominated [7]. Another explanation consistent with the results would be measurement error, possibly caused by delamination growth without disturbance of the paint layer applied to the edge of the specimen. If the delamination grows without cracking or deforming the paint layer this would cause the measured delamination length to be shorter than the actual delamination length. If the difference between measured and actual delamination length diverges the measured delamination growth rate will also be too low.

[1]The mode I reduction is not just due to reduction of the total SERR, the mode mix angle is also increased.

6.3 Relation Between Delamination Growth and SERR for series A and B

In order to use the test data gathered from the material coupons for the prediction of delamination growth, the delamination growth rate needs to be related to the SERR according to the Paris relation:

$$\frac{db}{dN} = C\,(G)^m \tag{6.1}$$

One aspect that must be decided is which expression to use for G. It is possible to use the total G, but it is also possible to only consider one of the modal components. Instead of using G_{max} (the SERR when S_{max} is applied) it is also possible to use $\Delta\sqrt{G}$, which is defined as [17]:

$$\Delta\sqrt{G} = \left(\sqrt{G_{max}} - \sqrt{G_{min}}\right)^2 \tag{6.2}$$

To determine the best option all possibilities were plotted and are shown in figures 6.8 through 6.13. These figures include the data from test series A and B, as well as data from earlier experiments conducted at both TU Delft and Airbus (unpublished).

The earlier tests at TU Delft relied on both direct visual measurements, as well as DIC to detect the delamination front. The tests conducted by Airbus measured the delamination growth rate by means of vacuum gauges. In this method a hole is drilled through one of the adherents and part-way in to the adhesive layer. A vacuum is applied to this hole. When the delamination reaches this point the hole will no longer have an airtight seal and thus the vacuum will be broken, which is detected by a pressure gauge.

The delamination growth rate for each delamination monitored during the test was determined from the slope of a linear curve fit through the measured points. For the series A specimens where there was a clear drop-off visible in the delamination growth, the growth rate was determined from the linear portion of the graph. The corresponding SERR was calculated using the numerical models described in chapter 4; taking the average of the SERR for a delamination length of 5, 10 and 15 mm and assuming all delaminations present on a specimen had an equal length.

The graphs clearly show that the best correlation between SERR and delamination growth rate is achieved by considering only the mode II component. Considering the total SERR [2], gives a reasonable correlation and considering only mode I SERR gives a poor correlation. This confirms the results of Alderliesten [20] that delamination growth is governed by the mode II component. The difference in correlation between using $G_{II,max}$ or $\Delta\sqrt{G_{II}}$ is small. This was expected, as all tests were performed for the same R-ratio. Additionally however it should be noted that the use of $\Delta\sqrt{G}$ eliminates the effect of thermal residual stresses [17]. If G_{max} is used this effect would not be eliminated. Thus the small difference in correlation between delamination growth rate and either $\Delta\sqrt{G}$ or G_{max} suggests the effect of thermal residual stresses on the delamination growth rate was small for these configurations.

The effect of test temperature itself is clearly visible in the graphs. The delamination growth rate at -30℃is roughly an order of magnitude lower than at room temperature.

[2] Of which mode II is the largest component, as shown by the analysis in section 5.3

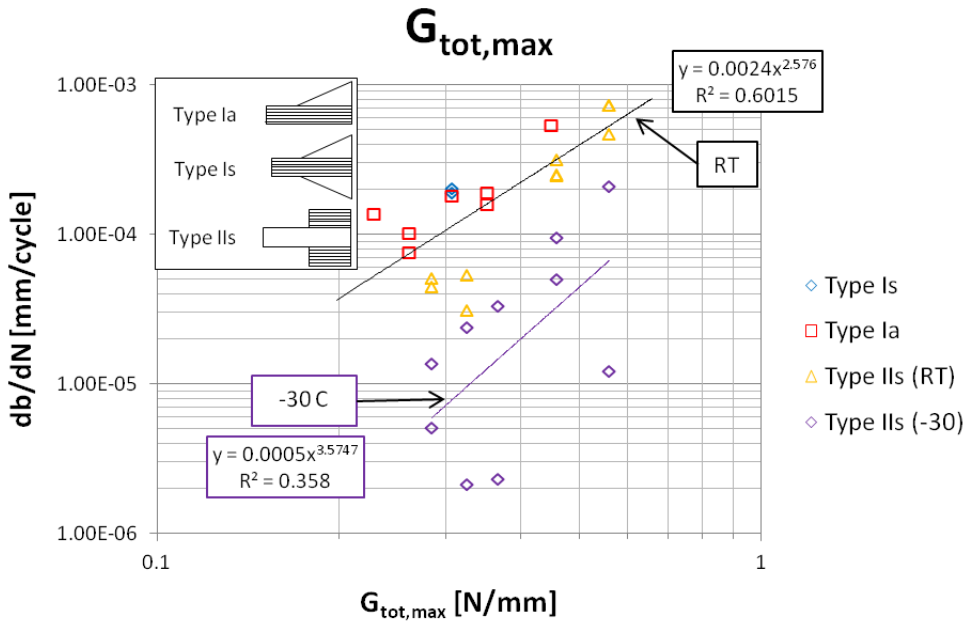

Figure 6.8: Delamination growth rate plotted as a function of maximum total SERR. Power-law curve fits are shown both for the specimens tested at room temperature and for the specimens tested at -30°C.

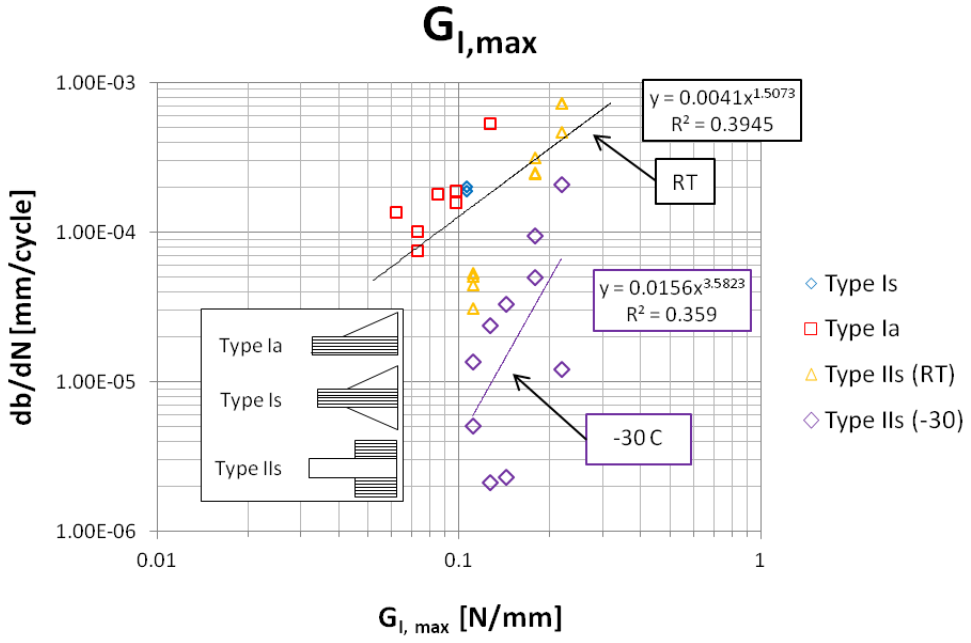

Figure 6.9: Delamination growth rate plotted as a function of maximum mode I SERR. Power-law curve fits are shown both for the specimens tested at room temperature and for the specimens tested at -30°C.

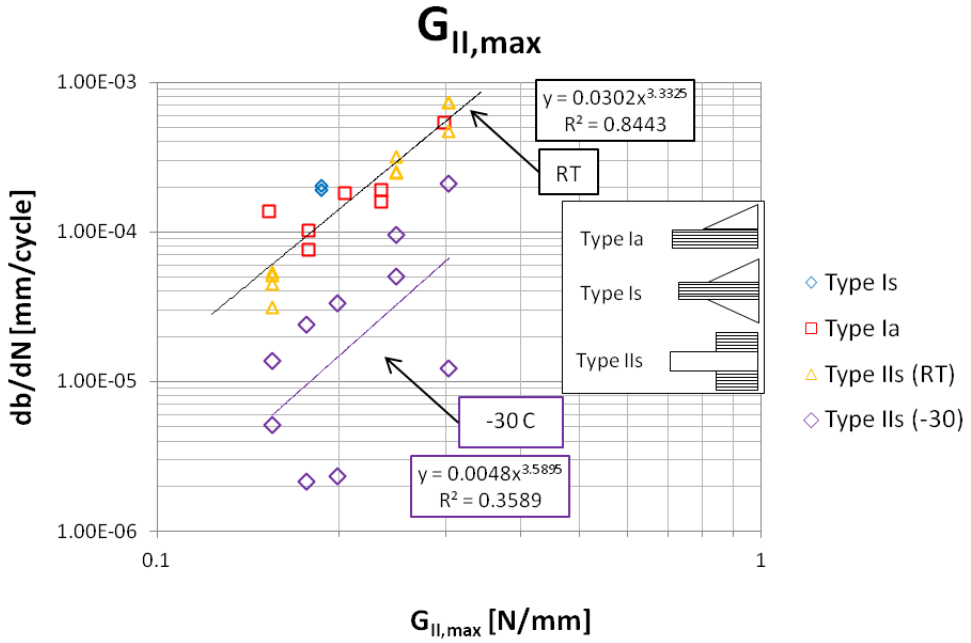

Figure 6.10: Delamination growth rate plotted as a function of maximum mode II SERR. Power-law curve fits are shown both for the specimens tested at room temperature and for the specimens tested at -30°C.

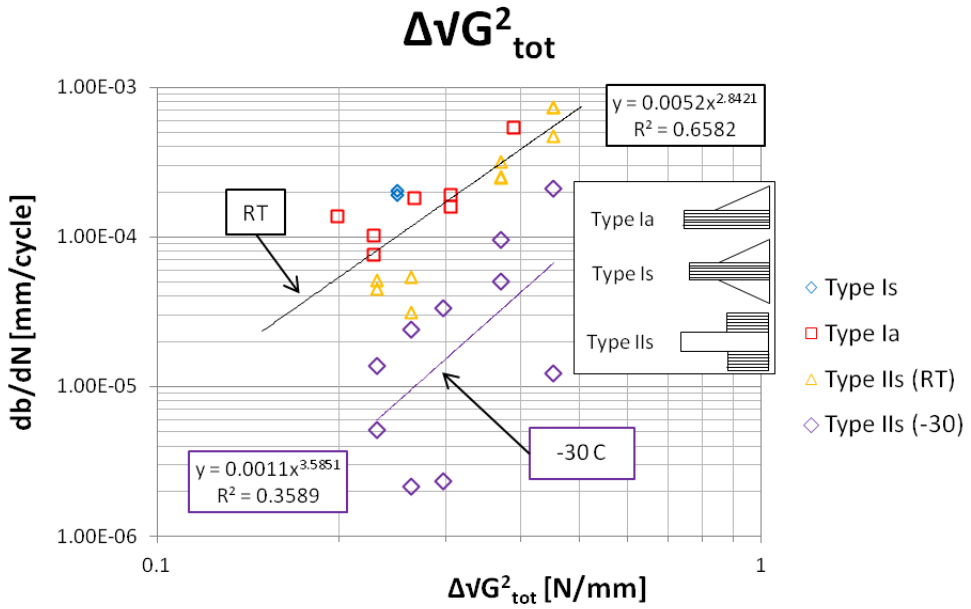

Figure 6.11: Delamination growth rate plotted as a function of total SERR range. Power-law curve fits are shown both for the specimens tested at room temperature and for the specimens tested at -30°C.

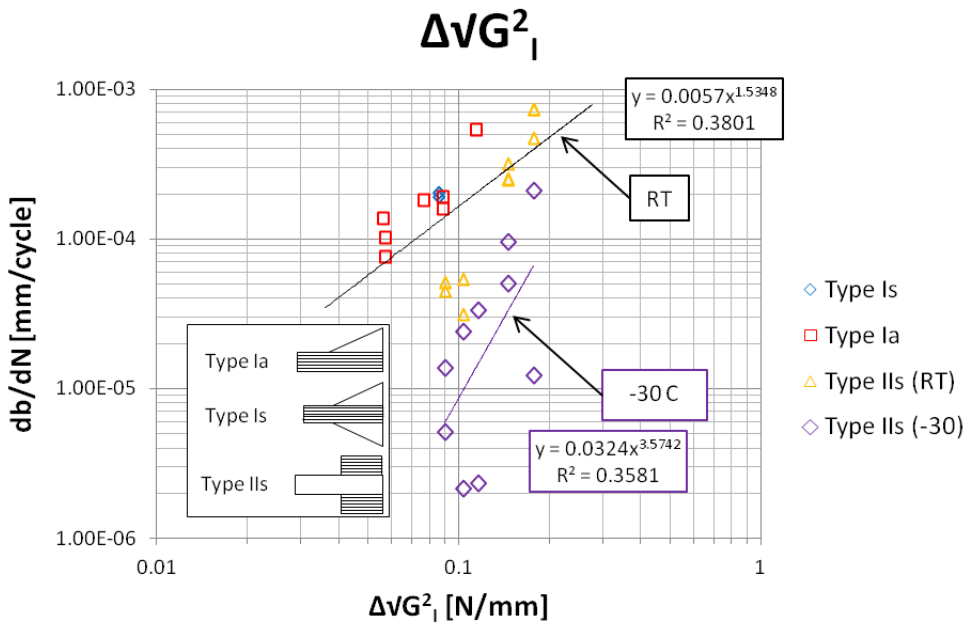

Figure 6.12: Delamination growth rate plotted as a function of mode I SERR range. Power-law curve fits are shown both for the specimens tested at room temperature and for the specimens tested at -30°C.

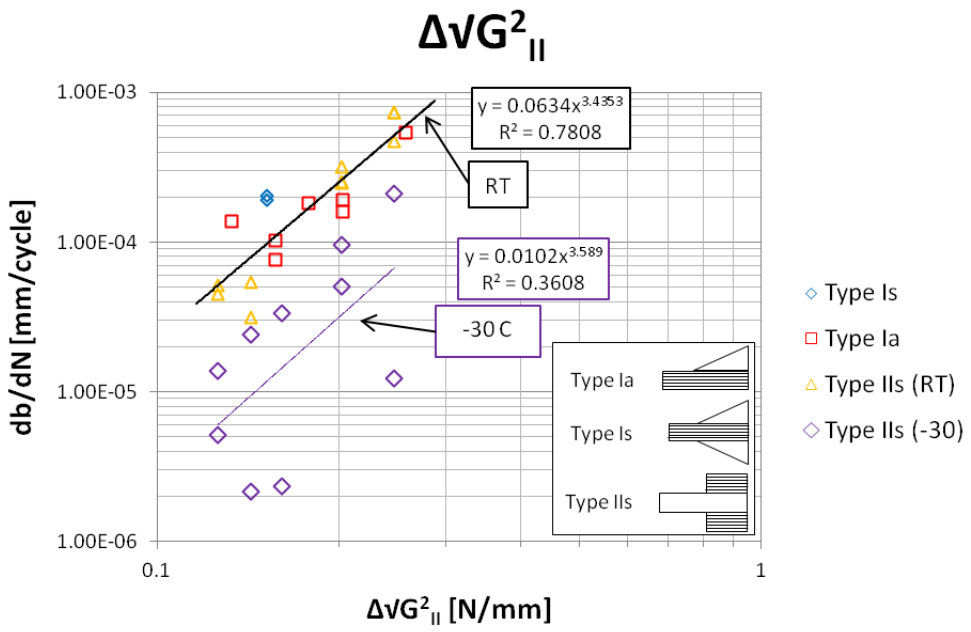

Figure 6.13: Delamination growth rate plotted as a function of mode II SERR range. Power-law curve fits are shown both for the specimens tested at room temperature and for the specimens tested at -30°C.

This is thought to be caused by the change in material properties of the adhesive, which becomes stronger and more brittle at lower temperatures [38]. This result is in contrast to the results of Rans et al. [15], who found an increased delamination growth rate at low temperature (-40 ℃in that case) in FMLs. Apart from the difference in adhesive thickness between the specimens investigated in this case and the FML specimens investigated by Rans et al, the FMLs used a different adhesive than was used for the material coupons. Both of these factors may explain the difference in delamination growth rate behaviour.

There is a large amount of scatter visible for the series B test data. This is caused by the assumption that the delaminations in the specimens all have equal length. From the measurement data presented in figure 6.4 it is clear that this is not the case in reality. In fact there are (in some cases quite large) differences in delamination length. The analysis presented in section 5.4 suggests that large differences in local SERR at each delamination tip should be expected in these cases. Thus it was attempted to correct for this asymmetric growth by considering the local SERR. Again the SERR was averaged over a number of delamination sizes, using different lengths for the different delaminations. The choice of lengths was based on the measurement results. The results are shown in figure 6.14. Accounting for the asymmetric growth of the delaminations clearly eliminates a large portion of the scatter, showing that this effect should not be ignored in the case of a symmetrical bonded joint. Averaging the delamination growth and local SERR over a smaller range of delamination lengths would most likely further reduce the scatter.

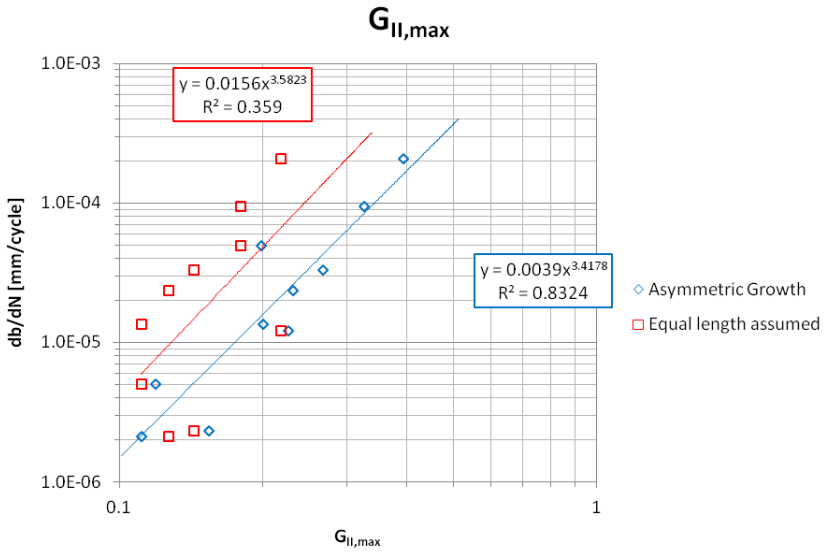

Figure 6.14: Comparison of the delamination growth rate as a function of maximum mode II SERR for the series B specimens, both with and without taking into account asymmetric growth.

6.4 Series C

Specimens C1, C2, and C3 were tested to failure. Due to time constraints testing of specimen C4 was stopped after 170 kcycles, at which point sufficient delamination growth

data was assumed to have been collected.

Specimens C1 and C2, which both contained an artificial delamination initiation, failed due to fatigue fracture of the substrate. The fatigue crack initiated in the vicinity of the delamination front. Specimen C3, which did not contain an artificial delamination, also failed due to fatigue fracture of the substrate. However in this case the fatigue crack initiated at the corner of the central cut-out in the substrate. Figure 6.15 shows schematically the locations of the fatigue crack initiations. Given these initiation locations it would appear that the delamination front acts as a sufficiently strong stress raiser to initiate a fatigue crack in the substrate.

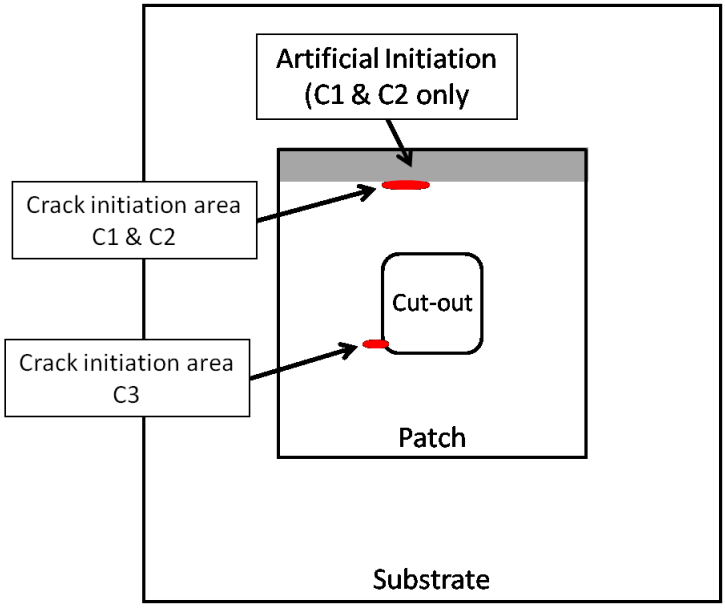

Figure 6.15: Schematic overview of the fatigue crack initiation locations. All fatigue cracks initiated in the substrate.

6.4.1 Specimen C1

Specimen C1 was monitored using 3D DIC. A reference image was taken before the start of testing, which was compared to new images taken at regular intervals during testing. The comparison images were taken with the specimen loaded with the maximum fatigue load. Figure 6.16 shows a comparison between the strain field as measured by DIC and that predicted by the FEA. Qualitatively the strain fields match, with corresponding areas of high and low stress. The FEA predicts a much smoother strain field than was measured. This is thought to be caused by noise in the DIC measurement.

The delamination front is clearly visible in the image, in the form of the steep strain gradient. The location of the strain gradient was measured at a number of points distributed over the width of the specimen in each of the images, producing figure 6.17. Since the objective of the test was to measure the delamination growth rate, the y-coordinate as given by the DIC software was not converted to a delamination length.

There was a large amount of scatter in the length measurements, making the delamination

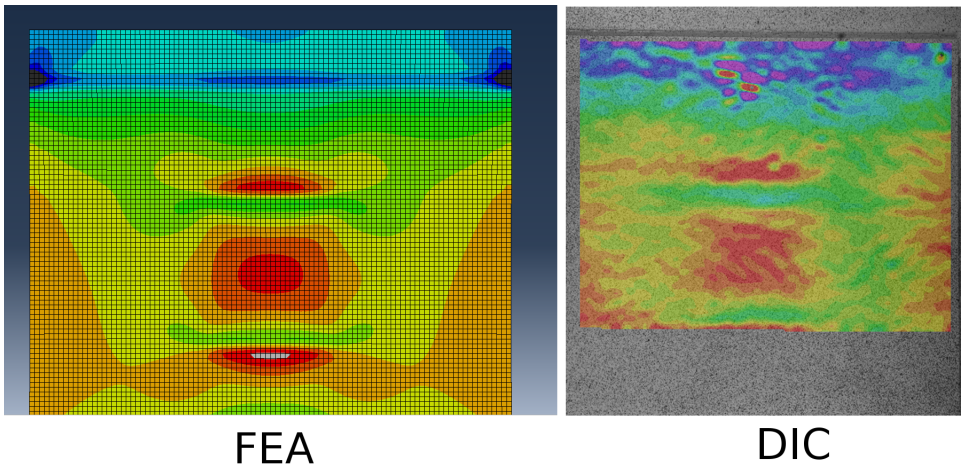

Figure 6.16: Comparison between the strain field predicted by FEA (left) and the strain field as measured by DIC (right). Black/blue/purple indicates areas of lowest strain, red/grey indicates areas of highest strain. The two high strain areas visible in the delaminated (low strain) area in the DIC image are thought to be measurement errors caused by damage of the CCD-chip in the camera used. The FEA image shows true strain, whereas the DIC image shows engineering strain.

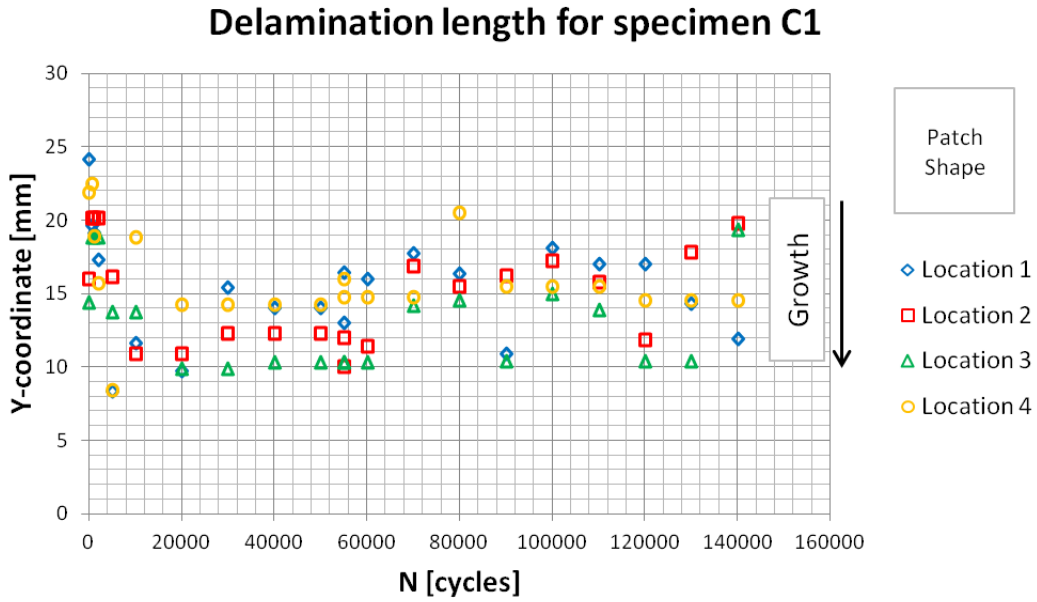

Figure 6.17: Delamination length measurements for specimen C1. The vertical axis shows the y-coordinate of the delamination front, measured from the bottom of the DIC image. A decrease of the y-coordinate implies delamination growth, as indicated.

growth measurement rather unreliable. Averaging the growth rates for each of the four locations measured gives an average growth rate of 9.48 E-06 mm/cycle, with a standard

deviation of 8.83 E-06 mm/cycle.

An important source of the scatter is the noise in the DIC measurements, which can be seen in figure 6.18. Figure 6.18 a was taken after 55 kcycles at the end of a day of testing. Figure 6.18 b was taken at the start of the next day, before testing was continued. Thus no changes would be expected and yet the two measured strain fields are significantly different. Figure 6.17 shows the resultant difference in measured delamination length at $N = 55$ kcycles. This demonstrates the amount of noise in the DIC measurements. For accurate delamination measurements the technique will need to be refined.

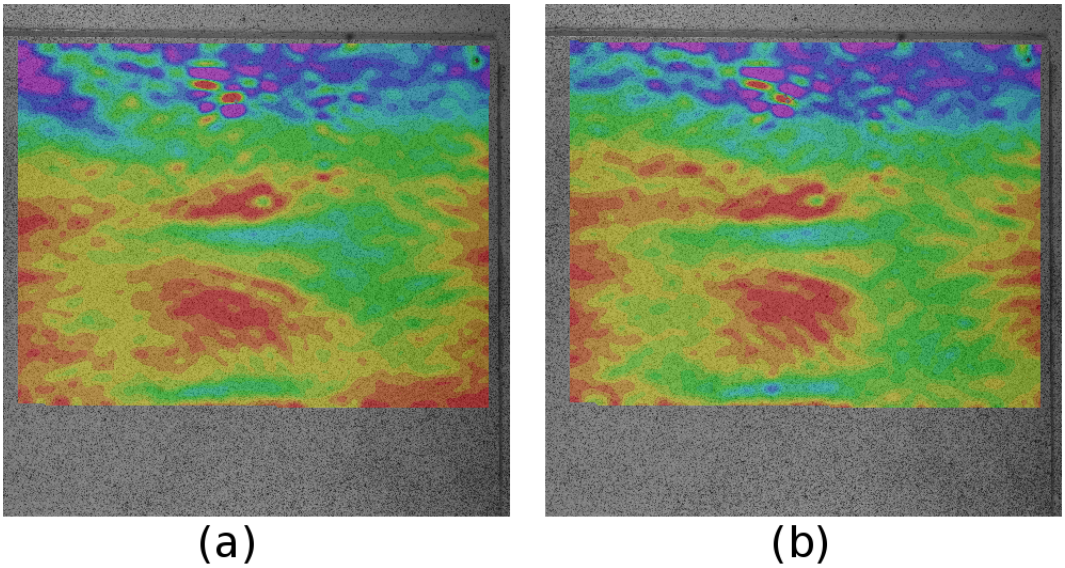

Figure 6.18: Comparison between two DIC measured strain fields after 55 kcycles. Image (a) was taken at the end of one test day. Image (b) was taken at the start of the next day. As no fatigue loading occurred in the meantime and the specimen was kept at room temperature in lab air, the two measured strain fields should be the same. However due to the noise in the DIC system they are not.

6.4.2 Specimen C2

Specimen C2 was monitored using 2D DIC. As a result the numerical strain values measured are unreliable, since they fail to account for the effect of secondary bending, which will occur out of the plane of the image. A representative DIC image is shown in figure 6.19. Although the numerical value of the calculated strain is incorrect (maximum strain is measured in the delaminated area) there is a clear strain gradient visible, which indicates the presence of the delamination front.

Again the delamination length was measured at several points distributed over the width of the specimen, as shown by the black circles in figure 6.19. The resultant delamination length measurements are shown in figure 6.20.

As was done for specimen C1 a set of images was taken both at the end of one test day and at the start of the next, in this case at 30 kcycles, giving an impression of the amount of noise in the measurements. Again a large amount of scatter is visible. There

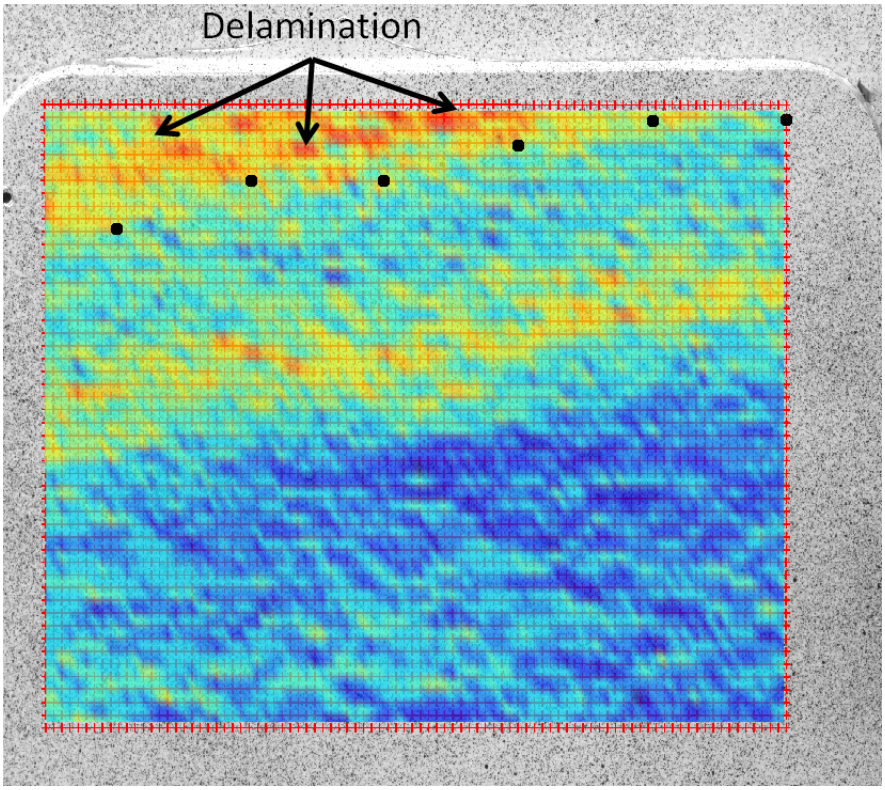

Figure 6.19: DIC image for specimen C2 at 20 kcycles and maximum fatigue load. The calculated strain field is superimposed, showing the delaminated area. The points used for the delamination measurements are marked by the black circles.

also appears to be a sharp drop in the delamination length after 40 kcycles. Since it is highly unlikely that the adhesive bond suddenly developed self-healing properties, it is thought that the apparent drop (or the prior steep rise at 30 kcycles) is an artifact of measurement error. Another possibility is that the initiation of the fatigue crack that later caused failure of the substrate somehow modified the stress field, and thus the strain field, making it appear as if the delamination front had retreated. Although the presence of a fatigue crack should not change the strain in the delaminated portion of the patch the fatigue crack might change the secondary bending of the entire specimen. Using only 2D DIC the out of plane displacement as a result of a change in the secondary bending cannot be separated out from a change in the strain field itself.

6.4.3 Specimen C3

Specimen C3 did not contain an artificial delamination initiation. There was some natural delamination initiation at the corners of the patch, as can be seen in figure 6.21. Little to no delamination growth occurred before the specimen failed due to fatigue cracking of the substrate. As was mentioned above, and was highlighted by figure 6.15 it is interesting to note that in this case the fatigue crack initiated at the edge of the central cut-out, rather than at the delamination front.

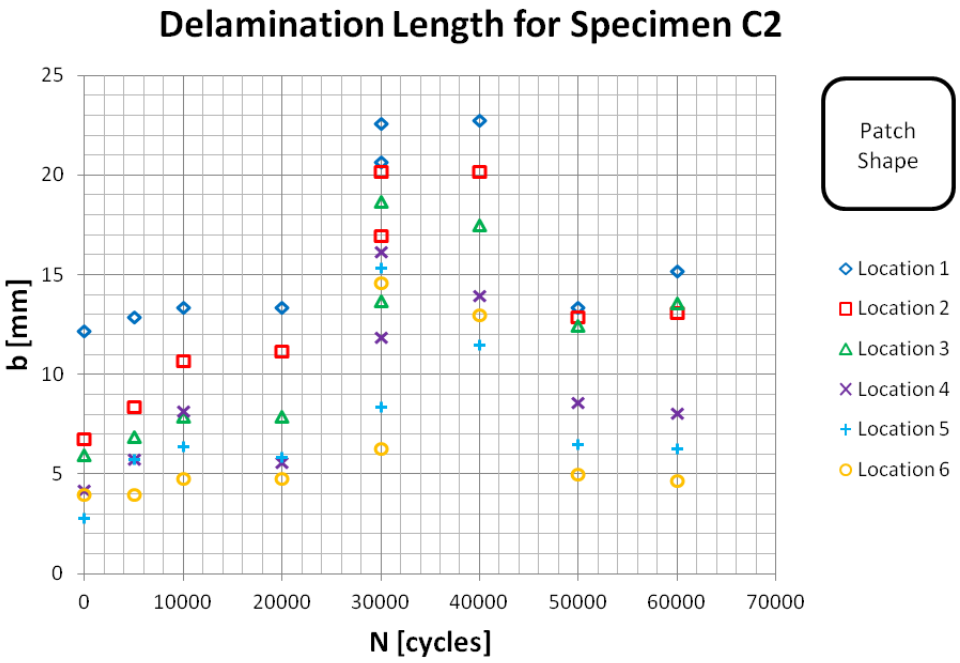

Figure 6.20: Delamination length measurements for specimen C2.

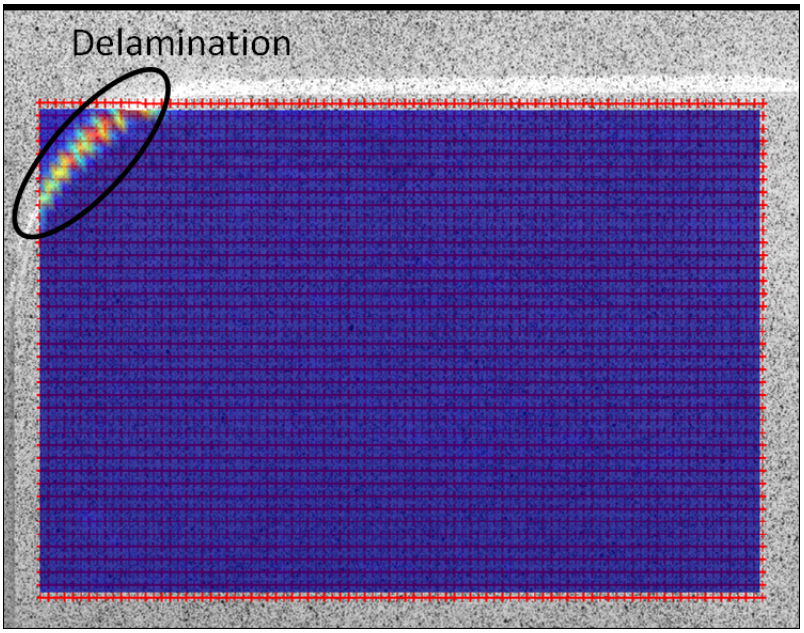

Figure 6.21: DIC image for specimen C3 at 170 kcycles and maximum fatigue load. The specimen failed due to fatigue cracking of the substrate shortly afterwards.

6.4.4 Specimen C4

Specimen C4 did contain an artificial initiation, as was clearly visible in the DIC images. An example is shown in figure 6.22, which was the last measurement taken during the test.

No delamination growth was observed. In addition it is remarkable that the delamination length in figure 6.22 appears to be only 1 mm. This is remarkable because adhesive tape was applied to the substrate, to prevent bonding of the adhesive, over an area that extended 5 mm from the patch edge. Either there was an error during manufacturing, or the adhesive tape did not initiate a delamination as anticipated.

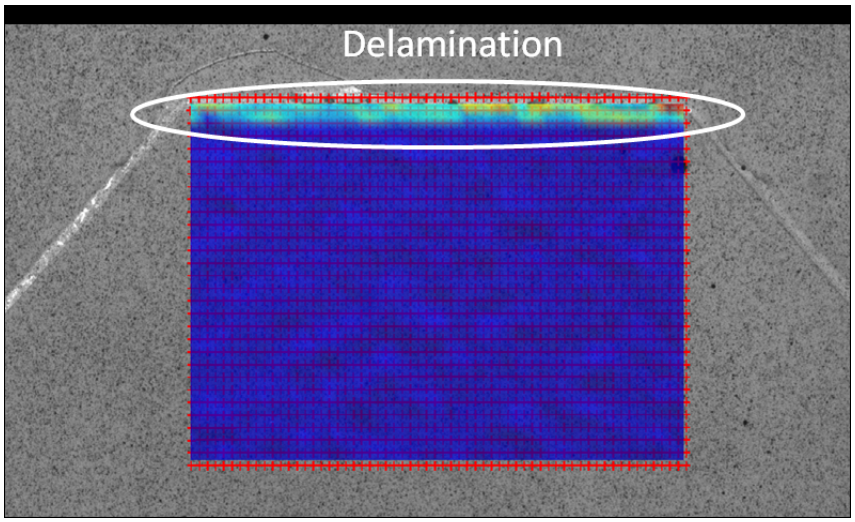

Figure 6.22: DIC image for specimen C4 at 170 kcycles and maximum fatigue load.

6.5 Relation Between Delamination Growth and SERR for Series C

As was done for series A and B, the measured delamination growth rate for specimen C1 and C2 was plotted against the SERR. Based on the measured lengths the SERR value used was the average of the values calculated for a delamination length of 5, 10 and 15 mm.

The resulting graphs are shown in figure 6.23 for the total SERR, figure 6.24 for the mode I SERR and in figure 6.25 for the mode II SERR. As the delamination growth rate was measured at a number of locations spread over the patch width, the delamination growth rate was plotted for each of these locations separately. For one location on specimen C1 the delamination growth rate was not plotted, as a negative growth rate was measured here, which seems highly unlikely to be correct.

The growth measurements match best with the trend line determined for the material coupons when only the mode II SERR component is considered. This mirrors what was noticed for the material coupons themselves, i.e. that the correlation between delamination growth rate and SERR was greatest for the mode II component.

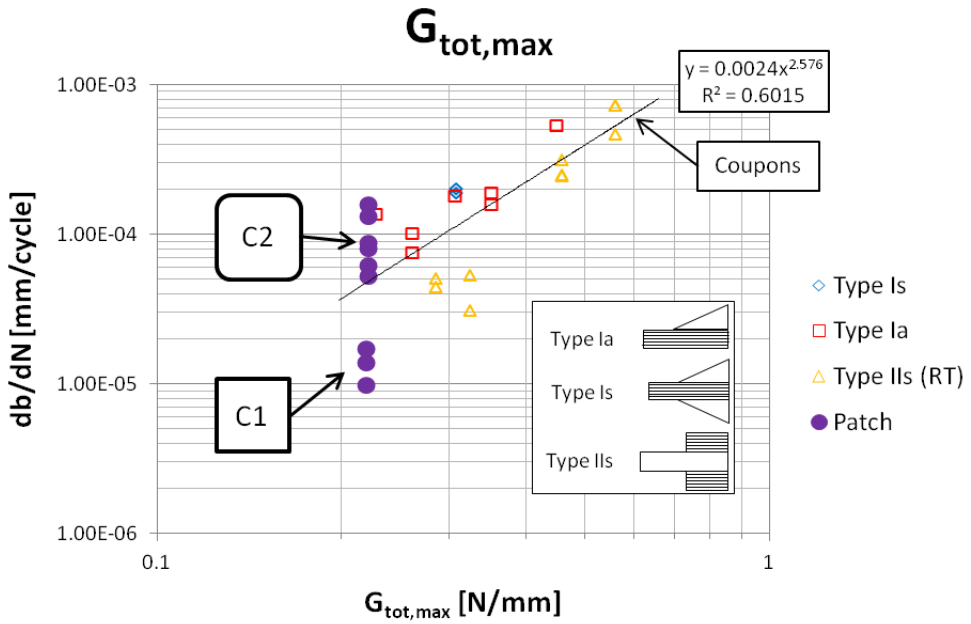

Figure 6.23: Delamination growth rate plotted as a function of total SERR. The power-law curve fit shown is based only on the material coupon data. Delamination growth rate of specimens C1 and C2 is shown for each measurement location separately.

The measured growth rate for specimen C2 agrees fairly well with what would be predicted based on the trend line for the material coupons. For specimen C1 the agreement is not very good however. Even in the best case (mode II SERR component only) the measured growth rate is a factor 2 to 8 lower than what would be predicted. In the end though the underlying delamination length measurements, and thus the growth rate measurements that are based on them, are to unreliable to draw any firm conclusions from these graphs.

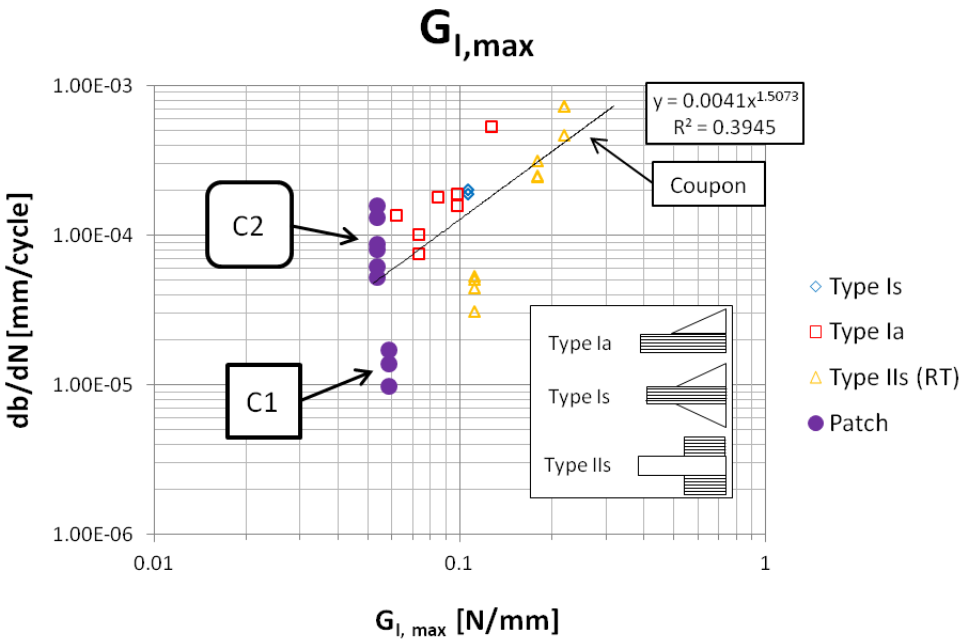

Figure 6.24: Delamination growth rate plotted as a function of mode I SERR. The power-law curve fit shown is based only on the material coupon data. Delamination growth rate of specimens C1 and C2 is shown for each measurement location separately.

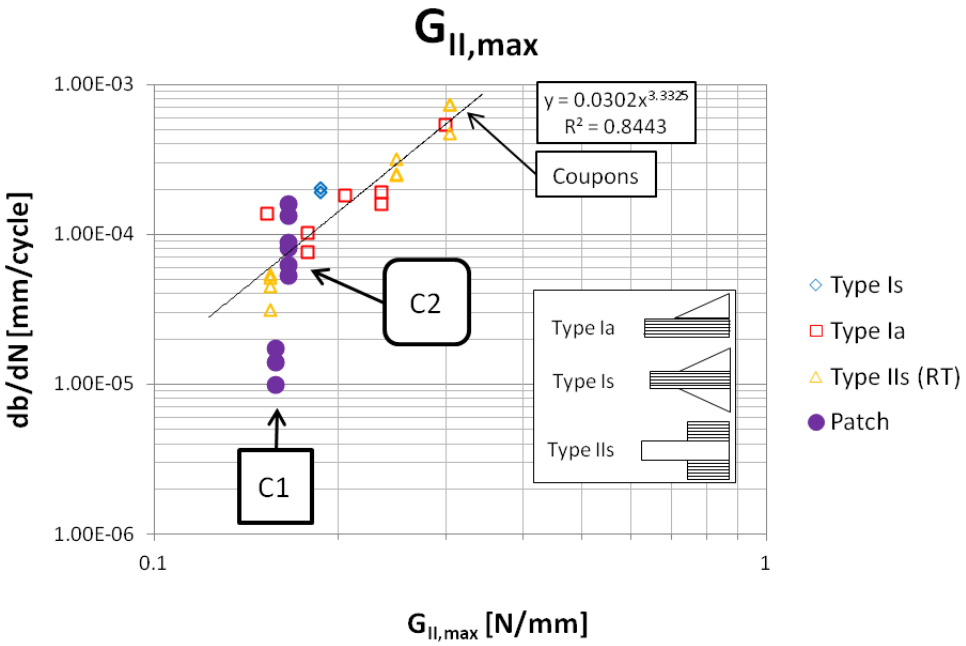

Figure 6.25: Delamination growth rate plotted as a function of mode II SERR. The power-law curve fit shown is based only on the material coupon data. Delamination growth rate of specimens C1 and C2 is shown for each measurement location separately.

Chapter 7

Prediction of the Delamination Growth

The results of the numerical analysis presented in chapter 5 and the test results presented in chapter 6 can be combined to generate a prediction for the delamination growth. This chapter starts with a description of the model used and then continues with a comparison between the model predictions and the test results.

7.1 Description of the Model Used

The model is based on the following two equations:

$$G = f(b) \tag{7.1}$$

$$\frac{db}{dN} = C(G)^m \tag{7.2}$$

Where G can be any expression of the SERR as appropriate. Based on the results presented in section 6.3, $G = G_{II,max}$ or $G = \Delta\sqrt{G_{II}}$ are used, unless otherwise specified.

The first of these equations describes the dependance of the SERR on the delamination size and follows from the FEA results employing the VCCT. The function, which depends on the applied stress and specimen configuration, was found by calculating the SERR at a number of fixed and pre-defined delamination lengths. A fourth-order polynomial trend line was then fit through those points. The second equation is the Paris relation between delamination growth rate and SERR. The required parameters C and m were determined by a power law curve fit through the points in the $\frac{db}{dN}$ vs G graphs constructed for the material coupon specimens (figures 6.10 and 6.13).

These two equations were combined in an iterative numerical integration, resulting in a prediction of the delamination length as a function of cycle count. Figure 7.1 shows schematically the algorithm used to do this. To set up the calculation a cycle increment

ΔN and maximum cycle count N_{max} must be chosen. As mentioned in section 2.5 the developed method does not incorporate delamination initiation. Thus an initial delamination length b_0 must also be chosen. The algorithm was implemented in a Matlab code (included in appendix B), which gives as output both a vector of delamination lengths at each cycle increment and a graph of b versus N.

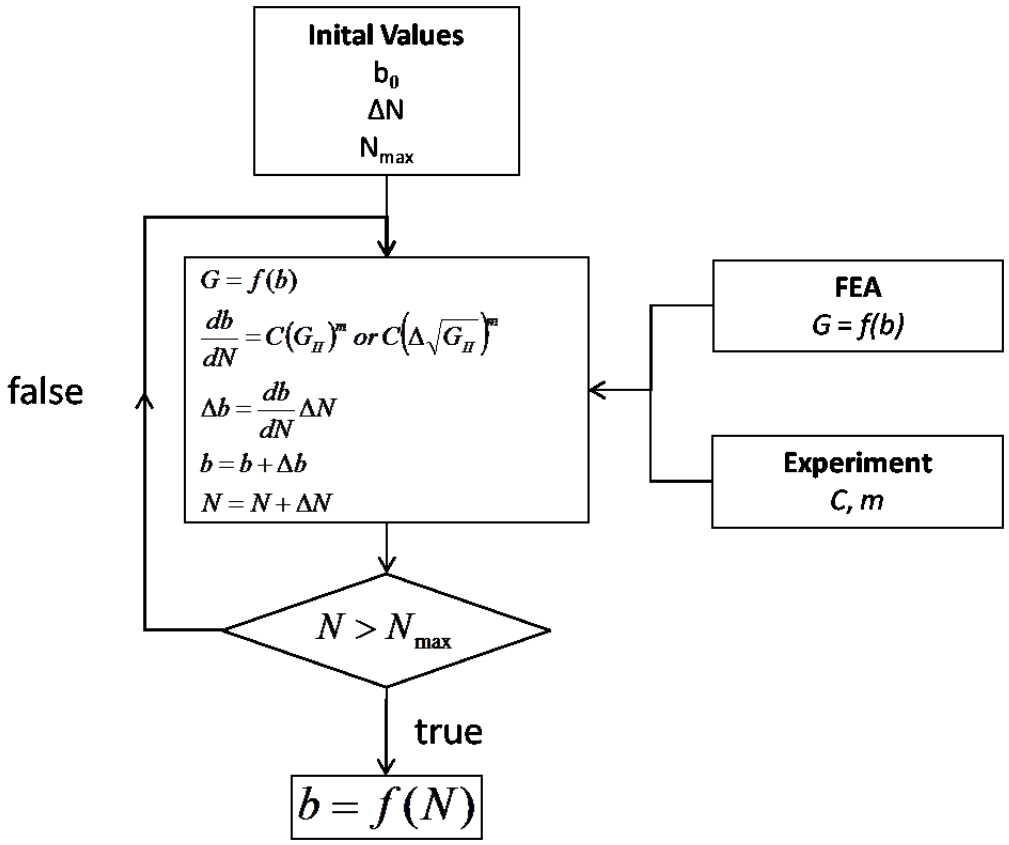

Figure 7.1: Flowchart depicting the numerical algorithm used to predict delamination length as a function of cycle count.

7.2 Comparison Between Predictions and Material Coupon Results

The key parameters of the proposed delamination prediction model, C and m, are based on a curve fit through the measurement data collected from the material coupons. As such any prediction produced for the material coupons is tautological and can not be used to validate the model. However these predictions can still provide some insight into the behaviour and limitations of the model.

Figures 7.2 through 7.4 show predictions for the delamination growth in specimen A1 based on, respectively, $G_{tot,max}$, $G_{II,max}$ and $\Delta\sqrt{G_{II}}$. The predictions are compared with the measurement results. The measurement results have been translated along the N-axis direction in order to match the initial delamination length chosen for the prediction

model. The initial delamination length was chosen such that the delamination had grown beyond the initiation phase.

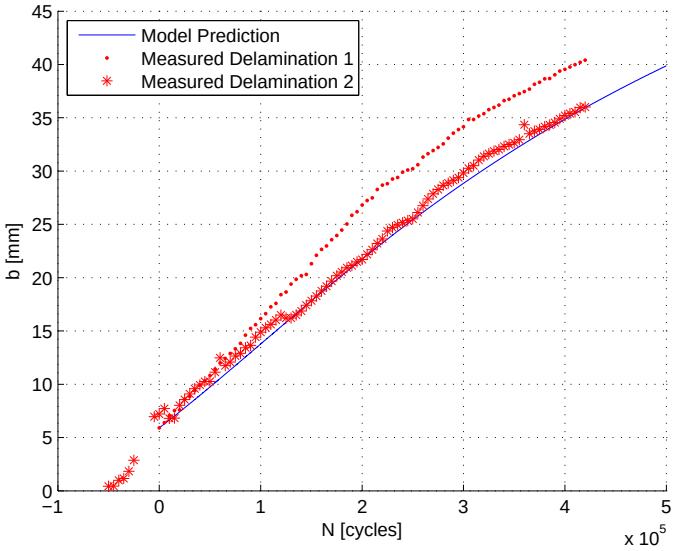

Figure 7.2: Delamination growth prediction for specimen A1 based on $G_{tot,max}$.

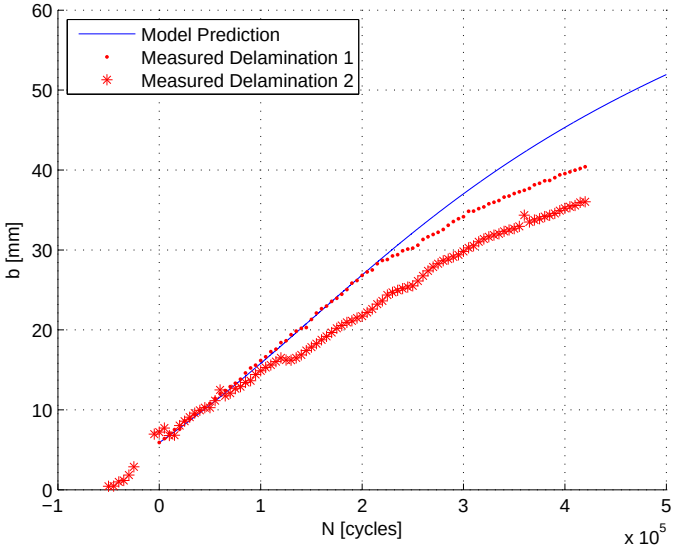

Figure 7.3: Delamination growth prediction for specimen A1 based on $G_{II,max}$.

As C and m were partially based upon measurement data for specimen A1 these predictions are rather tautological, as mentioned above. However it should be noted that C and m were determined using only the linear portion of the delamination growth assuming a constant (average) value for G. Nevertheless the curvature of the predicted delamination length curve follows that of the measured delamination length curve. This is significant because although the *slope* of the predicted curve follows from the measurement results,

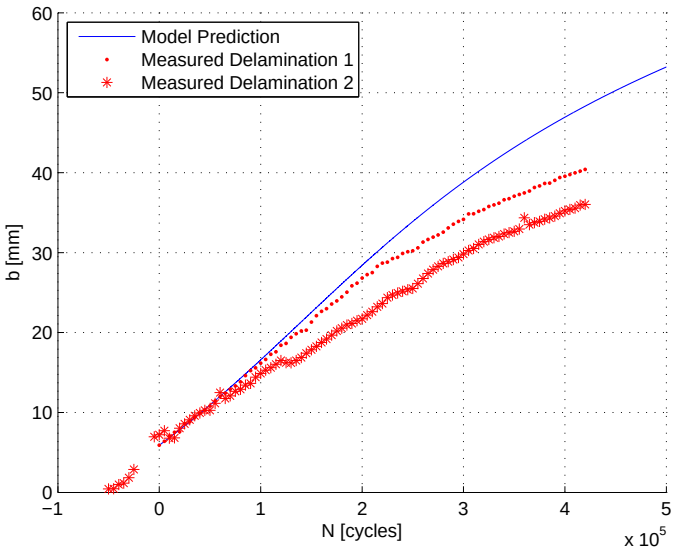

Figure 7.4: Delamination growth prediction for specimen A1 based on $\Delta\sqrt{G_{II}}$.

the *curvature* follows only from the FEM analysis. This supports the idea that the G vs b relationship determined by the numerical analysis is correct and can be used to describe the delamination growth behaviour.

7.3 Comparison Between Predictions and Patch Repair Results

Using the developed model a delamination prediction was also generated for specimens C1 and C2. The predicted delamination length is compared to the measurement results in figure 7.5 for specimen C1 and figure 7.6 for specimen C2. In both cases the prediction was based on the mode II SERR component. These graphs have been included for the sake of completeness, but as was discussed in sections 6.4 and 6.5, the delamination length measurements are considered to be too unreliable to draw any firm conclusions from these graphs.

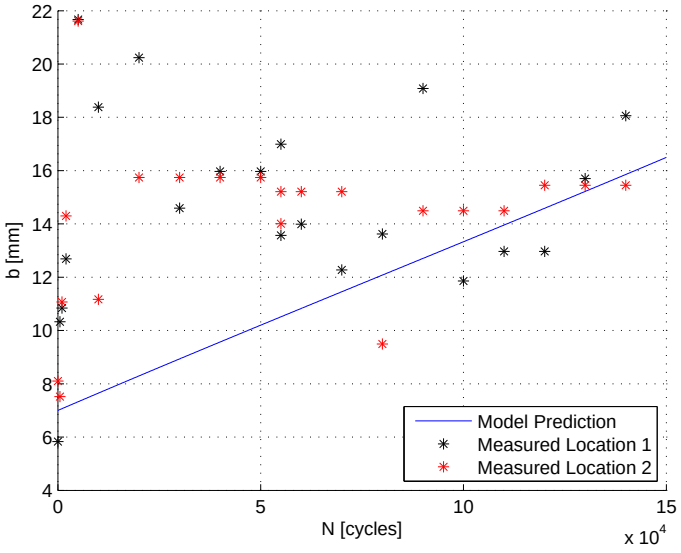

Figure 7.5: Delamination growth prediction for specimen C1 based on $G_{II,max}$.

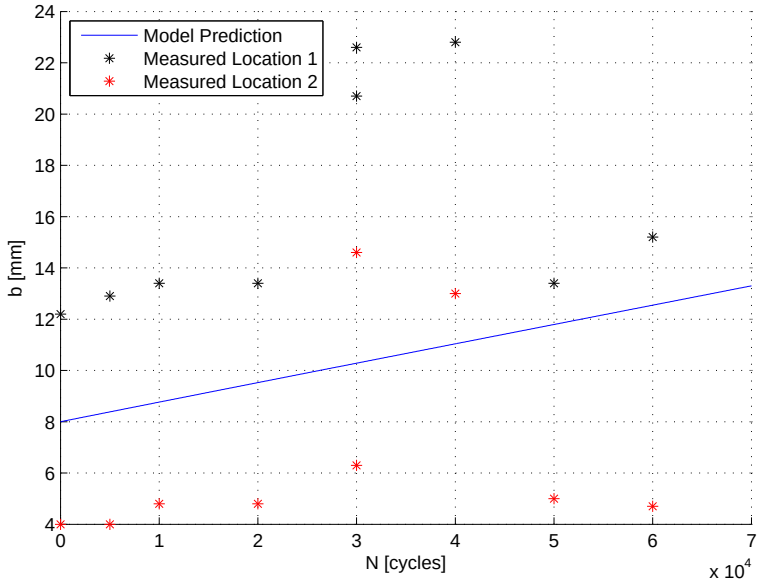

Figure 7.6: Delamination growth prediction for specimen C2 based on $G_{II,max}$.

Chapter 8

Conclusions and Recommendations

This chapter presents the conclusions of the thesis research. It also provides recommendations for the use of the developed model in design practice and for further research to improve the model.

8.1 Conclusions

This section presents the conclusions of the research.

Delamination growth represented as a function of SERR The most important conclusion of this research is that the delamination growth rate in an adhesively bonded repair can be described by a power law function of the strain energy release rate. The delamination growth rate is most strongly correlated to the mode II component of the SERR. Mathematically this can be stated as:

$$\frac{db}{dN} = C\left(G_{II,max}\right)^m \tag{8.1}$$

One can also use the expression:

$$\frac{db}{dN} = C\left(\Delta G_{II}\right)^m \tag{8.2}$$

However in the present research this did not significantly affect the correlation with the delamination growth rate, as discussed in section 6.3. It is expected that in cases where the R-ratio is not constant, or thermal residual stresses have a significant effect, equation 8.2 will be more accurate than equation 8.1. However this can not be confirmed using the results of this research.

Significance of the Paris relation parameters In equations 8.1 and 8.2, the SERR is a similarity parameter that depends only on the structural configuration. C and m are material parameters. Thus if C and m are determined by performing experiments on a certain structural configuration, they can be used to predict the behaviour of a different structural configuration made using the same materials. One important caveat however is that the environmental conditions must remain the same.

As shown by the results of the series B specimen tests presented in section 6.3, C and m depend on test temperature. By analogy to the Paris relation in fatigue crack growth it is expected that these parameters will also be material dependant, but that can not be confirmed on the basis of this research. Given that C and m essentially are a measure for the amount of energy needed to grow the delamination, it is perhaps better to consider them 'interface parameters' rather than material parameters. This recognises that any factor that may influence the strength of the interface, whether environmental or related to the materials, may change the value of these parameters.

Effect of temperature The results of the series B specimen tests show that reduced temperature retards delamination growth. The most likely cause for this retardation is the change in material properties of the adhesive as a result of the lower temperature.

Calculation of the SERR To create a full delamination growth prediction model it is necessary to know the behaviour of the SERR as a function of delamination length. This relationship can be found by employing the virtual crack closure technique in a finite element analysis, by pre-defining suitable delamination lengths in the model and then interpolating between the results. As an alternative to the VCCT analytical methods may be used to calculate the SERR. However as was shown in section 5.1 care must be taken to ensure that the equations are suitable to the configuration being studied and that the underlying assumptions (often, the lack of secondary bending) are not violated.

Delamination prediction model Combining the G versus b behaviour found either numerically or through an analytical method with either equation 8.1 or 8.2 the delamination size as a function of number of fatigue cycles can be predicted by a numerical integration. The accuracy of the prediction will depend on the size of the scatter band around the $\frac{db}{dN}$ vs G trend line for the material under investigation. It should be emphasised that this model is a damage growth model only. It assumes an initial flaw is present and does not correctly account for any initiation or initial growth effects.

Validation The patch repair specimens were intended to validate the prediction method described above. However the inaccuracy of the delamination length measurements, discussed in section 6.4, prevent the drawing of any firm conclusions. However some confirmation of the correctness of the approach may be seen in the results of the material coupons as presented in section 6.3. The data presented here combines results for three different patch configurations as well as three different measurement techniques. Nonetheless the data points fall along a single trend line, showing at the very least that G is indeed a configuration independent similarity parameter. By itself however it is not sufficient to

describe the delamination growth behaviour, as temperature (and thus most likely also other environmental effects) will have a large influence on delamination growth as well.

Effect of asymmetric delamination growth As discussed in section 5.4, asymmetric delamination growth can cause the local value of the SERR at a delamination front to be significantly different to what would be found if all delaminations are assumed to grow equally. Especially in a symmetrical patch configuration where delaminations on opposite sides of the substrate thickness do not grow equally, the difference in SERR can be very large. Once a difference in delamination length is present, the difference in local SERR values will cause the delamination lengths to diverge, increasing the difference. A failure to account for this effect can cause a significant under prediction of the delamination growth rate or the false appearance of scatter in test data.

Criticality of the delamination mode Apart from the conclusions on the delamination growth behaviour the experiments also show that, in an appropriately designed adhesive bond, disbonding due to delamination of the adhesive interface is not the critical damage mode. In all specimens that failed, failure occurred due to fatigue crack growth in the metal adherents. In all cases the delamination had reached at most 30% of the bond length when failure of the adherent occurred. The location of the fatigue crack initiations on the patch repair specimens suggest that the delamination front may produce a stress concentration that is significant enough to initiate fatigue cracking. As such, even if delamination is not the critical damage mode, it may play an important role in accelerating a different damage mode.

8.2 Recommendations

This section will offer both recommendations on the use of the results of this research in design practice as well as recommendations for further research.

8.2.1 Recommendations for Design Practice

This research has shown that delamination growth rate can be described as a power-law function of the mode II SERR component. Thus designing for minimum delamination growth (or equivalently maximum delamination life) is equivalent to designing for minimum mode II SERR. With an appropriate design the designer can also ensure that delamination of the patch will not be the critical failure mode.

If merely the optimum shape with regards to delamination growth is required, computationally cheap numerical methods or analytical methods can be used. As long as the point in the design space that will produce the minimum SERR is correctly identified, the actual value SERR calculated is not important. Although the actual growth rate can not be predicted accurately in this way, it can be confirmed which design will produce the minimum SERR. Once the design for minimum SERR has been found, more computationally expensive models can be used to find the actual SERR value. This can then be used to provide an accurate prediction of the delamination growth rate.

Although the analytical methods for the calculation of the SERR were not used in this research, due to the presence of secondary bending in the specimens being tested, they may be of more use in the actual design of aircraft structures. Many bonded repairs will be applied to curved panels constrained by supporting structures. Thus it is likely that secondary bending will not be an important issue. In those cases the analytical methods may offer a computationally cheap way of calculating the SERR. The designer should ensure that the method used is appropriate to the specific patch configuration under investigation however.

The designer should take care to study any possible interaction effects. From the results of the patch repair specimens it appears that delamination in the adhesive interface can initiate fatigue cracking in the adherents. Thus it is imperative that this interaction be studied.

In addition to the interaction between delamination and fatigue crack initiation and growth, the designer should also study the possible interaction effects of multiple delaminations occurring in the bonded repair. Especially in the case of delaminations with different lengths on opposite sides of a plate (e.g. in a symmetrical bond) these interaction effects can cause large changes in the local SERR.

8.2.2 Recommendations for Further Research

The method developed in this research is a delamination growth model and thus assumes an initial flaw is present, as is common practice in damage tolerance analyses. However if no initial flaw is present in reality the delamination initiation phase may be significant, as can be seen in the results for the series A specimens. For those specimens the initiation phase represented about 20% of the total test life. In patch repair specimens C3 and C4 the delamination never progressed beyond the initiation phase before the substrate failed. For a full understanding of the damage tolerance of a bonded repair as a whole the delamination initiation behaviour also needs to be understood.

As it appears delaminations can initiate fatigue cracking in the adherents, a greater understanding of the interactions between bond-line damage and adherent damage is needed.

Regarding the model as developed in this research, it needs to be extended in many ways to be usable in actual aircraft design. First of all a more thorough validation of the model should be performed, as lack of accuracy in the delamination length measurements for the patch repair specimens prevented a proper validation of the model in this research.

Second, in this research the only loading investigated was uni-axial, constant amplitude and with only one R-ratio. In reality aircraft structures are (in general) loaded bi-axially, with a variable amplitude and a variable R-ratio. Thus the model should be extended to include these factors.

Third, the influence of other factors than loading that may influence the delamination growth rate should be investigated. Based on this research this will certainly include the effect of temperature, but other factors may include humidity, manufacturing quality and bond-line thickness.

Finally the model should be validated for structures that more closely resemble structural components as used in practice, so including single or double curvature and supporting structures such as stringers, ribs, and frames.

All in all the model developed in this research appears to be promising, but is merely a first step on the road to a full damage tolerance model for bonded repairs.

References

[1] A. A. Baker. Repair of cracked or defective metallic aircraft components with advanced fibre composites–an overview of Australian work. *Composite Structures*, 2(2):153–181, 1984.

[2] H. J. M. Woerden, J. Sinke, and P. A. Hooijmeijer. Maintenance of Glare structures and Glare as riveted or bonded repair material. *Applied Composite Materials*, 10(4):307–329, 2003.

[3] A. Rider and R. Vodicka. Proposed framework for a risk-based approach for the environmental certification of adhesively bonded repairs. Technical Report DSTO-RR-0282, DSTO, 2004.

[4] Y.J. Guo and X.R. Wu. Bridging stress distribution in center-cracked fiber reinforced metal laminates: modeling and experiment. *Engineering Fracture Mechanics*, 63(2):147–163, 1999.

[5] E. S. Aggelopoulos, T. D. Righiniotis, and M. K. Chryssanthopoulos. Debonding of adhesively bonded composite patch repairs of cracked steel members. *Composites Part B: Engineering*, 42(5):1262–1270, 2011.

[6] R. C. Alderliesten. *Fatigue crack propagation and delamination growth in Glare*. PhD thesis, Delft University of Technology, 2005.

[7] R. C. Alderliesten. Damage tolerance of bonded aircraft structures. *International Journal of Fatigue*, 31(6):1024–1030, 2009.

[8] J. Schijve. *Fatigue of Structures and Materials*. Springer, Delft, 2nd edition, 2009.

[9] R. C. Alderliesten. Analytical prediction model for fatigue crack propagation and delamination growth in Glare. *International Journal of Fatigue*, 29(4):628–646, 2007.

[10] R. Marissen. *Fatigue crack growth in ARALL. A hybrid aluminium-aramid composite material: Crack growth mechanisms and quantitative predictions of the crack growth rates*. PhD thesis, Delft University of Technology, 1988.

[11] R. Jones, S. Barter, L. Molent, and S. Pitt. Crack patching: An experimental evaluation of fatigue crack growth. *Composite Structures*, 67(2 SPEC. ISS.):229–238, 2005.

[12] R. Jones. A scientific evaluation of the approximate 2D theories for composite repairs to cracked metallic components. *Composite Structures*, 87(2):151–160, 2009.

[13] R. L. Hastie, R. Fredell, and J. W. Dally. A photoelastic study of crack repair. *Experimental Mechanics*, 38(1):29–36, 1998.

[14] M. Boscolo, G. Allegri, and X. Zhang. Enhanced 2-D modeling technique for single-sided patch repairs. *AIAA Journal*, 47(6):1558–1567, 2009.

[15] C. D. Rans, R. C. Alderliesten, and R. Benedictus. Predicting the influence of temperature on fatigue crack propagation in fibre metal laminates. *Engineering Fracture Mechanics*, 78(10):2193–2201, 2011.

[16] R. C. Alderliesten, J. Schijve, and S. van der Zwaag. Application of the energy release rate approach for delamination growth in Glare. *Engineering Fracture Mechanics*, 73(6):697–709, 2006.

[17] C. Rans, R. C. Alderliesten, and R. Benedictus. Misinterpreting the results: How similitude can improve our understanding of fatigue delamination growth. *Composites Science and Technology*, 71:230–238, 2011.

[18] G. Allegri, M. I. Jones, M. R. Wisnom, and S. R. Hallett. A new semi-empirical model for stress ratio effect on mode II fatigue delamination growth. *Composites Part A: Applied Science and Manufacturing*, 42(7):733–740, 2011.

[19] A. S. J. Suiker and N. A. Fleck. Crack tunneling and plane-strain delamination in layered solids. *International Journal of Fracture*, 125(1-2):1–32, 2004.

[20] R. C. Alderliesten. On crack tunneling and plane-strain delamination in laminates. *International Journal of Fracture*, 148(4):401–414, 2007.

[21] G. Ji, Z. Ouyang, and G. Li. Effects of bondline thickness on Mode-II interfacial laws of bonded laminated composite plate. *International Journal of Fracture*, 168(2):197–207, 2011.

[22] E.F. Rybicki and M.F. Kanninen. A finite element calculation of stress intensity factors by a modified crack closure integral. *Engineering Fracture Mechanics*, 9(4):931–938, 1977.

[23] R. Krueger. The virtual crack closure technique: History, approach and applications. Technical Report NASA/CR-2002-211628, NASA, 2002.

[24] D. Xie and S. B. Biggers Jr. Strain energy release rate calculation for a moving delamination front of arbitrary shape based on the virtual crack closure technique. Part I: Formulation and validation. *Engineering Fracture Mechanics*, 73(6):771–785, 2006.

[25] D. Xie and S. B. Biggers Jr. Strain energy release rate calculation for a moving delamination front of arbitrary shape based on the virtual crack closure technique. Part II: Sensitivity study on modeling details. *Engineering Fracture Mechanics*, 73(6):786–801, 2006.

[26] M. Boscolo and X. Zhang. A modelling technique for calculating stress intensity factors for structures reinforced by bonded straps. Part I: Mechanisms and formulation. *Engineering Fracture Mechanics*, 77(6):883–895, 2010.

[27] M. Boscolo and X. Zhang. A modelling technique for calculating stress intensity factors for structures reinforced by bonded straps. Part II: Validation. *Engineering Fracture Mechanics*, 77(6):896–907, 2010.

[28] R. Krueger. Development of a benchmark example for delamination fatigue growth prediction. Technical Report NASA/CR-2010-216723 / NIA Report No. 2010-04, NASA / NIA, 2010.

[29] R. Krueger. Development of benchmark examples for delamination onset and fatigue growth prediction. Technical Report NF1676L-11493, NASA, 2011.

[30] R. Krueger. Development of benchmark examples for static delamination propagation and fatigue growth predictions. Technical Report NF1676L-11356, NASA, 2011.

[31] K. L. Roe and T. Siegmund. An irreversible cohesive zone model for interface fatigue crack growth simulation. *Engineering Fracture Mechanics*, 70(2):209–232, 2003.

[32] H. Khoramishad, A. D. Crocombe, K. B. Katnam, and I. A. Ashcroft. Predicting fatigue damage in adhesively bonded joints using a cohesive zone model. *International Journal of Fatigue*, 32(7):1146–1158, 2010.

[33] Anonymous. Matweb. www.matweb.com, Last accessed: 07-03-2012.

[34] G. Roebroeks. The metal volume fraction approach (restricted). Technical Report TD-R-00-003, Delft University of Technology, 2000.

[35] R.C. Alderliesten. Delamination growth at bonded interfaces - calculation approach (restricted). Technical Report B2v-06-12, Delft University of Technology, 2006.

[36] Anonymous. *Abaqus 6.10-1 PDF Documentation*. Dassault Systèmes, 2010.

[37] S. Kumar and P. C. Pandey. Fatigue life prediction of adhesively bonded single lap joints. *International Journal of Adhesion and Adhesives*, 31(1):43–47, 2011.

[38] Anonymous. FM73 epoxy film adhesive technical data sheet. Technical report, Cytec, 2011.

[39] R. Marissen. Ae4633 Composite Materials for Durable Structures; Lecture Notes, 2009.

[40] H. Thomas Han, Milan Mitrovic, and Ozgur Turkgenc. The effect of loading parameters on fatigue of compostie laminates: Part III. Technical Report DOT/FAA/AR-99/22, US Department of Transportation, Federal Aviation Administration, Office of Aviation Research, 1999.

Appendix A

Complete Test Results

This appendix contains graphs of all the test results for series A and B per specimen.

A.1 Series A

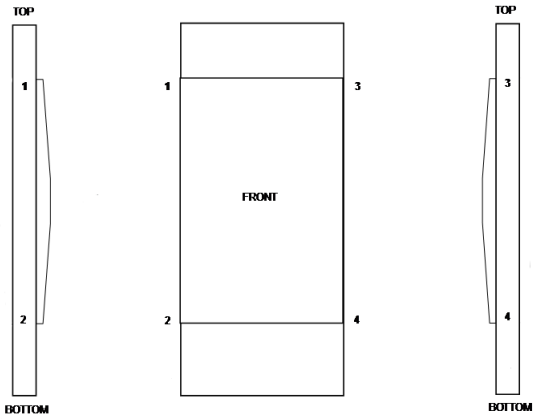

Figure A.1: Nomenclature used for series A specimens. Adapted from a figure by C. Rans (unpublished).

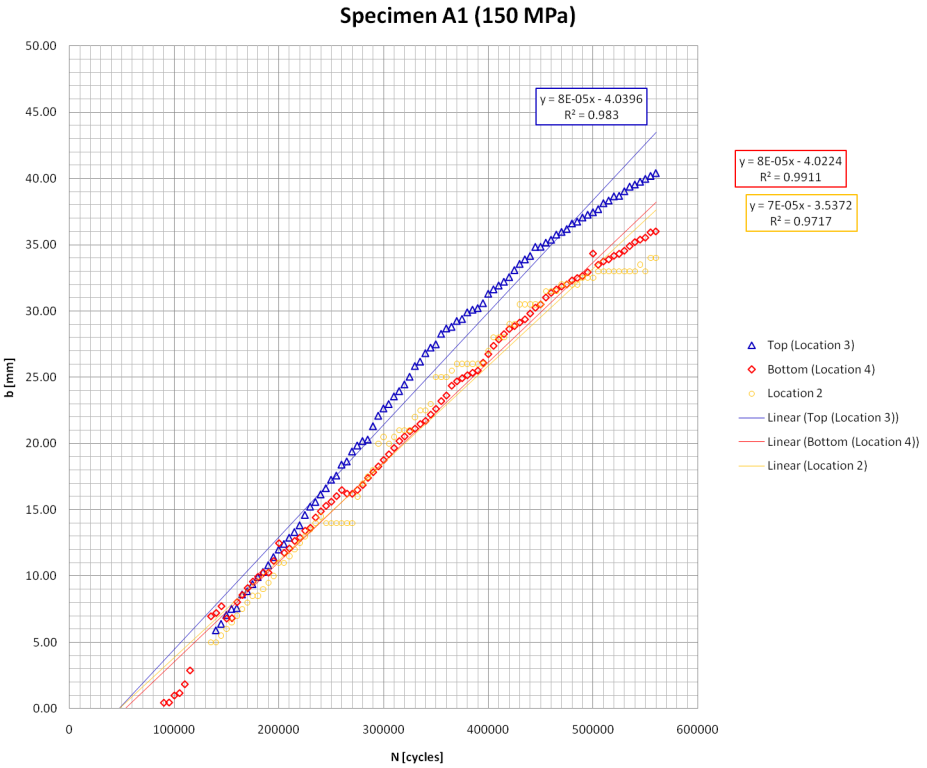

Figure A.2: Delamination lengths measured for specimen A1. Measurements done at location 2 were performed using the naked eye and a ruler and so are less accurate.

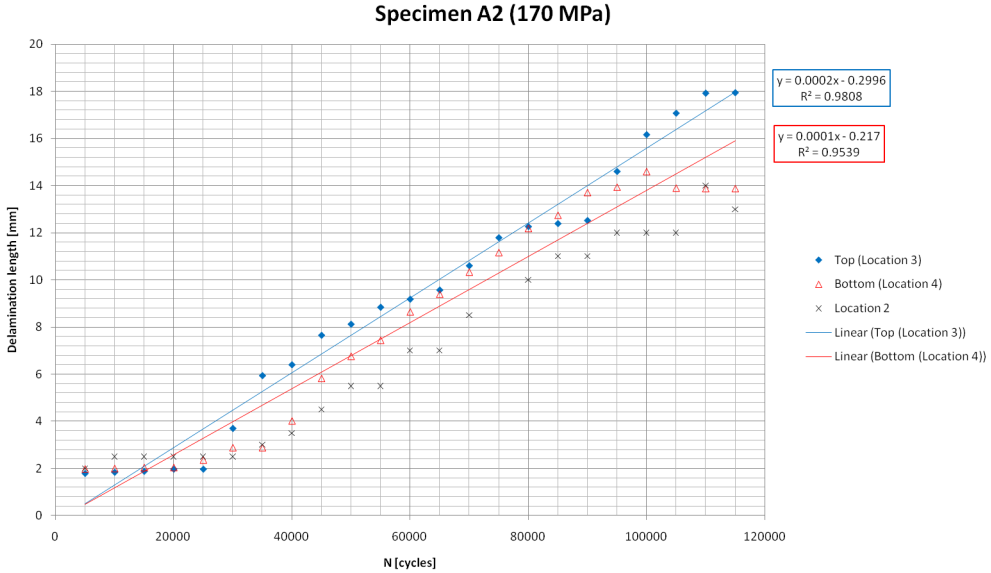

Figure A.3: Delamination lengths measured for specimen A2. Measurements done at location 2 were performed using the naked eye and a ruler and so are less accurate.

A.2 Series B

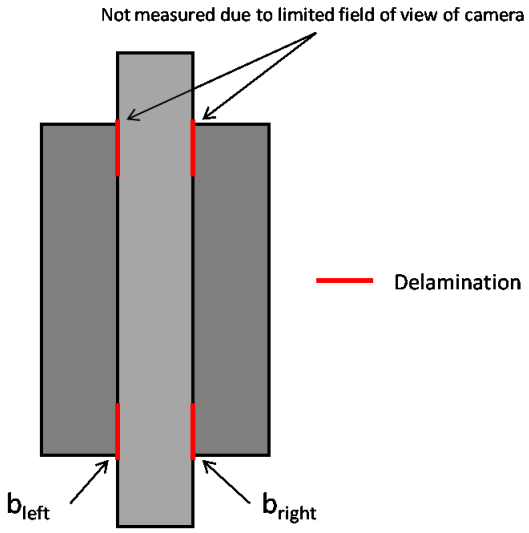

Figure A.4: Nomenclature used for series B specimens.

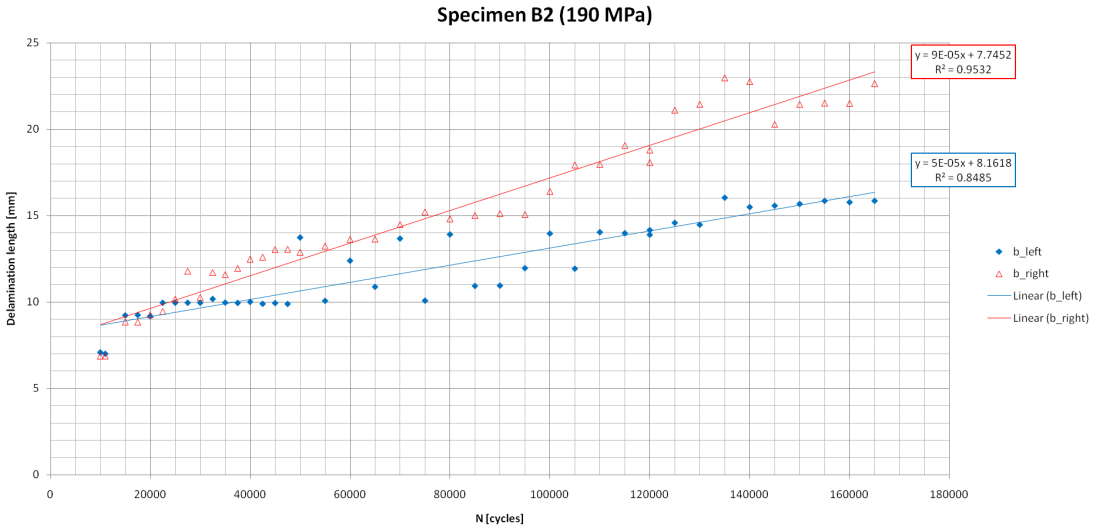

Figure A.5: Delamination lengths measured for specimen B2.

Figure A.6: Delamination lengths measured for specimen B3.

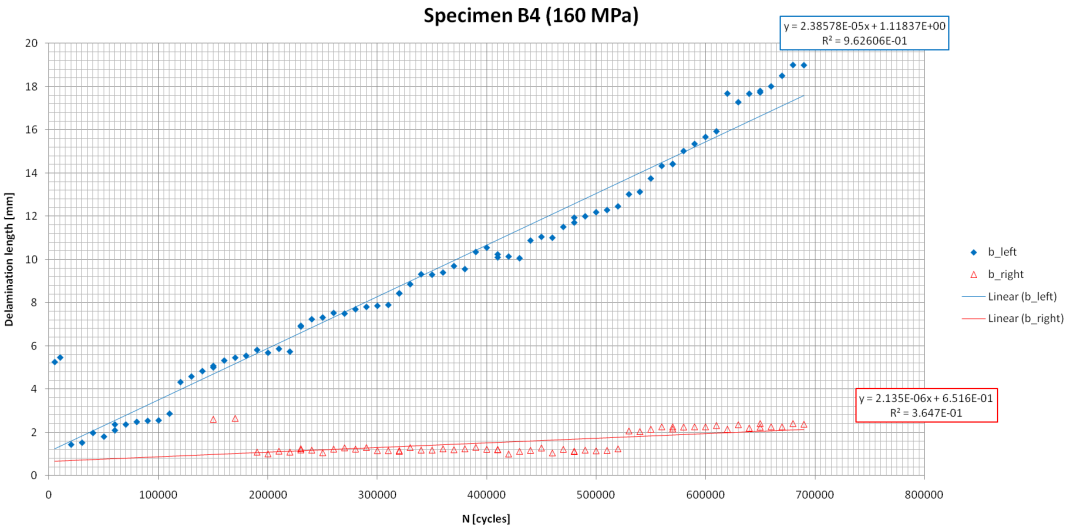

Figure A.7: Delamination lengths measured for specimen B4.

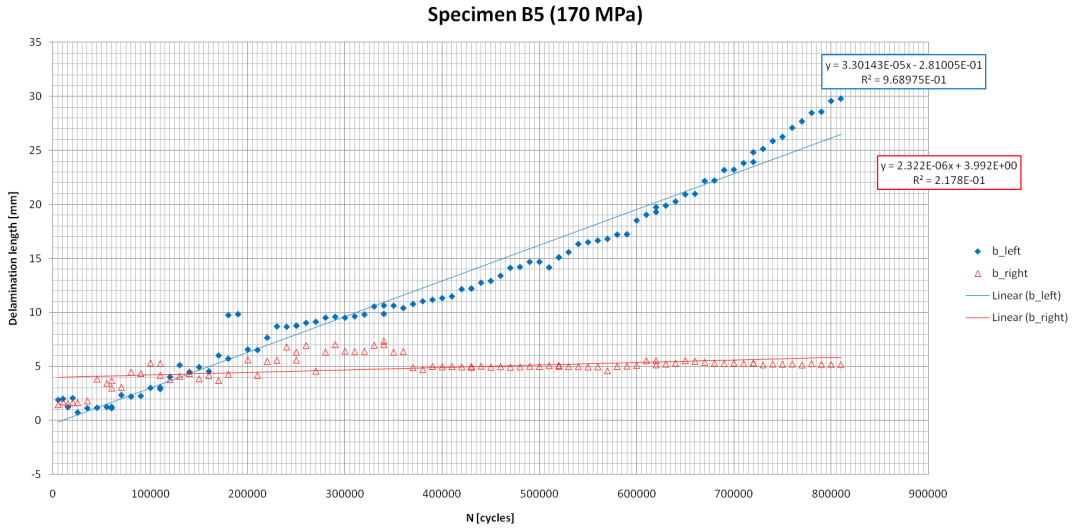

Figure A.8: Delamination lengths measured for specimen B5.

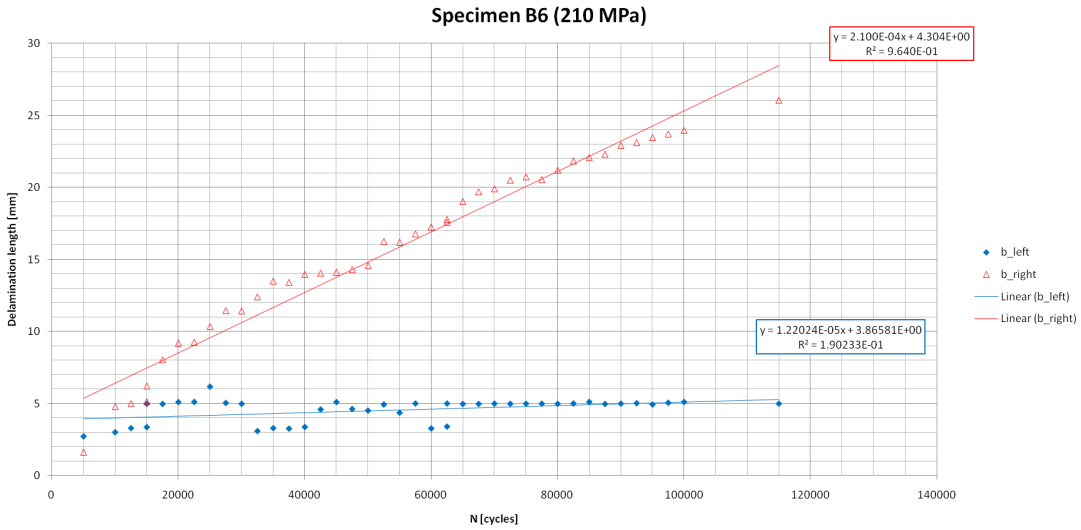

Figure A.9: Delamination lengths measured for specimen B6.

Appendix B

Matlab Code

This appendix contains the full code of the Matlab program used to numerically predict the delamination growth.

```
%% Matlab reset

clear all
close all
clc

%% Request User Input

prompt = {'Enter specimen number: A1, A2, B2-B6, C1, C2', '-30C [C] or
 Room Temperature [R]', 'Enter \Delta N','Enter N_{max}', 'G_{tot} [1]
 or G_{II} [2]'};
dlg_title = 'Input for delamination prediction';
num_lines = 1;
def = {'A1','R','100','5e5','1'};
options.Resize='on';
options.WindowStyle = 'normal';
options.Interpreter = 'tex';
inputvals = inputdlg(prompt,dlg_title,num_lines,def,options);
specimen = inputvals{1};
Temperature = inputvals{2};
G_function = str2double(inputvals{5});


%% Read in test data, primary crack

temp = dlmread(strcat(specimen,'-1.csv'),';',1,0);
Ntest1 = temp(:,1);
```

```
btest1 = temp(:,2);

%% Initialisation of variables

b_0 = temp(1,9);                    %Initial delamination size in mm
delta_N = str2double(inputvals{3}); %Step size
N_max = str2double(inputvals{4});   %Maximum number of cycles

if Temperature == 'T'
    if G_function == 1
        c = 2.6906E-04;    %Paris "constants", RT, for
 trial purposes
        m = 2.6059;
    end
    if G_function == 2
        c = 3.8922E-03;
        m = 3.4178;
    end
end

if Temperature == 'C'
    if G_function == 1
        c = 5.2931e-4;     %Paris "constants", -30C
        m = 3.5747;
    end
    if G_function == 2
        c = 4.7913e-3;
        m = 3.5895;
    end
end

if Temperature == 'R'
    if G_function == 1
        c = 2.3579E-03;     %Paris "constants", RT
        m = 2.5760;
    end
    if G_function == 2
        c = 3.0244E-02;
        m = 3.3325;
    end
end

a1 = temp(G_function,3);     %Polynominal coefficients of G vs b.
a2 = temp(G_function,4);
a3 = temp(G_function,5);
a4 = temp(G_function,6);
a5 = temp(G_function,7);
```

```
b_plot = b_0;
G_plot = 0;
N_plot = 0:delta_N:N_max; %Vectors to allow plotting of delamination growth

offset = temp(1,8)
 %Offset in test data plotting to match initial delamination size.

%% Read in test data, secondary crack

temp = dlmread(strcat(specimen,'-2.csv'),';',1,0);
Ntest2 = temp(:,1);
btest2 = temp(:,2);

%% Numerical intergration of db/dN

b=b_0;
for i=1:delta_N:N_max
    G = a1*b^4+a2*b^3+a3*b^2+a4*b+a5; %G = f(b), polynominal fit from excel
    dbdN = c*G^m;      %db/dN = f(G_max), Paris relation fit from from excel
    delta_b = dbdN*delta_N;
    b = b+delta_b;
    b_plot = [b_plot b];
    G_plot = [G_plot G];
end

%% Plot results

hold on
plot(N_plot,b_plot)
plot(Ntest1-offset,btest1,'.r')
plot(Ntest2-offset,btest2,'*r')
grid on
xlabel('N [cycles]')
ylabel('b [mm]')
legend ('Model Prediction', 'Measured Delamination 1', 'Measured
Delamination 2','Location', 'NorthWest')
hold off
figure
plot(b_plot,G_plot) %Plot of G vs b, for bughunting purposes
```